The Local Group in LCDM - Shapes and masses of dark halos

Vera-Ciro, Carlos Andrés

rijksuniversiteit groningen

The Local Group in ΛCDM
Shapes and masses of dark halos

Proefschrift

ter verkrijging van het doctoraat in de
Wiskunde en Natuurwetenschappen
aan de Rijkuiversiteit Groningen
op gezag van de
Rector Magnificus, dr. E. Sterken,
in het openbaar te verdedigen op
maandag 21 januari 2013
om 11:00 uur

door

Carlos Andrés Vera Ciro

geboren op 8 december 1983
te Ituango, Colombia

Promotor:	Prof. dr. A. Helmi
Copromotor:	Dr. L.V. Sales
Beoordelingscommissie:	Prof. dr. J.M. van der Hulst Prof. dr. J.F. Navarro Prof. dr. S.D. M. White

ISBN: 978-90-367-5987-8
ISBN: 978-90-367-5988-5 (electronic version)

Cover: Dark matter distribution of the Aq-A-2 halo and one of its tidal streams

Printed by: Ipskamp Drukkers, Enschede

Contents

CHAPTER 1
Introduction

What is the problem with ΛCDM? Well, first is "Λ", and then "C" and then there is the "DM" part ...

Nick Gnedin

1.1 The ΛCDM Universe

Through history, some of the most fundamental questions about our place in the Universe have stemmed from looking at the heavens. On clear nights the naked eye is able to perceive myriads of stars and some other extended and fuzzy objects, such as the clouds discovered by Magellan et al. (1519) much before BibTeXwas invented.

Many more of such objects were discovered with the advent of improved observational techniques, and led to the construction of large catalogs containing tens of thousands of *nebulae* (Dreyer, 1888). The nature of these nebula was a matter of debate especially at the beginning the last century: whether they were nearby objects or distinct entities outside of the Milky Way was the topic of discussion of more than one coffee break (Smith, 1982). It was Edwin Hubble who finally solved the puzzle by measuring the distance to some of the nebulae. One such example was the Andromeda Galaxy, now known to be located at approximately 2.4×10^{19} km from the Earth, or 778 ± 17 kpc[1], which is 25 times the size of the Milky Way (Karachentsev et al., 2004). This conclusively showed that some of the observed nebulae are indeed extragalactic objects.

By using a version of the Doppler effect applied to light known as *redshift* of spectral lines, Hubble (1929) showed in addition that these galaxies are not only moving, but they appear to be receding from us with a velocity that is proportional to their distance. Rather than implying that we are at the center of the Universe, this can be explained if the Universe is in expansion.

The list of surprises does not end there though. From measurements of the velocities of individual galaxies in the Coma cluster, Zwicky (1937) was able to make an estimate of its total mass. Unexpectedly he found it was ~ 400 times larger than the value derived by adding up the galaxies visible mass. This discovery constitutes one of the most fundamental problems in astrophysics for almost one century now. We refer to this invisible mass as *Dark Matter* and it appears to be dominant component of extragalactic structures.

The need for dark matter also is evident on the scale of individual galaxies, for example from the rotation curves of spirals. Assume for instance that a galaxy has a distribution of mass $M(r)$, then the circular velocity profile will follow the law $v_{\rm circ}^2 = GM(r)/r$. Naively this would imply that beyond the edge of the galaxy, its circular velocity profile should decrease as $v_{\rm circ} \sim r^{-1/2}$. Observations however show that the rotation curve of spiral galaxies is flat at large radii, indicating the presence of additional mass beyond that contributed by gas and stars (Bosma, 1981a,b; Sofue & Rubin, 2001).

These experiments do not reveal what dark matter consists of. Stellar remnants, dim enough to remain undetected from earth, were once considered

[1] A more natural unit used to represent distances in astronomy, namely the parsec, where 1 pc $= 3.09 \times 10^{16}$ m.

a possibility (White & Rees, 1978; Carr & Rees, 1984). Arguments based on the amount of baryons expected from nucleo-synthesis at the dawn of time, confidently rule this out, although some small fraction of dark matter could be made of left-overs from stellar evolution. Neutrinos, a light neutral particle of the Standard Model of particle physics, have also been suggested as candidates. These particles are so common that right now $\sim 10^9$ of them are crossing this little black square ■ every second (Bahcall, Serenelli & Basu, 2005). This estimate comes just from the reactions that occur inside our Sun. Neutrinos, however, have been discarded as the only form of dark matter because they produced stronger clustering on large scales than observed in the cosmic web (White, Davis & Frenk, 1984).

These two arguments combined narrow the list of possible candidates for dark matter in the Standard Model. Currently, the most favored candidates are weakly interacting particles, and these particles are termed "warm" or "cold" depending on the velocity at the time of decoupling. Some additional constraints can be obtained from the Lyman α forest (e.g. Viel et al., 2008), and the abundance of substructures in the Galactic halo (Lovell et al., 2011a; Benson et al., 2012) (See also Chapter 4 of this Thesis), although the conclusions are somewhat controversial (Macciò et al., 2012). The direct detection of dark matter particles will undoubtedly reveal their nature. However these experiments are extremely challenging. Indirect detection through annihilation of dark matter particles would also be a possibility, although no conclusive signals have yet been measured (For a complete review on Galactic searches of Dark Matter please refer to Strigari, 2012).

An even more bizarre discovery was made in an extension of Hubble's experiment carried out including objects probing larger distances (Riess et al., 1998; Perlmutter et al., 1999). It showed that the universe is not only expanding, but actually that it is accelerating. Even if the Universe, as a whole, is dominated by dark matter, this result is counter-intuitive, in the sense that classical mechanics suggests that the mutual interaction of galaxies through gravity will lead to a reduction in the acceleration rate, instead of the observed increment. To account for this phenomenon, an additional force field is necessary. This has been termed as *Dark Energy*, and can be parametrized as a fluid whose pressure and density follows the equation of state $P_\Lambda \sim -\rho_\Lambda$. About its nature we know close to nothing.

As a result we now have a picture of a dynamical universe, dominated on large scales by at least two components: dark matter and dark energy. To model this Universe as an entity we use Einstein's field equations (Friedmann, 1924). Solutions to this model are mathematically encapsulated in the properties of the clocks used to measure time and the rules to measure distances, or more formally, the *metric*. For a universe that is homogeneous and isotropic, the infinitesimal distance between two events that occur at the coordinates

(t, r, Ω) and $(t + dt, r + dr, \Omega + d\Omega)$ can be written as,

$$ds^2 = -c^2 dt^2 + a(t)^2 \left[dr^2 + S_\kappa(r)^2 d\Omega^2 \right], \tag{1.1}$$

with c the speed of light, and $S_\kappa(r)$ a function that describes the (only) three different types of curvature κ that are consistent with the assumption homogeneity and isotropy. The scale factor $a(t)$ and the type of curvature κ are univocally determined by the matter/energy content of the Universe. It is possible to show that for a universe composed of pressureless matter (dark matter), radiation and a fluid with negative pressure (dark energy), with densities ρ_m, ρ_r and ρ_Λ, respectively, the scale factor a follows the equation (Peebles, 1980)

$$\frac{\dot{a}}{a} = H_0 E(a) \equiv H(a) \tag{1.2}$$

where,

$$E^2(z) = \Omega_{\Lambda,0} + (1 - \Omega_0)(1 + z)^2 + \Omega_{m,0}(1 + z)^3 + \Omega_{r,0}(1 + z)^4, \tag{1.3}$$

with $\Omega_0 = \rho(t_0)/\rho_{\rm crit}(t_0)$ the density of the different components in units of the critical value $\rho_{\rm crit,0} = 3H_0^2/8\pi G$, and $a = 1/(1 + z)$. The script "0" is used to indicate quantities measured at present day, i.e. $z = 0$. Note that from this expresion, all the information required to model the dynamics of the Universe is contained in the quantities $\Omega_0 = \sum_i \Omega_{i,0}$ and H_0.

Current estimates of the values of these parameters are $H_0 = 100h = 70.4^{+1.3}_{-1.4}$ km/s/Mpc, $\Omega_{m,0} = 0.227 \pm 0.014$, $\Omega_{\Lambda,0} = 0.728^{+0.015}_{-0.016}$, $\Omega_{r,0} = 8.1 \times 10^{-5}$ (Komatsu et al., 2011). In light of these results, the energy budget of the Universe is currently dominated by dark energy, followed by dark matter. It is geometrically flat ($\kappa \sim 1 - \Omega_0 = 0$) and in accelerated expansion.

This Universe, together with a specific spectrum for primordial density perturbations and where the dark matter is cold, is described by the ΛCDM model, and constitutes the framework of this Thesis.

1.2 Formation of structures in ΛCDM

One consequence of having an universe in expansion is that at some point in the past it must have been denser and hotter than it is today. Some time after the Big Bang it cooled down enough and structure formation started to take place. From that point onwards, we can model the density perturbations in the dark matter $\delta(\boldsymbol{x}, t) = 1 - \rho(\boldsymbol{x}, t)/\overline{\rho}_m(t)$ as a classical pressureless dust in a universe in expansion using the continuity, Euler and Poisson Equations. It can be shown that these equations reduce to

$$\frac{d^2\delta}{dt^2} + 2\frac{\dot{a}}{a}\frac{d\delta}{dt} = 4\pi G \overline{\rho}_m \delta \quad \text{for } \delta \ll 1, \tag{1.4}$$

where $\overline{\rho}_m$ is the mean matter density at time t. This equation has two solutions, but only one of them grows with time. An approximate solution is $\delta_+ \propto g(z)/(1+z) \propto D(z)$ where (Carroll, Press & Turner, 1992)

$$g(z) \approx \frac{5}{2}\Omega_m(z)\left\{\Omega_m^{4/7}(z) - \Omega_\Lambda(z) + [1+\Omega_\Lambda(z)/2]\,[1+\Omega_\Lambda(z)/70]\right\}^{-1}. \quad (1.5)$$

This expression models the evolution of primordial perturbations until they enter the non-linear regime, that is, until δ becomes of order of unity. To follow the evolution of these perturbations in the non-linear regime $\delta \gg 1$, a different approach is necessary. Consider a spherically symmetric mass shell enclosing a mass M. This shell evolves according to Newton's 2nd law, which before the shell collapses onto the distribution M, can be written as,

$$\frac{1}{2}\left(\frac{dr}{dt}\right)^2 - \frac{GM}{r} = E, \quad (1.6)$$

with E the specific energy of the shell. For $E < 0$, it can be shown that the solution to this expression can be given in the parametric form

$$r = A(1-\cos\theta), \qquad t = B(\theta - \sin\theta), \quad (1.7)$$

where the factors A and B can be written in terms of the initial conditions (Gunn & Gott, 1972; Fillmore & Goldreich, 1984),

$$A = \frac{1}{2}\frac{r_i}{[5\delta_i/3 - \Omega_i^{-1}]}, \qquad B = \frac{3}{4}\frac{t_i}{[5\delta_i/3 - \Omega_i^{-1}]^{3/2}}. \quad (1.8)$$

Each shell will therefore expand until it reaches the maximum radius $r_{\max} = 2A$ at $t = \pi B$ and then collapse. The overdensity at the time of collapse $t_{\rm col} \equiv 2t_{\max}$ for a matter dominated universe is,

$$\delta(t_{\rm col}) = \frac{3}{5}\left(\frac{3\pi}{2}\right)^{2/3}[\Omega(t_{\rm col})]^{0.0185} \approx 1.686[\Omega(t_{\rm col})]^{0.0185}. \quad (1.9)$$

In this model, isolated perturbations with overdensity larger than $\delta_c = 1.686$ will collapse under their own gravity and form a virialized object.

The evolution of an ensemble of perturbations that follow this prescription can be modeled in a statistical fashion. Consider the perturbation density field $\delta(\boldsymbol{x})$ following the dynamics described above. This field can be smoothed on some scale R, by convolving it with a window function with the same scale length W_R. The smoothed field $\delta_s(\boldsymbol{x}) \equiv (\delta \star W_R)(\boldsymbol{x})$ will follow a Gaussian distribution if $\delta(\boldsymbol{x})$ is Gaussian,

$$P(\delta_s)d\delta_s = \frac{1}{\sqrt{2\pi}\sigma(R)}\exp\left[-\frac{\delta_s^2}{2\sigma^2(R)}\right]d\delta_s, \quad (1.10)$$

where $\sigma(R)$ is the variance of the perturbations on the length scale R, or equivalently, with the mass scale $M \sim \overline{\rho} R^3$.

At a particular position $\boldsymbol{x}$ consider now a set of overdensities generated by smoothing the density field on different mass scales $S = \sigma^2(M)$, if the density perturbation field δ is Gaussian, it can be shown that Eq. (1.10) generates a Markovian random walk $\delta_s = \delta_s(S)$, where the fraction of all trajectories that have $\delta_s(M') > \delta_c$ equals the fraction of collapsed objects with mass $M > M'$ (Press & Schechter, 1974; Bond et al., 1991). Each of these walks has its origin at $\delta_s(S = 0) = 0$, which just reflects the homogeneity of the underlying density field on very large scales $\sigma(M \to \infty) = 0$. In general if $M_1 > M_2$ then $S(M_1) < S(M_2)$.

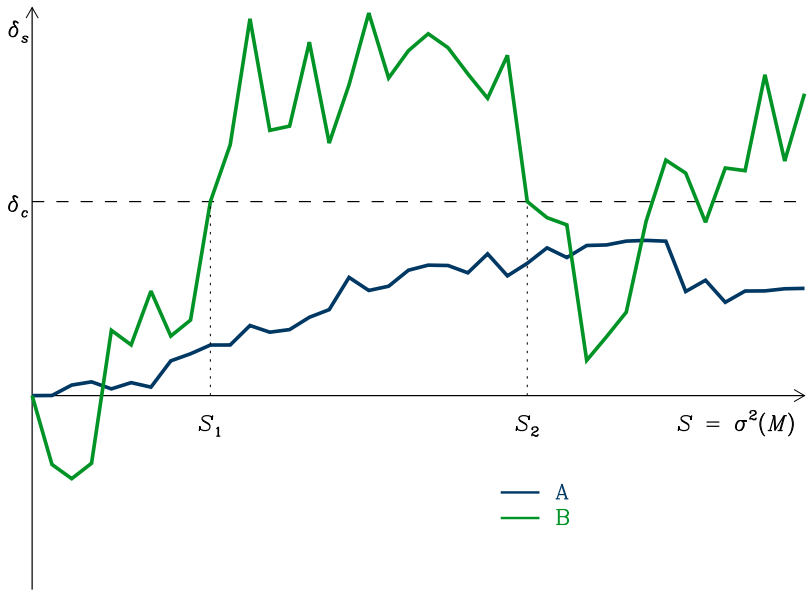

Figure 1.1: Examples of Markovian random walks of the perturbation density field δ_s smoothed on different scales $R \sim M^{1/3}$. The fraction of all trajectories that have $\delta_s(M') > \delta_c$ equals the fraction of collapsed objects with mass $M > M'$.

In Fig. 1.1 we show two examples of such trajectories. According to this prescription, the random walk `A` does not cross the critical overdensity δ_c for $S < S_1$, that means that this particular overdensity will never be part of a collapsed object with $M > M_1$. The trajectory `B` on the other hand has $\delta_s > \delta_c$ at S_1, therefore it will be part of a collapsed halo with $M > M_1$.

By increasing the mass scale M, the region around the perturbation that is smoothed is also increased $R \sim M^{1/3}$, including, possibly, other density peaks. Trajectory `B` for instance describes a perturbation that will be part of a collapsed object with mass $M > M_2$ and also of an object with mass $M > M_1$, with $M_1 > M_2$. By increasing the mass scale from M_2 to M_1, the smoothed

density field around this perturbation, randomly grows and decreases, indicating that several other density perturbations are being included in the process. An overdensity such as the one described by `B` therefore reflects one of the fundamental features in the ΛCDM cosmogony: a collapsed halo is *not* formed by one single density peak, but contains several other peaks, that may or not have virialized themselves.

Overdensities therefore grow by accretion of smaller objects. This hierarchical way of mass assembly encapsulates some of the most fundamental aspects of structure formation in ΛCDM. The predicted number density of collapsed objects with masses between M and $M + dM$ is therefore

$$\begin{aligned} m(M,t)dM &= 2 \times \frac{\overline{\rho}}{M}\frac{\partial \mathcal{P}}{\partial M}dM = \sqrt{\frac{2}{\pi}}\frac{\overline{\rho}}{M^2}\frac{\delta_c}{\sigma}\exp\left(-\frac{\delta_c^2}{2\sigma^2}\right)\left|\frac{d\ln\sigma}{d\ln M}\right|dM \\ &= \frac{\overline{\rho}}{M^2}f_{\rm PS}(M,\sigma)\left|\frac{d\ln\sigma}{d\ln M}\right|dM, \end{aligned} \tag{1.11}$$

where $\mathcal{P} = \int_{\delta_c}^{\infty} P(\delta_s)$. Several other predictions can be extracted from this formalism, for instance the mass spectrum of objects that merge to form objects of given masses, or the time of assembly of a given dark matter structure (Sheth & Tormen, 1999; Jenkins et al., 2001; Kauffmann & White, 1993). This formalism thus constitutes a powerful tool to explore the statistical properties of objects assembled in ΛCDM.

Note that these results are based on the spherical collapse model introduced at the beginning of this section. In a more realistic scenario the accretion of mass is expected to follow a more anisotropic behavior, because of the presence of randomly placed additional peaks in the perturbation field. Several expressions have been proposed the multiplicity function f that take this into account, such as Sheth & Tormen (1999) who consider triaxial collapse instead of the spherical described above.

However, this complexity is best modeled through computer simulations (Efstathiou et al., 1985). The idea behind this approach is to sample the initial density field at early times and then follow its evolution under the dynamics generated by its own gravity. The so-called N-body simulations use N points as tracers of the density, their positions and velocities are integrated to simulate the formation and evolution of the primordial density fluctuations.

Of course, the larger the number N the better sampled the density field is, but also the more computationally expensive the numerical experiment becomes. The evident progress in both computational techniques and computing power has allowed to dramatically (exponentially) increase this number N in the last decades (Kuhlen, Vogelsberger & Angulo, 2012). For example, one of the most recent simulations of this kind, the *Millennium XXL* simulation, follows the evolution of nearly 303 billion particles (6720^3) in a box of side 4.1 Gpc from $z = 63$ until present day (Angulo et al., 2012).

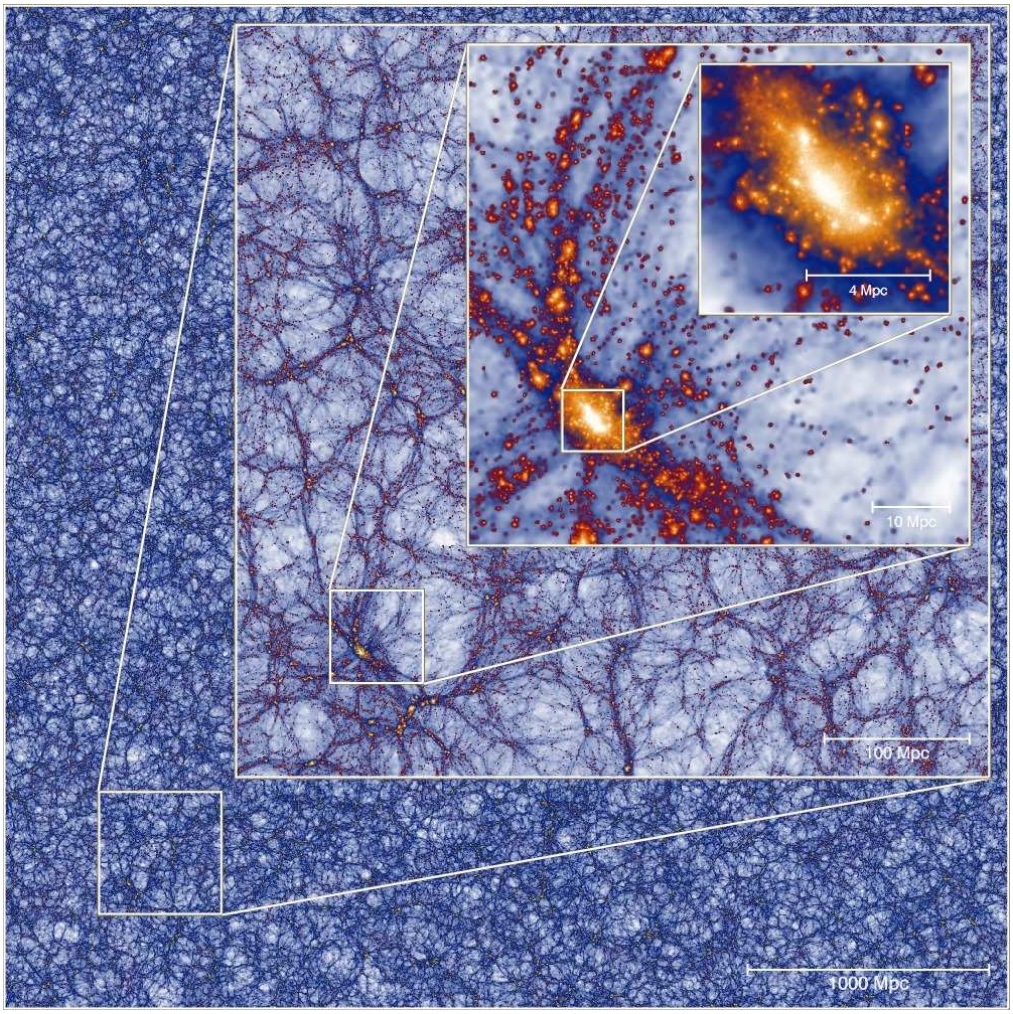

Figure 1.2: Snapshot view of the Millennium XXL simulation at $z = 0$, successive frames zoom into an object of mass $\sim 10^{15}\ M_{\odot}$. Figure from Angulo et al. (2012).

Fig. 1.2 shows a snapshot-view at present day of the density field in this simulation. On the scale of a Gpc, the universe is predominantly homogeneous and no strong features are observed. On scales of ~ 100 Mpc the landscape is dominated by filamentary structures which connect at nodes. The nodes grow through accretion of matter predominantly along these filaments, which gives rise to phenomena such as coherent infall of structures (Libeskind et al., 2011; Lovell et al., 2011b). Smaller scales reveal another important aspect of the hierarchical nature of ΛCDM model, namely, the presence of *substructures*, these are remnants of the accretion of independent halos. Finally, the top-right panel shows that collapsed objects deviate appreciably from perfect spherical symmetry, and although the spherical collapse model described above provides important insights into the process of galaxy formation, objects assembled in

ΛCDM are intrinsically not-spherical.

1.3 Galaxy Formation

So far we have described the properties of the dark matter component in the ΛCDM model. Fortunately, this is the dominant mass component in the Universe, and therefore it dictates the evolution of the baryonic matter to a large extent, and especially so at early times. When the first overdensities have collapsed, the baryons will follow, cool down and eventually form the galaxies that we see today (White & Rees, 1978).

Because the physics governing the evolution of baryons is rather complicated (more than the simple gravity under which dark matter evolves) modeling the formation and evolution of galaxies in a cosmological context has been very challenging. Numerical simulations including gas dynamics, star formation and feedback processes have to be able to resolve a very large dynamical range, from the scale of molecular clouds ($\lesssim 1$ pc) to the cosmological scale ($\sim 10 - 100$ Mpc). This has led to the development of parametrizations of various physical processes, and to impressive numerical simulations (Libeskind et al., 2010; Schaye et al., 2010; Zolotov et al., 2012).

A different, more phenomenological, approach is the so-called semianalytic modeling (SAM) which has the advantage of being computationally less expensive (Kauffmann et al., 1999; Springel et al., 2001; De Lucia, Kauffmann & White, 2004; Croton et al., 2006; De Lucia & Blaizot, 2007). This technique has allowed to study the properties of galaxy populations, their dependence on the environment, evolution with redshift, etc., in a rather successful manner. However, it cannot take into account the dynamical interaction between baryons and dark matter self-consistently, such as e.g. the modification of the inner structure of dark matter halos as a result of feedback from star formation (Governato et al., 2012), or the change in the orbital structure as a response to the presence of baryons (Bryan et al., 2012).

1.4 Properties of halos assembled in ΛCDM halos

Individual halos can be followed with great detail in numerical dark matter simulations. The object shown in the top-right panel of Fig. 1.2, for instance, has a mass of $\sim 10^{15}$ $M_\odot$ and is resolved with $\sim 10^6$ particles. Simulations of smaller boxes allow to resolve objects of similar masses with more particles, at the expense of a less accurate representation of the large-scale tidal field. State of the art simulations can deal with this problem by successively zooming into smaller and smaller scales, and now include several billions of particles

(10^9) to resolve an object of a given scale (Springel et al., 2008; Gao et al., 2012). These suites of N-body simulations have allowed us to make strong and robust predictions about the properties of dark matter halos (in the absence of baryonic effects).

1.4.1 Dark matter substructures

In Section 1.2 we described one of the fundamental aspects of ΛCDM, namely, its hierarchical nature. Structures are assembled through mergers of smaller entities, and therefore, a halo is not expected to be smooth, but to contain substructures (subhalos). Such peaks are also observed in simulations of the ΛCDM cosmogony. The top right panel of Fig. 1.2 shows an example for a cluster-sized dark halo with 668 resolved subhalos (Angulo et al., 2012).

High resolution simulations of MW-like halos resolve tens to hundreds of thousands of these substructures (Diemand, Kuhlen & Madau, 2007; Diemand et al., 2008; Springel et al., 2008; Stadel et al., 2009; Libeskind et al., 2010). The number of subhalos with masses between M and $M + dM$ is usually well fit by the distribution,

$$\frac{dN}{dM}dM = aM^{-n}dM, \tag{1.12}$$

where $n = 1.7 - 1.9$ (Helmi, White & Springel, 2002; Gao et al., 2004; Springel et al., 2008; Gao et al., 2012) and the normalization constant a depends on the mass of the halo. The mass in substructures around a given halo is finite $M_{\rm tot} = \int MdN$ and usually corresponds to less than 10% of the total mass of the host (Ghigna et al., 1998; Stoehr et al., 2003). This mass spectrum could be extrapolated beyond the minimum mass that simulations can resolve, to predict e.g. the number of light objects, for example as light as Jupiter. However two important points need to be taken into account. Firstly, free streaming of dark matter particles does not allow the formation of arbitrarily small structures, this depends on the mass and velocity of the particle, which as previously discussed are not well constrained. Secondly, subhalos may be fully disrupted by the tidal field of the host (Hayashi et al., 2003).

According to Eq. (1.12), for a system like the MW, ΛCDM predicts $\sim 100 - 200$ objects with masses larger than $10^8 \mathrm{M}_\odot$, which clearly contrasts with the ~ 20 that have been observed around the MW (Koposov et al., 2008). This mismatch is known as the *missing satellite problem* (Klypin et al., 1999b; Moore et al., 1999).

1.4.2 Density profile

The radial density profile has been traditionally one of the strongest predictions from ΛCDM. Navarro, Frenk & White (1996) showed that the spherically

averaged density profile of simulated dark matter halos can be described by the parametric form,

$$\rho(r) = \frac{4\rho_{-2}}{(r/r_{-2})(1+r/r_{-2})^2}, \tag{1.13}$$

where r_{-2} is the radius at which the logarithmic slope reaches the isothermal value $d\ln\rho/d\ln r = -2$, and ρ_{-2} is the density at that point. This profile yields a good representation of the density for isolated halos of all masses assembled by dissipationless clustering. The profile is universal and depends on two parameters. One of these can be parametrized as the total integrated mass within a given radius r_h, $M_h = 4\pi \int_0^{r_h} dr' r'^2 \rho(r')$. The other free parameter is conventionally set as the ratio between the characteristic radius r_{-2} and the extent of the halo r_h, $c = r_h/r_{-2}$. In this thesis we will define r_h as the radius at which the mean density of the halo equals 200 times the critical density and conventionally call it the *virial radius*, $r_{\rm vir}$.

The characteristic density $\delta_{\rm char} \equiv 4\rho_{-2}/\rho_{\rm crit}$ is tightly correlated with the formation time of the halo z_f, $\delta_{\rm char} \propto \Omega_{m,0}(1+z_f)^3$ (Navarro, Frenk & White, 1997). The concentration c is also strongly correlated with the total mass of the halo (Neto et al., 2007).

The latest generation of simulations with enough resolution to study the asymptotic behavior of radial density profiles in the central regions of dark matter halos, show that density is better fit by the parametric form (Einasto, 1965)

$$\ln\frac{\rho}{\rho_{-2}} = -\frac{2}{\alpha}\left[\left(\frac{r}{r_{-2}}\right)^{\alpha} - 1\right], \tag{1.14}$$

where $0.1 \lesssim \alpha \lesssim 0.3$ (Gao et al., 2008). Fig. 1.3 shows the density profiles of the six MW-like dark halos from the *Aquarius Simulations* with $\sim 10^8$ particles within $r_{\rm vir}$. The residuals to the best fits to NFW and Einasto models are also shown. The circular velocity profiles actually increase more slowly than the prediction from the NFW model.

1.4.3 Shapes

Despite the prediction power of the spherical collapse model described in the previous section, it was realized early that objects assembled in ΛCDM depart significantly from spherical shapes (Davis et al., 1985; Frenk et al., 1988). Fig. 1.2 shows an example of the geometrical distribution for a cluster-size halo. To a good approximation, the density of dark matter halos can be described with a triaxial ellipsoid with axis lengths $a \geq b \geq c$. The degree of triaxiality in the density contours can be quantified by measuring the difference in lengths at a particular position at the halo. For instance, the minor-to-major

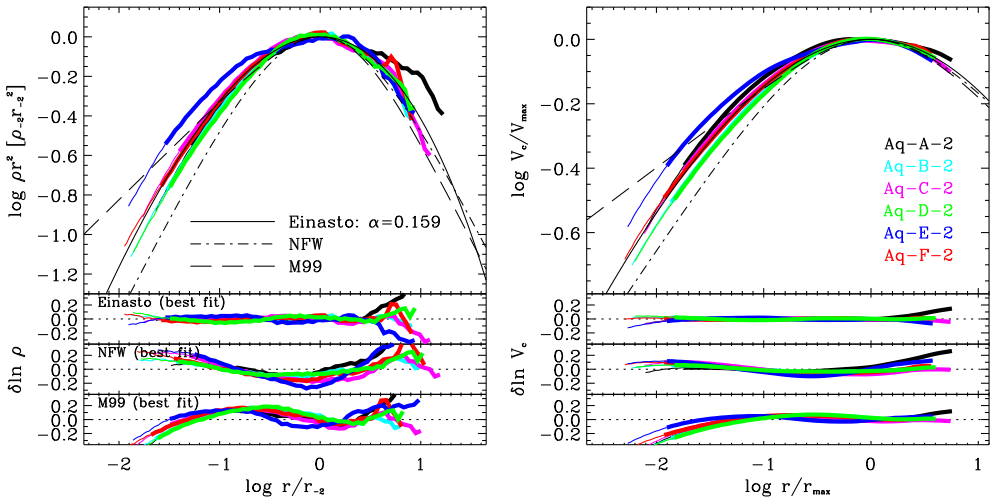

Figure 1.3: Density (left) and circular velocity (right) profiles for the Aquarius halos. Figure from Navarro et al. (2010).

axis ratio c/a quantifies how much a particular density contour deviates from perfect sphericity $c/a = 1$.

Understanding the shapes and orientation of dark matter structures is of particular interest since these depend on the nature of dark matter itself and could be used to constrain its properties (Bullock, 2002). It has also been shown that ignoring the intrinsic non-spherical symmetry of dark halos can lead to biases in the estimations of cosmological parameters (Buote & Humphrey, 2012; Wang & Fan, 2006). Correlations in the orientations of the halos also affect predictions from gravitational lensing, and these are particularly relevant for weak lensing experiments trying to constrain Dark Energy (Faltenbacher et al., 2009).

As a consequence, many studies have been devoted to measuring the shapes, their evolution and their dependence on their surrounding tidal field (Hahn et al., 2007b). The strongest correlation appears with mass, with smaller objects being more spherical in general (Allgood et al., 2006)

$$\langle c/a \rangle = 0.54 \left(\frac{M}{M_\star(z)} \right)^{-0.05} , \tag{1.15}$$

where the mass scale $M_\star$ is defined at redshift z such that $\sigma(M_\star) = \delta_c(z)$. Halos are also in average more elongated at early times (Muñoz-Cuartas et al., 2011). These two results can be interpreted as a consequence of the evolution of the density field in which individual halos are embedded as discussed in more detail in Chapter 2.

1.4.4 The effect of baryons

In general baryonic processes taking place at the center of galaxies can modify to some extent the properties of their host dark matter halos. For example, there may be transfer of angular momentum from a rotating stellar or gaseous disk or bar (Tonini, Lapi & Salucci, 2006). On the other hand, feedback from supernovae (perhaps also from AGN) can modify significantly the central radial density distribution, making it less steep in the inner regions of the galaxy, especially in small systems where the binding energy may be comparable to the energy injection by the exploding stars (Flores & Primack, 1994; Navarro, Eke & Frenk, 1996; Mo & Mao, 2004; Read & Gilmore, 2005; Pontzen & Governato, 2012)

Another example is the formation of a rotating disk from the cooling of baryons in a dark matter halo. Their mass may be sufficiently large that it leads to changes in the dynamics of the dark matter particles in the inner region, which in turn affects the overall distribution of mass. Experiments including gas show that the mass distribution in the region where the disk forms, becomes axisymmetric with minor-to-major axis ratios smaller than unity $c < b \approx a$, (Dubinski, 1994; Debattista et al., 2008; Kazantzidis, Abadi & Navarro, 2010; Abadi et al., 2010; Tissera et al., 2010; DeBuhr, Ma & White, 2012; Bryan et al., 2012). This oblate configuration clearly contrasts the prolate ($c \approx b < a$) inner shapes predicted for MW-like objects in pure dark matter simulations (Vera-Ciro et al., 2011).

1.5 Probing the properties of dark halos with luminous tracers

The rotation curves of spiral galaxies are a very powerful tool to measure the mass profile of their host dark matter halos. Objects with a negligible baryonic contribution to the potential provide the most promising cases, since the response to the dark halo from the presence of baryons can be safely ignored. If the dark matter density profile behaves in the inner parts of the galaxy as $\rho \sim r^{-1}$, as for NFW halos, then the mass profile should rise as $M \sim r^2$ and the circular velocity as $v_{\rm circ} \sim r^{1/2}$. Instead measurements of the kinematics of Low Surface Brightness (LSB) galaxies show a rotation curve with an steeper behavior $v_{\rm circ} \sim r$ implying a density profile that is asymptotically flat in the inner part (cored), $d\ln\rho/d\ln r \sim 0$ (Moore et al., 1999; de Blok et al., 2001; de Blok, 2010). Several explanations have been proposed to alleviate this conflict, even including the effect of baryons. But Hayashi & Navarro (2006) suggested that the inherent triaxiality of dark matter halos (see Fig. 1.2) could affect the conclusions about the presence of cusp/core, since no circular orbits are present in highly asymmetric potentials.

Other experiments have been used to constrain the properties of dark halos. Gravitational lensing constitutes a powerful technique (especially when combined with stellar dynamics, Barnabè et al., 2011, e.g.) for measuring the mass content and geometrical shape of the potential for external galaxies (Hoekstra, Yee & Gladders, 2004; van Uitert et al., 2012) and also for clusters (Newman et al., 2012a,b). However, it is undeniable that to test predictions on the smallest scales the best laboratory is provided by Local Group galaxies.

For these galaxies, the dynamics of individual stars are relatively easy to measure. Consider for instance stars in a spherical system in equilibrium under the effect of the gravitational potential Φ, and f its distribution function, that is, $f(\boldsymbol{x}, \boldsymbol{v}, t)d\boldsymbol{x}d\boldsymbol{v}$ represents the probability of finding a star with position between $\boldsymbol{x}$ and $\boldsymbol{x} + d\boldsymbol{x}$ and velocity between $\boldsymbol{v}$ and $\boldsymbol{v} + d\boldsymbol{v}$. The velocity moments of the distribution are easily calculated as

$$\langle \rho v_r^i v_\theta^j v_\phi^j \rangle = \int d^3\boldsymbol{v} v_r^i v_\theta^j v_\phi^j f(r, \boldsymbol{v}), \tag{1.16}$$

for any i, j and k. From the collissionless Boltzmann equation it is possible to derive an expression relating the stellar density ρ, the radial velocity dispersion of the stars σ_r and the gravitational potential exerted on them Φ (Binney & Tremaine, 2008)

$$\frac{d}{dr}(\rho\sigma_r^2) + 2\frac{\beta}{r}(\rho\sigma_r^2) + \rho\frac{d\Phi}{dr} = 0, \tag{1.17}$$

with $\beta = 1 - \sigma_\theta^2/\sigma_r^2$ the orbital anisotropy. Note that in this case Φ is the total potential of the system, and not only the one generated by the distribution of stars. In other words, if ρ, β and σ_r are known for the stellar component, the functional form of Φ, and therefore that of the dark matter halo, can be calculated using Eq. (1.17). If β is assumed to be constant this equation can integrated to give

$$\rho\sigma_r^2 = r^{-2\beta}\int_r^\infty dr' r'^{2\beta}\rho\frac{d\Phi}{dr'}. \tag{1.18}$$

Unfortunately, most of the information we have about galaxies is only known in projection. Eq. (1.18) can however be related to observables on the sky. The line of sight velocity dispersion as a function of projected radius R from the center of the galaxy is in that case (Binney & Mamon, 1982)

$$\sigma_{\rm los}^2 = \frac{2}{I(R)}\int_R^\infty dr\left(1 - \beta\frac{R^2}{r^2}\right)\frac{\rho\sigma_r^2 r}{\sqrt{r^2 - R^2}}, \tag{1.19}$$

where $I(R)$ is the surface brightness. After parametrizing the potential Φ, best fits to line of sight velocities of stars (or any tracer population, such as globular clusters or satellites) in the galaxy can be used to determine the properties of the underlying mass distribution if the anisotropy is known. Since this is not

usually the case, assumptions have to be made and this limits the power of this approach (Merrifield & Kent, 1990). Measurements of higher moments of the line of sight velocity distribution can, however help break the degeneracy between mass and anisotropy models (Łokas, Mamon & Prada, 2005). Other approaches include full dynamical models through orbit superposition (see e.g. Breddels et al., 2012a; Jardel et al., 2011).

1.5.1 Results for Dwarf Spheroidal galaxies in the MW

Regardless of the method, some interesting results have been obtained over the last few decades concerning the properties of the dark matter distribution in the dwarf galaxies satellites of the MW. Owing their relative small distance, samples with line of sight velocities for thousands of stars are available now. Some of the results of mass modeling indicate for instance that dSph are the most dark matter dominated objects known, with mass-luminosity ratios in the range 100-1000 $M_\odot/L_\odot$ (Walker, 2012).

Some studies suggest that the slopes are shallower than the predicted value from the profile in Eq. (1.13) (Amorisco & Evans, 2011; Walker & Peñarrubia, 2011; Amorisco & Evans, 2012). This however, is a subject of active debate, since various authors have shown that the stellar kinematics of Milky Way dwarfs are also consistent with the NFW cuspy profile (Battaglia et al., 2008; Walker et al., 2009; Strigari, Frenk & White, 2010; Breddels et al., 2012a; Jardel & Gebhardt, 2012).

Most of the works above assume that the dark halos of the dSphs are spherical. However, Hayashi & Chiba (2012) from their modeling of the internal kinematics of 6 of the MW dSph derive an average minor-to-major axis ratio $\langle c/a \rangle_{\rm obs} = 0.6 \pm 0.11$, whereas the prediction from Eq. (1.15) is $\langle c/a \rangle_{\Lambda{\rm CDM}} = 0.9 \pm 0.1$, although the latter is an extrapolation below the resolution limit of the simulations used to derive this result. We take a closer look at this issue in Chapter 3.

1.5.2 Results for the MW

Another system for which the form of the gravitational potential can be estimated is the MW itself. Much recent work has focused on measuring its shape. In this case several approaches have been used such as the properties of the velocity moments (Eq. 1.16) (Sesar, Juric & Ivezic, 2011), or the flaring of the neutral hydrogen layer (Banerjee & Jog, 2011). A popular alternative is the use of the remnants of accretion events known as *stellar streams*.

Streams are coherent structures generated by the disruption of a system in an external tidal field. Consider for instance a galaxy g that is falling into the potential well of a more massive galaxy G. If the gravitational pull generated by G is strong enough, stars from g will be stripped through the *Lagrange*

points of the composite potential (Binney & Tremaine, 2008). The loci of these two stable points closely follows the orbit of g around G, although some deviations are expected (Choi, Weinberg & Katz, 2007; Eyre & Binney, 2009). The stars from g will therefore follow closely the orbit of its center of mass, thereby effectively "revealing" its orbit.

Since properties of the orbit of g are determined by the potential generated by G, by measuring the dynamics of the stars it is, in principle, possible to obtain information about the mass distribution of the host galaxy.

Because of the hierarchical nature of ΛCDM, streams are expected to be ubiquitous. This has been confirmed in deep photometric observations of galaxies in the local volume (Martínez-Delgado et al., 2010; Fardal & PAndAS Collaboration, 2011). The MW itself is surrounded by many streams (Belokurov et al., 2006; Bonaca, Geha & Kallivayalil, 2012). In particular the Sagittarius (Sgr) stream has been used to measure the shape of the MW's dark matter halo (Ibata et al., 2001; Johnston, Law & Majewski, 2005; Helmi, 2004; Koposov, Rix & Hogg, 2010; Law & Majewski, 2010), however the results are rather controversial and difficult to reconcile with the predictions of ΛCDM. In Chapter 5 we investigate this with more detail.

1.6 This thesis

This work focuses on the properties of the dark matter distribution of objects with masses between $10^8 - 10^{12}$ $M_\odot$. We place this study in the context of Local Group galaxies, as our findings (will) help us understand the internal dynamics of these systems.

In Chapter 2 we use the high resolution cosmological N-body simulations from the Aquarius project to investigate in detail the mechanisms that determine the shape of Milky Way-type dark matter halos. We find that, when measured at the instantaneous virial radius, the shape of individual halos changes with time, evolving from a typically prolate configuration at early stages to a more triaxial/oblate geometry at the present day. This evolution in halo shape correlates well with the distribution of the infalling material: prolate configurations arise when halos are fed through narrow filaments, which characterizes the early epochs of halo assembly, whereas triaxial/oblate configurations result as the accretion turns more isotropic at later times. Interestingly, at redshift $z = 0$, clear imprints of the past history of each halo are recorded in their shapes at different radii, which also exhibit a variation from prolate in the inner regions to triaxial/oblate in the outskirts. Provided that the Aquarius halos are fair representatives of Milky Way-like 10^{12} $M_\odot$ objects, we conclude that the shape of such dark matter halos is a complex, time-dependent property, with each radial shell retaining memory of the conditions at the time of collapse.

Chapter 3 extends the analysis of Chapter 2 by exploring the properties

of objects with masses $M \lesssim 10^{11}$ $M_\odot$. Since the Aquarius simulations were designed to replicate the most massive object ($M_{z=0} \approx 10^{12}$ $M_\odot$) at different resolutions, we perform a convergence study using the various Aquarius resolution levels to test the accuracy of our results for this mass range. For the converged objects, we determine the principal axis ($a \geq b \geq c$) of the normalized inertia tensor as a function of radius. In general we find that field halos are more triaxial with increasing halo mass, with our smallest halos being rounder by $\sim 40 - 50\%$ than Milky Way-like objects at the radius of peak circular velocity, $r_{\rm max}$. We find that the distribution of axis ratios for the subhalo population is consistent with that of field halos of comparable $V_{\rm max}$ within the scatter. Inner and outer contours within each object are well aligned, with the major axis preferentially pointing in the radial direction for subhalos close to the host, although with a large scatter. We specifically analyze the dynamical structure of subhalos likely to host luminous satellites comparable to the classical dwarf spheroidals in the Local Group. These halos have axis ratios that increase with radius, and which are mildly triaxial with $\langle b/a \rangle \sim 0.75$ and $\langle c/a \rangle \sim 0.60$ at $r \sim 1$ kpc and ~ 0.9 at large radii. Their anisotropy profiles $\beta(r)$ become strongly tangentially biased in the outskirts as a consequence of tidal stripping.

In connection with observational constraints on the number and characteristics of the satellites of the Milky Way, we present in Chapter 4 a new analysis of the Aquarius simulations done in combination with a semi-analytic galaxy formation model. Our goal is to establish whether the subhalos present in ΛCDM simulations of Milky Way-like systems could host the dwarf spheroidal (dSph) satellites of our Galaxy. Our analysis shows that, contrary to what has been assumed in most previous work, the mass profiles of subhalos are generally not well fit by NFW models but that Einasto profiles are preferred. We find that for shape parameters $\alpha = 0.2 - 0.5$ and $v_{\rm max} = 10 - 30$ km/s there is very good correspondence with the observational constraints obtained for the nine brightest dSph of the Milky Way. However, to explain the internal dynamics of these systems as well as the number of objects of a given circular velocity the total mass of the Milky Way should be $\sim 8 \times 10^{11}$ $M_\odot$, a value that is in agreement with many recent determinations, and at the low mass end of the range explored by the Aquarius simulations. Our simulations show important scatter in the number of bright satellites, even when the Aquarius Milky Way-like hosts are scaled to a common mass, and we find no evidence for a missing population of massive subhalos in the Galaxy. This conclusion is also supported when we examine the dynamics of the satellites of M31.

Finally, in Chapter 5 we present a new model for the dark matter halo of the Milky Way that fits the properties of the stellar streams associated with the Sagittarius dwarf galaxy. In the inner regions, the halo potential is axisymmetric and oblate with $q_z = 0.9$, and therefore is consistent with the expected response to the formation of a baryonic disk in its center. In the

outskirts, the halo follows the shape proposed by Law & Majewski (2010), namely a nearly oblate ellipsoid oriented perpendicular to the Galactic plane. This outer halo can be made more triaxial, with minor-to-major axis ratio $c/a = 0.8$ and intermediate-to-major axis ratio $b/a = 0.9$ if the effect of the Large Magellanic Cloud is taken into account, and thereby made reconcilable with the predictions of ΛCDM simulations, and presented in Chapter 2.

In this thesis we have put forward possible explanations for two well-known conflicting results between ΛCDM and Local Group galaxies, namely, on the properties and number of bright satellites around the Milky Way, and on the shape of the dark halo of the Galaxy. The next years, with the launch of the Gaia mission and various deep photometric and spectroscopic surveys, promise new discoveries and likely will reveal new puzzles. Together with advances in numerical simulations, especially in the degree of sophistication in modeling baryonic processes taking place inside dark matter halos, we expect to learn a great deal about the formation and evolution of galaxies like those found in the Local Group.

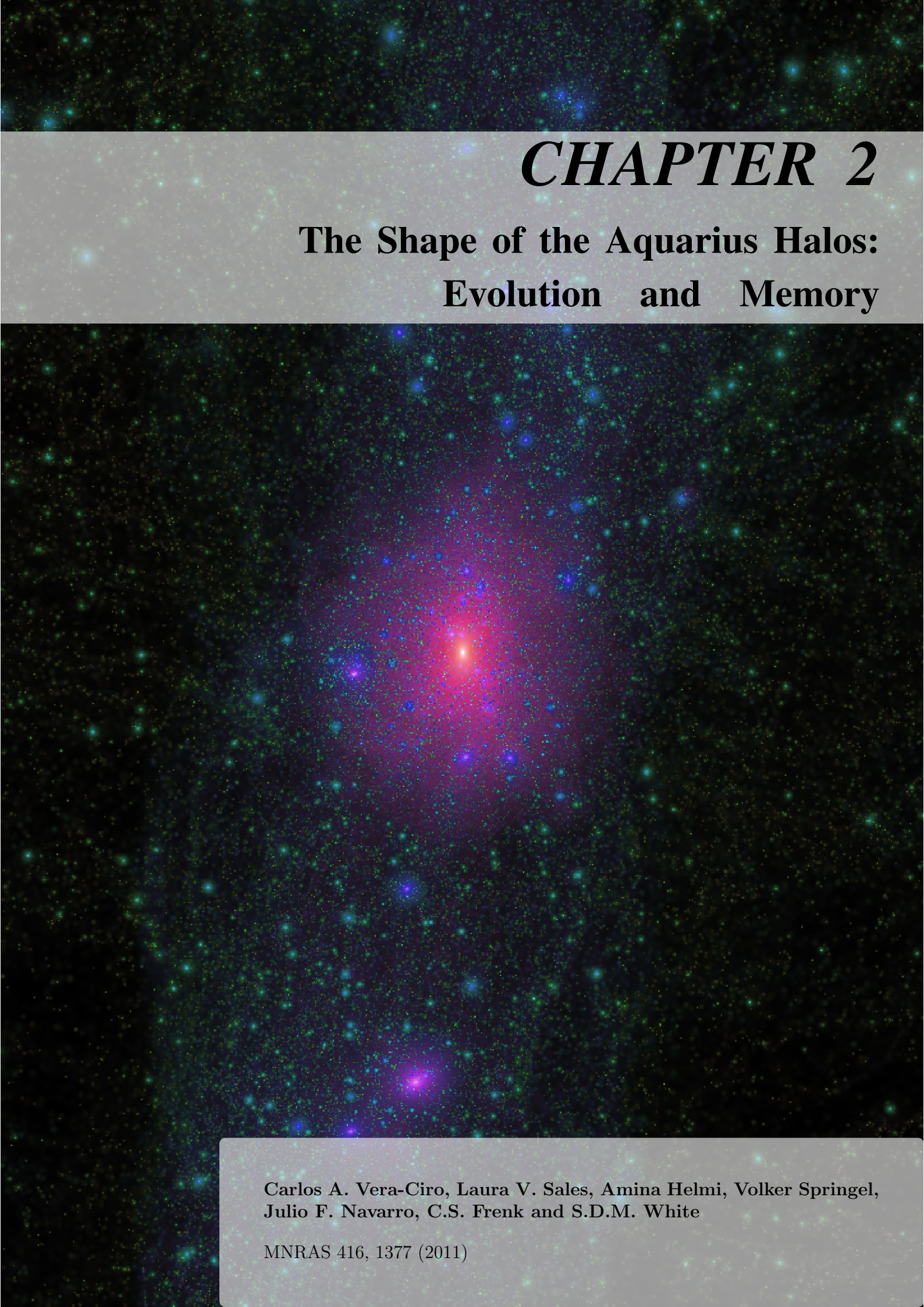

CHAPTER 2

The Shape of the Aquarius Halos: Evolution and Memory

Carlos A. Vera-Ciro, Laura V. Sales, Amina Helmi, Volker Springel, Julio F. Navarro, C.S. Frenk and S.D.M. White

MNRAS 416, 1377 (2011)

Abstract

We use the high resolution cosmological N-body simulations from the Aquarius project to investigate in detail the mechanisms that determine the shape of Milky Way-type dark matter halos. We find that, when measured at the instantaneous virial radius, the shape of individual halos changes with time, evolving from a typically prolate configuration at early stages to a more triaxial/oblate geometry at the present day. This evolution in halo shape correlates well with the distribution of the infalling material: prolate configurations arise when halos are fed through narrow filaments, which characterizes the early epochs of halo assembly, whereas triaxial/oblate configurations result as the accretion turns more isotropic at later times. Interestingly, at redshift $z = 0$, clear imprints of the past history of each halo are recorded in their shapes at different radii, which also exhibit a variation from prolate in the inner regions to triaxial/oblate in the outskirts. Provided that the Aquarius halos are fair representatives of Milky Way-like $10^{12}\mathrm{M}_{\odot}$ objects, we conclude that the shape of such dark matter halos is a complex, time-dependent property, with each radial shell retaining memory of the conditions at the time of collapse.

Cover: Aq-A-2 halo rotated using the principal axis of the virial contour at $z = 0$

2.1 Introduction

In our current understanding of the Universe, dark matter halos constitute an integral part of galaxies. Their properties, especially their density profile and shape, have received significant attention in recent years as they have been argued to be sensitive to the fundamental properties of the dark matter particles. Numerical simulations have been extensively used to study the characteristics of the dark matter halos, exploring for example the effects of the environment, mass assembly history and the nature of dark matter itself (e.g., Bullock, 2002; Bett et al., 2007; Macciò et al., 2007; Hahn et al., 2007b; Spergel & Steinhardt, 2000; Yoshida et al., 2000; Avila-Reese et al., 2001; Strigari, Kaplinghat & Bullock, 2007; Wang & White, 2009).

The first fully analytical models of the formation of dark matter halos such as the top-hat spherical collapse model (Gunn & Gott, 1972; Fillmore & Goldreich, 1984), considered highly symmetric configurations. However, the pioneering work of Frenk et al. (1988); Dubinski & Carlberg (1991); Warren et al. (1992); Cole & Lacey (1996); Thomas et al. (1998) demonstrated important deviations from spherical symmetry by measuring the shape of dark matter halos in numerical N-body simulations evolved in a fully cosmological context. These authors consistently found that after virialization, dark matter halos are triaxial with more prolate shapes towards the center and more oblate shapes in the outskirts. Recent high resolution N-body simulations have yielded similar conclusions (Jing & Suto, 2002; Bailin & Steinmetz, 2005; Kasun & Evrard, 2005; Hopkins, Bahcall & Bode, 2005; Bett et al., 2007; Hayashi, Navarro & Springel, 2007; Kuhlen, Diemand & Madau, 2007; Stadel et al., 2009; Diemand & Moore, 2011).

Further studies based on numerical simulations have also revealed that the environment and mass assembly history of a halo may play a crucial role in determining its shape. Pioneering work by Tormen (1997) and Colberg et al. (1999) suggested that the anisotropic infall of matter onto cluster-sized halos was largely responsible for their shape, orientations and dynamics at different times. Because infall is governed by the surrounding large scale structure, we expect significant correlations between the halo shapes and their environment, although evidence both against and in support of such trends have been reported so far in the literature (Lemson & Kauffmann, 1999; Avila-Reese et al., 2005; Faltenbacher et al., 2005; Altay, Colberg & Croft, 2006; Basilakos et al., 2006; Gottlöber & Turchaninov, 2006; Patiri et al., 2006; Aragón-Calvo et al., 2007b; Hahn et al., 2007a; Macciò et al., 2007; Ragone-Figueroa et al., 2010).

The observational determination of the shapes of dark matter halos is challenging. Preferably dynamical tracers at large radii are to be used, but these tracers are by definition rare. In external galaxies, constraints on these shapes have been put using the intrinsic shape of galactic disks (Fasano et al., 1993), the kinematics and morphology of the HI layer (Olling, 1996; Becquaert &

Combes, 1997; Swaters, Sancisi & van der Hulst, 1997), the morphology, temperature profile of X-ray isophotes (Buote & Canizares, 1998; Buote et al., 2002), gravitational lensing (Hoekstra, Yee & Gladders, 2004) and the spatial distribution of galaxies within groups (Robotham, Phillipps & De Propris, 2008) (for earlier reviews on the subject see Rix, 1996; Sackett, 1999). The general consensus of all these studies is that halos tend to be roughly oblate, with the smallest axis pointing perpendicular to the symmetry plane defined by the stellar component. Most of these constrains, however, pertain to the inner regions (a few optical radii) of galaxy-scale halos.

In the case of the Milky-Way, the shape constraints often rely on the kinematics of individual stars, and include e.g. the use of the tilt of the velocity ellipsoid for nearby stars (Siebert et al., 2008), the proper motions of hypervelocity stars (Gnedin et al., 2005) or the dynamics of stellar streams (Koposov, Rix & Hogg, 2010). Interestingly, the use of the latter have provided contradictory results, notably in the case of the Sagittarius Stream. For example, the positional information was used to argue that the Milky Way halo is nearly spherical (Ibata et al., 2001; Martínez-Delgado et al., 2004; Johnston, Law & Majewski, 2005) whereas the kinematics of stars in the leading stream could only be fit in a prolate halo elongated perpendicular to the disk (Helmi, 2004; Law, Johnston & Majewski, 2005). More recently, Law, Majewski & Johnston (2009); Law & Majewski (2010) have explored triaxial potentials with constant axis ratios, and found models that were able to fit simultaneously these constraints, albeit not completely satisfactorily.

From the theoretical perspective, there is a gap in our knowledge about the way in which dark matter halos acquire their shape, and in particular, on the impact of the dynamics of the surrounding large scale structure in the non-linear regime (Lee, Jing & Suto, 2005; Betancort-Rijo & Trujillo, 2009; Rossi, Sheth & Tormen, 2010; Salvador-Solé et al., 2011). Indeed, most of the theoretical works cited above restrict their analysis to the present day correlations with the environment, and do not consider when the shapes have been established and how they relate to the past history of an object. In this Chapter we use state-of-the-art high resolution N-body simulations that track the formation of five $\sim 10^{12}\mathrm{M}_{\odot}$ Milky Way-like halos in a fully cosmological context, in order to gain further understanding of this problem.

This Chapter is organized as follows. In Sec. 2.2 we describe the simulations used in this work which are part of the Virgo Consortium's *Aquarius* project, and test in Sec. 2.3 the convergence of halo shapes for different resolutions. The shapes at the present day, evolution and their relation with the formation history of the dark matter halos are analyzed in Sec. 2.4 and 2.5. Finally, we discuss and summarize our main conclusions in Sec. 2.6. For completeness, we compare in Appendix 2.7 the results obtained by using several different schemes to determine halo shapes. Also a novel method for measuring the size of the filaments based on dynamical arguments is described in Appendix 2.8.

2.2 Numerical Simulations

We use the Aquarius Simulations, a suite of high resolution N-body cosmological simulations of six Milky Way sized dark matter halos (Springel et al., 2008). These halos were selected from a larger ΛCDM cosmological box of $100h^{-1}$ Mpc side with parameters $\Omega_m = 0.25$, $\Omega_\Lambda = 0.75$, $\sigma_8 = 0.9$, $n_s = 1$ and $H_0 = 100h$ km s^{-1}Mpc^{-1} = 73 km s^{-1}Mpc^{-1}. The Aquarius halos, labeled `Aq-A` to `Aq-F`, have a final mass $\sim 10^{12}$M$_\odot$ and were chosen to be relatively isolated at redshift $z = 0$. The selection procedure was otherwise random, which allows us to study the impact of different assembly histories on the shape of Milky Way sized dark matter halos.

Each halo has been re-simulated at various resolution levels that accurately replicate the power-spectrum and phases for the resolved structures in all runs. Following the notation introduced in previous papers, we refer to each level of resolution as -5 to -1, for the lowest to highest resolution. The mass per particle varies from $m_p = 2.94 \times 10^6 h^{-1}M_\odot$ in the level 5 to $m_p = 1.25 \times 10^3 h^{-1}M_\odot$ for the highest resolution run, which resolves a given halo with approximately half-million up to 1.5-billion particles within the virial radius for level 5 and 1, respectively[1]. The results discussed in this Chapter pertain mostly to the 4th level of resolution ($m_p \sim 2 \times 10^5 h^{-1}M_\odot$, $n_{\rm vir} \sim 10^6$ particles within $r_{\rm vir}$, gravitational softening $\epsilon = 250h^{-1}$ pc) of halos `Aq-A` to `Aq-E` and aim to target the possible structure of the Milky Way dark matter halo. The Aquarius halo `Aq-F` is not considered in this work because it experiences a major merger less than ~ 5 Gyr ago; this is unlikely to be consistent with our current view of the assembly of the Milky Way halo, expected to have had no major mergers since $z \sim 1$ (Toth & Ostriker, 1992).

In this context, this Chapter focuses on dark matter halos with a relatively quiescent merger history (mass ratios lower than 1:5) after $z \sim 2$ (for a detailed comparison of the Aquarius halos' mass accretion history with respect to the general expectations for halos of similar virial mass see Boylan-Kolchin et al., 2010). We summarize the most relevant numerical details of our halos at level 4 in Table 2.1, and we refer the interested reader to Springel et al. (2008) for further information.

2.3 Halo shape determination and convergence

Various methods have been introduced in the literature to measure the shapes of dark matter halos. In Appendix 2.7 we describe a wide range of these

[1]Throughout this Chapter we refer to the virial radius, $r_{\rm vir}$, as the spherical radius that contains a mean density equal to 200 times the critical density of the Universe at a given time. Other virial quantities, such as mass and velocities, $m_{\rm vir}$ and $v_{\rm vir}$ respectively, correspond to those measured within $r_{\rm vir}$.

Halo	m_p	$r_{\rm vir}$	$m_{\rm vir}$	$n_{\rm vir}/10^6$	$r_{\rm conv}$
Aq-A-4	2.87	179.36	1.34	4.68	2.27
Aq-B-4	1.64	137.86	0.61	3.72	2.14
Aq-C-4	2.35	177.89	1.31	5.58	2.07
Aq-D-4	1.95	177.83	1.31	6.69	2.14
Aq-E-4	1.90	155.95	0.88	4.64	2.05

Table 2.1: Numerical details of the Aquarius halos for resolution level-4. Each column lists: (1) the name of the halo, (2) mass per particle m_p in $10^5 {\rm M}_\odot\ h^{-1}$, (3) the virial radius $r_{\rm vir}$ in kpc h^{-1} and (4) virial mass $m_{\rm vir}$ in $10^{12} {\rm M}_\odot\ h^{-1}$ at $z = 0$, (5) $n_{\rm vir}$ the number of dark matter particles within $r_{\rm vir}$, (6) $r_{\rm conv}$ the convergence radius in kpc h^{-1}. The gravitational softening length is $\epsilon = 250 h^{-1}$ pc for all halos at this resolution level.

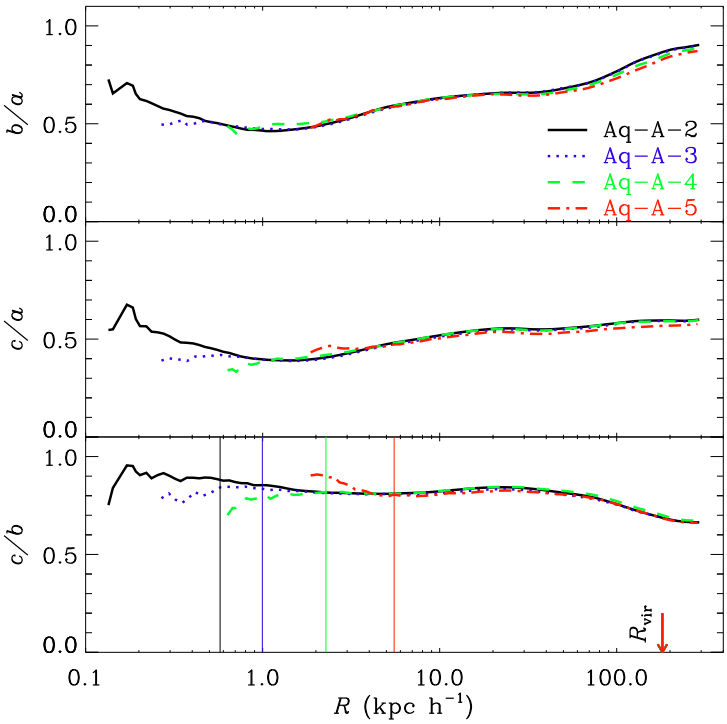

Figure 2.1: Convergence in the axis ratios for the Aq-A halo at four different numerical resolutions. The agreement is remarkable showing that the method used provides reliable axis ratios down to the "convergence radius" $r_{\rm conv}$ (denoted by the vertical lines).

methods in detail, and show that the measured halo shapes agree reasonably well when applied to the same object. Throughout this article we use the "reduced" inertia tensor method as implemented recently by Allgood et al.

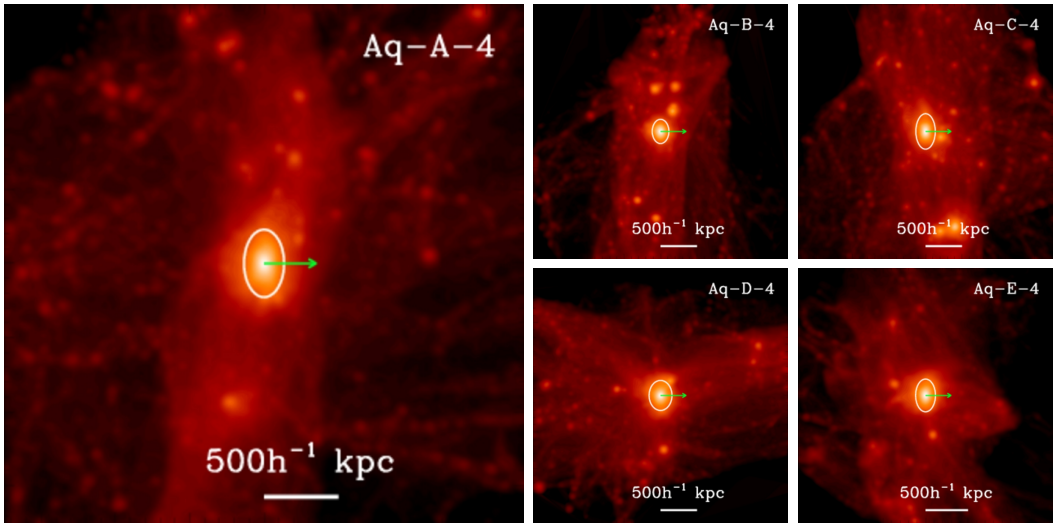

Figure 2.2: Present day dark matter distribution of the Aquarius halos and their surroundings. Colors are proportional to the logarithm of the squared dark matter density integrated along the line of sight. In each panel the depth of the projected image is $1.5h^{-1}$ Mpc. The virial ellipsoid is indicated in each panel with a solid white line and the green arrow shows the direction of the minor axis of the halo at the virial contour. The system is orientated such that the minor axis points horizontally and the major axis points vertically.

(2006). This tensor is defined as

$$I_{ij} = \sum_{\boldsymbol{x}_k \in V} \frac{x_k^{(i)} x_k^{(j)}}{d_k^2}, \tag{2.1}$$

where d_k is a distance measure to the k-th particle and V is the set of particles of interest. Assuming that dark matter halos can be represented by ellipsoids of axis lengths $a \geq b \geq c$, the axis ratios $q = b/a$ and $s = c/a$ are the ratios of the square-roots of the eigenvalues of $\boldsymbol{I}$, and the directions of the principal axes are given by the corresponding eigenvectors. Initially the set V is given by all particles located inside a sphere which is re-shaped iteratively using the eigenvalues of $\boldsymbol{I}$. The distance measure used is $d_k^2 = x_k^2 + y_k^2/q^2 + z_k^2/s^2$, where q and s are updated in each iteration. Furthermore, in the figures below we have removed all bound substructures contained in a halo using the SUBFIND algorithm (Springel et al., 2001). This alleviates the noise and artificial tilting of the ellipsoids that is introduced by such substructures. More details on our implementation can be found in the Appendix 2.7.

We test the convergence of the shape measurements using the different resolutions of the halo `Aq-A`, from level 5 to level 2. There is an increase of a factor ~ 230 in the number of particles within the virial radius and a factor ~ 10 reduction in gravitational softening from `Aq-A-5` to `Aq-A-2`. Fig. 2.1

shows the axis ratios as a function of R for halo `Aq-A`, where R is defined as the geometrical mean of the axis lengths $R = (abc)^{1/3}$. This quantity then provides a notion of distance to the center of the ellipsoid with the advantage of being volume invariant. Hereafter, we use R when referring to quantities measured using ellipsoidal contours, and r for spherical contours. With this convention, $r_{\rm vir}$ is the spherical radius enclosing an average overdensity of 200 times the critical value, whilst $R_{\rm vir}$ refers to the ellipsoid enclosing the same overdensity.

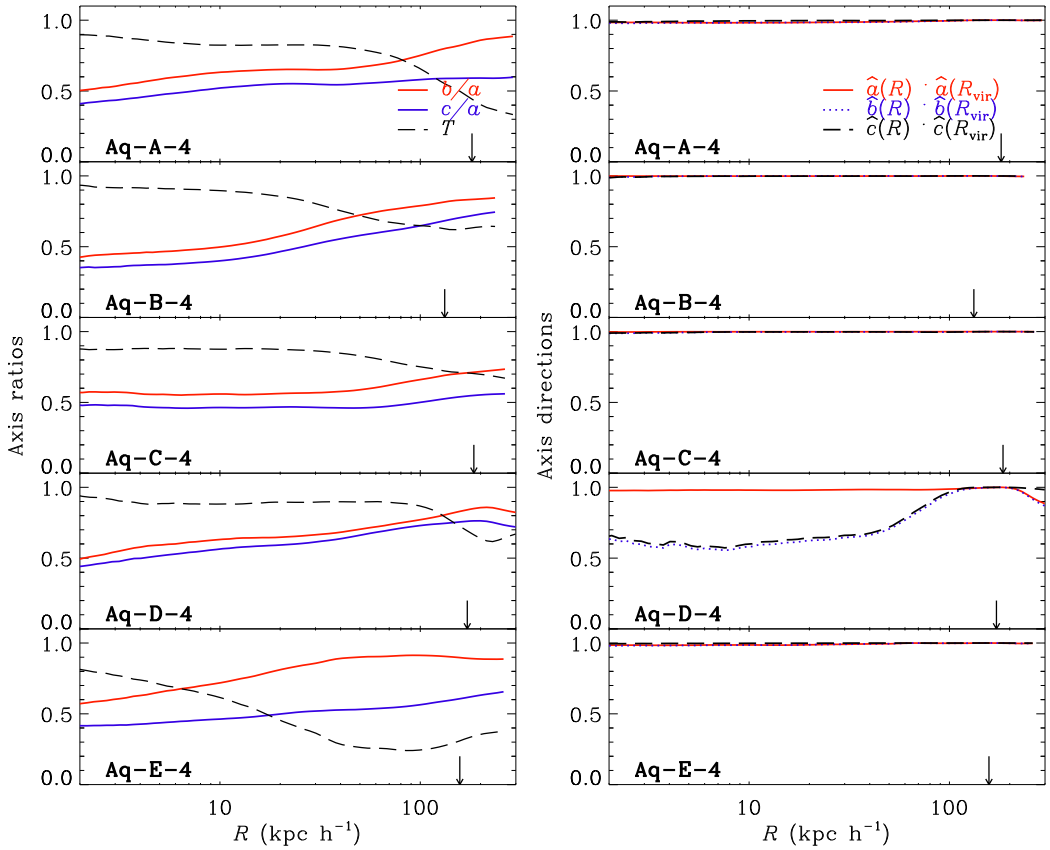

Figure 2.3: Axis ratios (left) and directions (right) as a function of R for each of the Aq-halos. In the left panels the thick solid lines represent the axis ratios b/a (red) and c/a (blue), while the dashed curves are the triaxiality parameter T. In general halos are more prolate in the inner parts and more oblate (and triaxial) in the outskirts. All concentric shells are also strongly aligned with the exception of halo `Aq-D` which exhibits a clear twisting close to the virial radius.

The agreement between the different resolutions in Fig. 2.1 is remarkable at all radii, although small deviations are present in the inner regions where resolution effects are expected to be important. The vertical lines in the lower panel indicate the "convergence radius" $r_{\rm conv}$ (Power et al., 2003; Navarro et al.,

2010). This radius is defined by setting $\kappa(r_{\rm conv}) = t_{\rm relax}(r_{\rm conv})/t_{\rm circ}(r_{\rm vir}) = 7$, where $t_{\rm relax}$ is the local relaxation time and $t_{\rm circ}(r_{\rm vir})$ corresponds to the circular orbit timescale at $r_{\rm vir}$. This choice ensures that circular velocity profiles for $r > r_{\rm conv}$ deviate less than 2.5% from the highest resolution value. Fig. 2.1 shows that $r_{\rm conv}$ provides also a very good estimate for the smallest radius at which the halo shape has converged. Although not explicitly shown, we have tested that the orientation of the ellipsoids is a well defined attribute independent of resolution for $r_{\rm conv} < R < R_{\rm vir}$.

Our analysis suggests that convergence in halo shapes is achieved in the level 4 from approximately $2h^{-1}$ kpc onwards (Table 2.1). We will therefore focus in what follows on the study of the different Aquarius halos `Aq-A` to `Aq-E` at the level of resolution 4, since this yields a robust characterization of the dark matter halo shapes and orientation, while keeping the numerical cost constrained.

2.4 The shape of dark matter halos

2.4.1 Present day

Fig. 2.2 shows a snapshot view of the Aquarius halos and their surrounding environment. The color scale used is proportional to the logarithm of the squared dark matter density integrated along the line of sight, with a projection depth per panel of $1.5h^{-1}$Mpc. All images have been rotated according to the orientation of the virial contours (indicated by the solid white curve) in such a way that the major and minor axis define the vertical and horizontal direction, respectively.

A careful look at the environment of each object reveals that the Aquarius halos are all embedded within a filamentary-like structure, which is better defined in some cases than in others (e.g. Fig. 2.2 `Aq-A` vs `Aq-E`), a result that holds independently of the projection used. These filaments also seem to contain the most massive substructures in the box and interestingly, the minor axes of the virial contours tend to be perpendicular to the direction defined by these. This is in very good agreement with the statistical findings of Bailin & Steinmetz (2005), who analyzed a sample of ~ 4000 halos in a wide range of masses. One relevant consequence of this type of configuration is that most of the substructure will preferentially be accreted along the *major* axis of the halo, a feature that has been used to explain the preferential alignment of satellite galaxies with respect to their hosts in observational studies of external galaxies (e.g. Brainerd, 2005, and references therein), in groups (e.g. Binggeli, 1982; Kitzbichler & Saurer, 2003; Yang et al., 2006; Faltenbacher et al., 2007; Godłowski & Flin, 2010; Paz et al., 2011) and also numerical simulations (e.g. Knebe et al., 2004; Libeskind et al., 2005, 2007; Kang et al., 2007; Sales et al., 2007; Bailin et al., 2008; Faltenbacher et al., 2008; Libeskind et al., 2011).

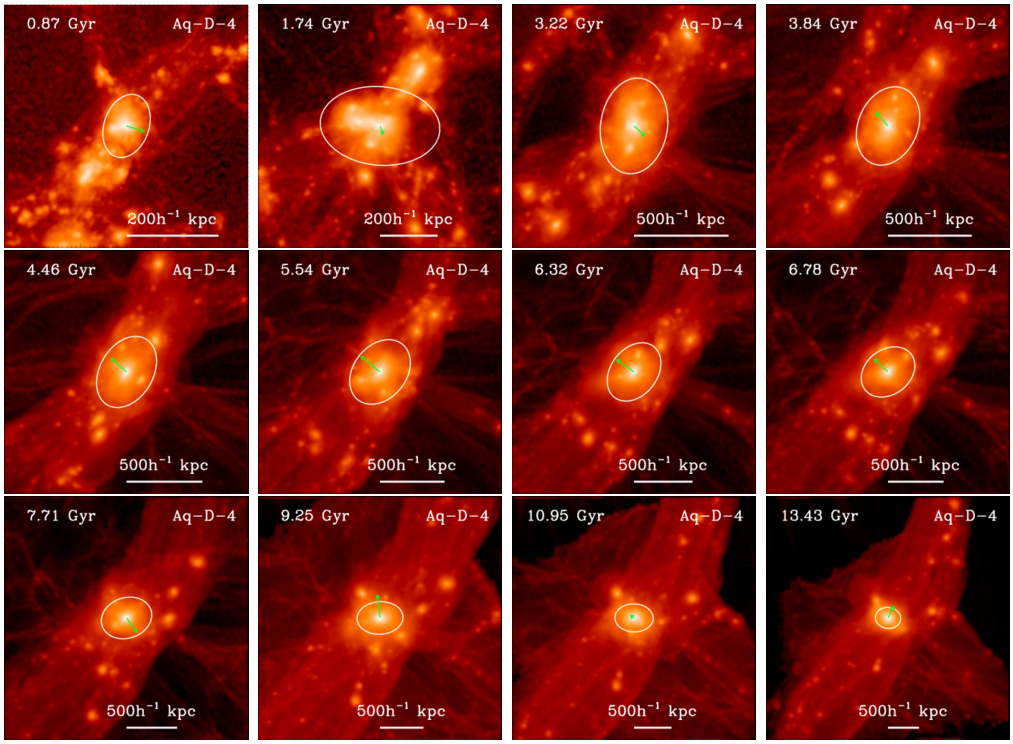

Figure 2.4: Time sequence of the formation of halo `Aq-D` from $t \sim 1$ Gyr to the present day. Each box shows the dark matter density distribution around this halo together with the shape and orientation of the virial contour at the given time. As before, the green arrows indicate the projection of the minor axis onto the plane, with the length of the arrow being proportional to the minor axis length. The shape of this halo evolves continuously with time, showing stretching and tilting in response to the infall of matter. The halo is oriented along the filament up to $t \sim 7$ Gyr and then rotates and becomes perpendicular to it at the present day. This figure clearly illustrates the complexity involved in the build up of the present day dark matter halo's structure.

The halo shapes and orientations as a function of radius are shown in Fig. 2.3. On the right panel, besides the axis ratios, we also plot the triaxiality parameter T defined as

$$T = \frac{a^2 - b^2}{a^2 - c^2}, \tag{2.2}$$

which is unity for a perfect prolate distribution and zero in the oblate case (Franx, Illingworth & de Zeeuw, 1991; Warren et al., 1992). This figure shows that in the inner regions all dark matter halos are more "prolate" with $b/a \sim c/a \sim 0.4$–0.6 (Hayashi, Navarro & Springel, 2007). On the other hand, at large radii b/a increases to 0.8–0.9, and the mass distribution becomes more oblate/triaxial. At intermediate radii halos are typically triaxial, but notice that the radius at which the prolate-to-oblate transition occurs (defined as the

radius where $T = 0.5$) is different for each object, ranging from $\sim 20h^{-1}$ kpc for `Aq-E` to $\sim 100h^{-1}$ kpc in the case of `Aq-A`.

Regardless of the change in shape of the concentric ellipsoids, these tend to remain well aligned throughout the halo. The right panel of Fig. 2.3 shows the cosines of the relative angle between the major, intermediate and minor axis of the ellipsoids at different radii and at the virial contour. The alignment is remarkable, with the exception of halo `Aq-D`, where the intermediate and minor axis in the inner regions are rotated $\sim 60^\circ$ with respect to their orientation at the virial radius, an issue that we explore in the next section.

2.4.2 Evolution

Fig. 2.4 shows a series of snapshots of halo `Aq-D` at different stages of its evolution. The orientation of the coordinate system is now kept fixed for all the snapshots. The corresponding time is quoted in the upper left corner of each panel, the virial ellipsoids are depicted by white ellipses while the projection of the minor axes onto the plane are indicated by the green arrows. There are several points worth highlighting:

- The shape and orientation of the halo seem to change throughout time (with the caveat that we are just seeing its evolution in *projection*).

- Also evident from this figure is the filamentary structure that characterizes the surroundings of `Aq-D`. Notice that the filament where this halo is located at the present day was already in place at $t \lesssim 1$ Gyr, and fully dominates the environment from $t \sim 3$ Gyr onwards, with remarkable coherence in time and direction.

- The relative orientation of halo `Aq-D` with respect to its environment is interesting since its minor axis is *parallel* to the direction of the filament at late times. This seems to be at odds with expectations from statistical studies of dark matter halo alignments (Bailin & Steinmetz, 2005; Faltenbacher et al., 2005; Aragón-Calvo et al., 2007a; Zhang et al., 2009) as well as in contradiction with the other halos illustrated in Fig. 2.2 and the analysis presented in Section 2.4.1. A closer inspection of the history of this halo shows that the infall of material at $t \gtrsim 7.5$ Gyr occurs mostly along a secondary filament (only barely visible in this projection) whose direction is almost perpendicular to that of the most prominent and massive filament that dominates the surrounding large scale structure and is clearly seen in Fig. 2.4. This change of infall direction explains the apparent change in orientation of halo `Aq-D` at late times.

- The relative size of a filament with respect to that of the halo increases with time: the filament's cross section is comparable to the virial radius at $t \lesssim 5$ Gyr, whereas the dark matter halo becomes smaller than and

is fully embedded in the filament at later times. This has interesting consequences on the halo shape as we discuss further in Section 2.5. We have explicitly checked that this conclusion is not dominated by projection effects nor rendering of our images. We refer the reader to Appendix 2.8, where we introduce a physically motivated definition of a filament (based on the number of caustic-crossings a particle has experienced) and compare its size with that of the halo at each timestep.

In Fig. 2.5 we quantify the time evolution of the axis ratios measured at the instantaneous virial ellipsoids for halos `Aq-A` to `Aq-E`. For reference, we have indicated with grey labels the corresponding physical sizes at a given time. We will only follow the evolution from $t = 2$ Gyr onwards (which corresponds roughly to the time at which the halos have $\sim 20\%$ of their final mass), which guarantees that the center of mass as well as the shapes at the virial radius are well defined at all times for the full sample of halos.

Fig. 2.5 shows that the shape of the virial ellipsoids is not constant with time. In general, halos seem to evolve from a quite prolate configuration at early times towards more triaxial shapes at the present day. In most of our halos (with the exception of `Aq-D`), this evolution in shape is driven by a larger increase of the intermediate-to-major axis ratio b/a than in c/a. Except for this weak general trend, the evolution of the axis ratios is quite disparate from halo to halo.

A qualitative comparison between the left panel of Fig. 2.3 and 2.5 suggests a certain degree of resemblance between the overall evolution of the virial ellipsoid's shape with time (as measured, for example, by the triaxiality parameter) and the shapes measured as a function of radius (Fig. 2.3) for each of our halos, despite their intrinsic differences. This suggests that the dark matter halos retain certain *memory* of their configuration in the past, and that this is imprinted on their present day structure. We note however that this refers to the overall *trend* with radius/time and does not imply that it is possible to recover the *exact* numerical value of the axis ratios at a given time from their present day value at a given radius.

This analogy between radius/time is better seen in Fig. 2.6, where we plot the present day axis ratios b/a vs c/a at different radii (grey curve) as well as those measured at the virial ellipsoids for different times (color points). Because we sample from $t = 2$ Gyr onwards, a dotted or a solid line is used to indicate respectively, the shapes at radii smaller or larger than the virial ellipsoid $R_{\rm vir}$ at this time. This figure shows that halos evolve away from the 1:1 line and therefore tend towards less prolate shapes with time (and also radius), with the clear exception of halo `Aq-D`. Moreover, the reasonable agreement between the solid curve and the diamonds in this figure suggests that the present day shape of the dark matter halos at different radii provides information about the evolution of the virial ellipticities during their assembly history.

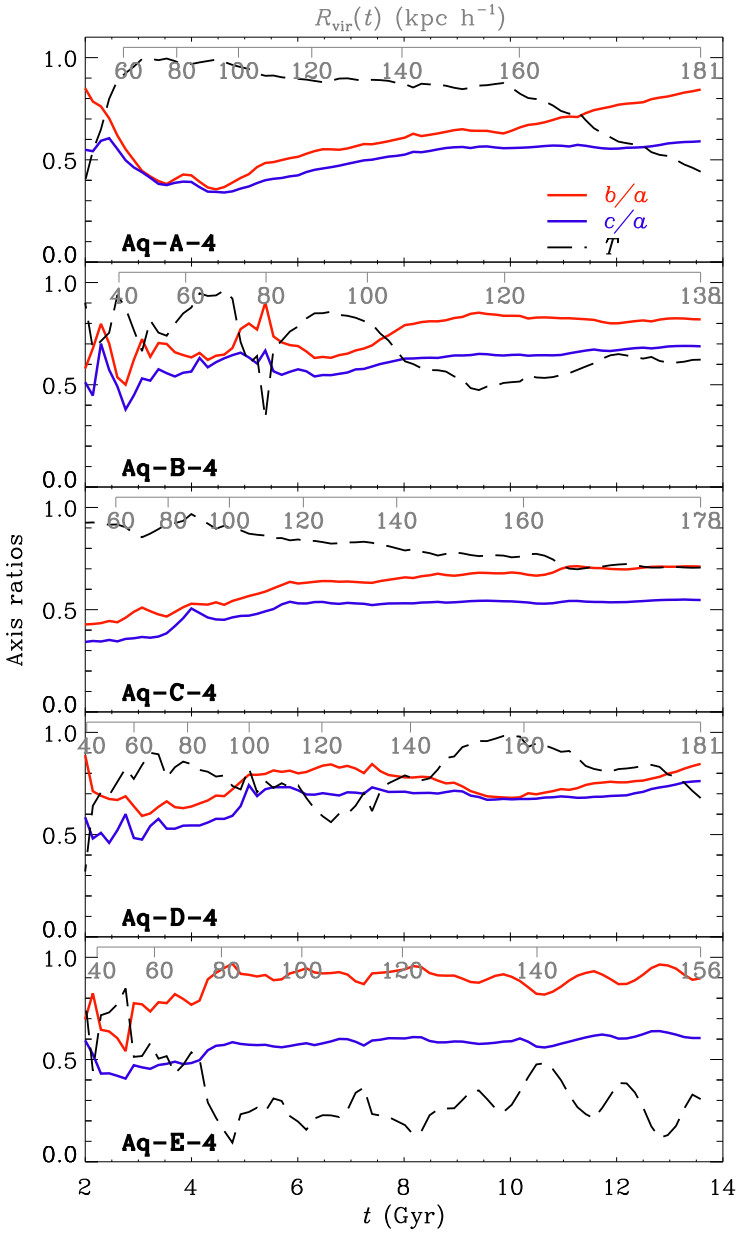

Figure 2.5: Temporal evolution of the axis ratios and triaxiality parameter for the virial contour. The color-coding is the same as in Fig. 2.3. A comparison to that figure shows that a correlation exists between the shape as a function of time, and the present-day shape as a function of radius. To aid this comparison we have added a second axis (gray), indicating the size of the virial contour $R_{\rm vir}$. This is derived for each halo by fitting: $R_{\rm vir}(t) = A(1 - {\rm e}^{(t-\tau)/(2t_h)})$ to the measured evolution of the virial (ellipsoidal) radius. Here t_h is the time at which the virial mass reaches half its present value, and A and τ are free parameters.

The analysis presented in this section, if generalized to Milky Way-type halos, is directly relevant to the modeling and interpretation of observational constraints on the shape of the Galactic potential. As discussed in the Introduction, the Sagittarius stream has led to contradictory results when modeled in axisymmetric dark matter halos with constant axis ratios (in the potential) (Ibata et al., 2001; Helmi, 2004; Law, Johnston & Majewski, 2005; Johnston, Law & Majewski, 2005; Fellhauer et al., 2006). We have shown here that significant variations in the axis ratios as a function of radius exist for all our five Aquarius halos and those variations are linked to the evolutionary history of each object. Although this might add an extra degree of freedom to models that attempt to constrain the Galactic potential, our results from Fig. 2.6 indicate that by doing so it may be possible to retrieve the local conditions around the Milky Way's halo throughout its assembly (Banerjee & Jog, 2011).

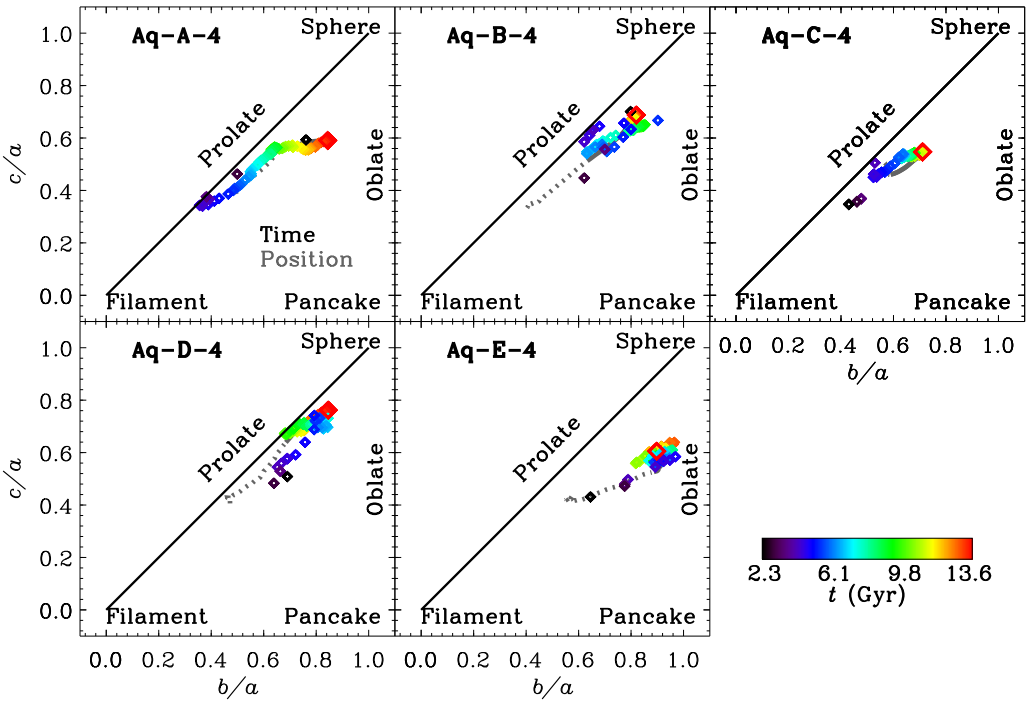

Figure 2.6: Axis ratios as a function of position (gray line) and time (diamonds). The colors indicate the time when the axis ratios at the virial contour have been measured. Notice that since we consider temporal evolution only after $t = 2$ Gyr, we have differentiated the shape as a function of position (gray curve) using solid (dotted) lines for distances larger (smaller) than the virial radius of each halo at $t = 2$ Gyr (see text for details).

2.5 Environment, Mass Accretion and Halo Shapes

Dark matter halos continue to grow with time, through a regular, although not always steady, injection of matter. Halos will respond to this new material and re-structure themselves onto a new equilibrium configuration as part of the virialization process. The environment of an object determines to some extent the way in which the material is incorporated into the halo. For instance, thin filaments imply accretion through well-defined preferential directions whereas a more isotropic mode is expected when the halo is embedded in a larger structure. Several correlations of halo shapes with environment have been found so far in simulations (e.g. Avila-Reese et al., 2005; Faltenbacher et al., 2005; Patiri et al., 2006; Basilakos et al., 2006; Macciò et al., 2007; Hahn et al., 2007a) and observations (e.g. Pimbblet, 2005; Godłowski & Flin, 2010; Niederste-Ostholt et al., 2010; Paz et al., 2011), albeit with significant scatter. In this section we explore in detail the role played by the environment and mass assembly histories in shaping the Aquarius halos.

The angular distribution on the sky of the infalling matter can provide useful information about the preferred directions and modes of the ongoing accretion (Tormen, 1997; Colberg et al., 1999; Aubert, Pichon & Colombi, 2004; Aubert & Pichon, 2007; Libeskind et al., 2011). For instance, whereas isotropic accretion would lead to a uniform signal on the sky, the presence of a thin filament will give rise to a bi-modal distribution of points in two opposite (180° apart) directions. This can be quantified further by means of a multipole expansion of the infalling particles on the sky at a given time. We measure the power spectrum for the mode l as,

$$C_l = \frac{1}{4\pi}\frac{1}{2l+1}\sum_{m=-l}^{l}|\tilde{a}_l^m|^2, \tag{2.3}$$

where the expansion coefficients are,

$$\tilde{a}_l^m = \frac{m}{4\pi r_{\rm vir}^2}\sum_{k=1}^{N}(Y_l^m(\Omega_k))^*, \tag{2.4}$$

with Ω_k being the angular position of the k-th particle crossing the virial radius $r_{\rm vir}$ with negative radial velocity at any given time. The asterisk on the right hand side of Eq. (2.4) indicates the complex conjugate of the term within parenthesis.

In the scheme introduced above, the $l = 0$ term (monopole) is a constant equal to unity and used for the overall normalization of the expansion. Notice that although this choice is arbitrary, the *relative* relevance of the monopole with respect to all the other modes, $C_0/\Sigma_l C_l$, is an indication of how isotropic

the distribution is; i.e. a perfectly isotropic infall would correspond to all the power in the $l = 0$ term. On the other hand, a significant contribution of the $l = 2$ (or quadrupolar moment) term arises when the accretion occurs through a well-defined direction in space, i.e. a filament. Similarly, accretion corresponding to more than one preferential direction will shift the power away from $l = 2$ and towards higher moments. Notice that a point mass on the sky will excite, by definition, a wide range of modes with similar power; just like the Fourier transform of a Dirac-delta function has constant power for all modes in the frequency space. We therefore expect single satellite infall events to excite higher moments compared to the smooth accretion. In the limit of a satellite that occupies a large area of the sky, the configuration will then resemble a dipole and the power spectrum will exhibit high power in the $l = 1$ mode.

In practice, most of the information is encoded in the terms $l \leq 2$ (e.g. Quinn & Binney, 1992; Eisenstein & Loeb, 1995; Aubert, Pichon & Colombi, 2004). We have checked in our experiments that higher moments than quadrupolar contribute always less than $\sim 15\%$ of all power at any given time once substructures have been removed. We therefore focus our analysis mostly on the $l = 0$ and $l = 2$ moments since they provide most of the information that allow to characterize the mass accretion onto dark matter halos.

Fig. 2.7 shows this multipole decomposition introduced in Eq. (2.3) of the mass infalling onto `Aq-A-4` as a function of time. At each output time, we select particles with negative radial velocity (infalling), $v_r < 0$, that are in the spherical shell $1.0 \leq r/r_{\rm vir} \leq 1.2$ and compute the corresponding C_l of the distribution[2]. The upper and the middle panels of this figure show the C_l power spectra obtained respectively, by including and by removing particles associated with substructures as identified by SUBFIND. Both distributions are quite similar, although as expected from the discussion in the previous paragraph, satellite accretion excites in general higher modes that last a very short timescale, and are visible as clear "spikes" in the upper panel of the figure.

The virialized regions of galaxy-sized objects can extend well beyond their formal $r_{\rm vir}$ (e.g. Cuesta et al., 2008), introducing a signal in the power spectrum that is driven by the halo's intrinsic shape rather than by the surrounding infall pattern. In order to avoid confusion with the material already in place and in equilibrium in the outskirts of the halo, we selected also the subsample of particles within $1.0 \leq r/r_{\rm vir} \leq 1.2$ that are infalling for the *first time* onto the halo (in practice we do this by requiring that a particle in a given output has never been within the virial radius of the main object at any previous time step). The corresponding power spectrum (after removing the subhalos' contribution) is shown in the bottom panel of Fig. 2.7. This distribution agrees

[2]We have tested that the qualitative behavior shown in this figure and the relative relevance of each mode with respect to the whole spectrum does not depend on the particular shell that is analyzed for $1 < r/r_{\rm vir} < 2$ for all of our halos.

well with those shown in the other panels of this figure, although the features appear noisier due to the smaller number of particles being considered.

The left panel of Fig. 2.8 shows the power spectrum of all infalling material for all five Aquarius halos after the contribution from subhalos has been removed. The residual "spikes" visible in this figure correspond to the matter that is associated to infalling substructures but that is rather loose and, consequently, has not been assigned to a particular subhalo by the halo finder.

The right panel of Fig. 2.8 shows the relative contribution of the $l = 2$ (solid black curve) and $l = 0$ (blue dot-dashed) moments to the total power spectrum as a function of time[3]. These have been computed using only the subset of particles on their first infall (although these curves do not change significantly when all infalling particles are considered instead). Large C_2 values are associated with the presence of net filamentary accretion. Fig. 2.8 shows that this condition is typically found at early times in our halos, with the exception of `Aq-B`, which shows no clear sign of smooth accretion through a filament at any time. The halo `Aq-D` shows also a peculiarly high power in the $l = 2$ mode at late times, whereas for most of the objects the relevance of C_2 remains approximately flat (and negligible) in the last few Gyr (a feature which is also evident in the left panel of Fig. 2.8).

The monopole term largely dominates the accretion at later times (blue dot-dashed curve in Fig. 2.8) in all halos. Exceptions are halos `Aq-A` and `Aq-D`, which show a decline in $C_0/\Sigma C_l$ beyond $t \sim 12$ Gyr and $t \sim 10$ Gyr respectively. In the case of `Aq-A` this is related to an increase in power of $l \geq 2$ modes, while for `Aq-D` this is driven only by the $l = 2$ moment, as mentioned in the previous paragraph. As we show in Appendix 2.8, this more isotropic infall is a direct consequence of the increase in the relative size of the filaments feeding the dark matter halos: infalling particles cover wider angles on the sky which leads to larger C_0 contributions with negligible $l = 2$ component. Notice that halo `Aq-E` is, in some sense, the most extreme object, with a monopolar term that dominates the power spectrum of infall material during almost all its entire history ($C_0/\Sigma_l C_l > 0.9$ for $t \sim 3$ Gyr onwards).

A careful comparison of Fig. 2.8 and Fig. 2.5 reveals a good correlation between the infall of material through filaments (large C_2) and the shape of the halos at a given time: high $l = 2$ moments are associated with virial contours that turn prolate (e.g. `Aq-A` for $t < 6$ Gyr, `Aq-C` for $t < 4$ Gyr, `Aq-D` for $t > 8$ Gyr). In particular, this multipole decomposition shows a filamentary accretion mode for halo `Aq-D` that is present at $t \geq 10$ Gyr, helping to explain why its axis ratio b/c remains close to unity at quite late times. When the accretion is more isotropic (i.e. $C_0/\Sigma_l C_l \simeq 0.9$), the halos become most nearly

[3]Note that we are not explicitly showing the $l = 0$ term in Fig. 2.8 because it is, by definition, set to unity in our formalism. However, the "relative" importance of the monopole with respect to the contribution of all other moments is a well defined quantity, that we analyze in more detail on the right panel of the same figure.

oblate. This explains why halo `Aq-E` is the more oblate in our sample, with $b/a \sim 0.9$ from $t \sim 3.5$ Gyr onwards, and also why it has this shape at smaller radii, compared for example to halo `Aq-C`.

We found that *the injection of material that occurs along filaments leads to a more prolate halo shape, an effect that is naturally enhanced at early times due to the relatively smaller size of the filaments with respect to the dark matter halo* (Avila-Reese et al., 2005; Gottlöber & Turchaninov, 2006). On the other hand, the more isotropic mass accretion that characterizes later phases of halo assembly for 10^{12}M$_\odot$ Milky Way-like objects, yields more oblate/triaxial geometries. When combined with the *memory* effect alluded to in Section 2.4.2, we find that prolate shapes are naturally expected to be set in the earliest collapsed regions (small radii) of $\sim 10^{12}$M$_\odot$ halos, in good agreement with previous work (Bailin & Steinmetz, 2005; Hayashi, Navarro & Springel, 2007). The filamentary structure typically found at early times thus seems to be responsible for the general trend of our Milky Way-like halos to be more prolate in their inner regions.

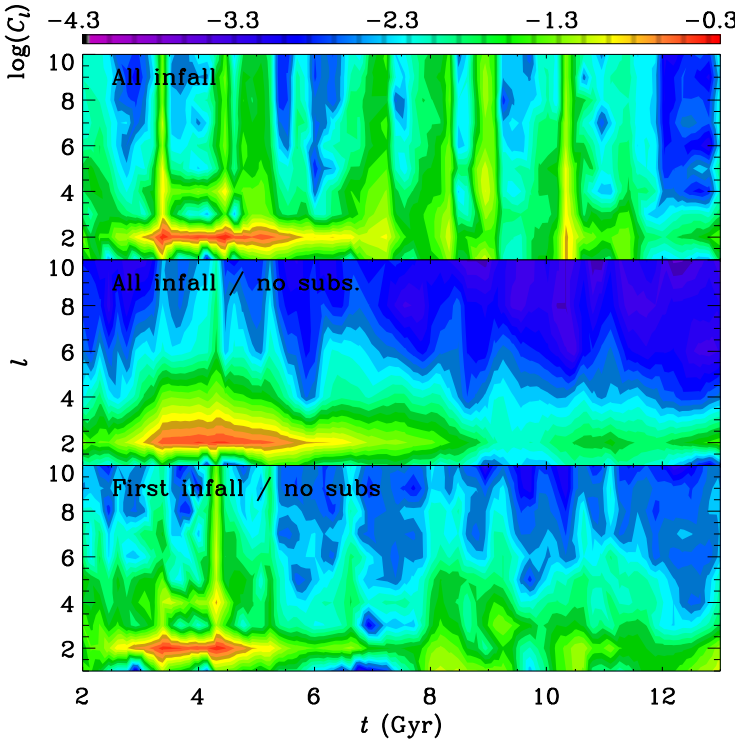

Figure 2.7: Multipole expansion of the infalling material ($v_r < 0$) in the region $1.0 \leq r/r_{\rm vir} \leq 1.2$ as a function of time for halo `Aq-A-4`. The upper and middle panels show the results with and without the contribution from subhalos, respectively. In the bottom panel only those particles that are on their *first infall* have been considered.

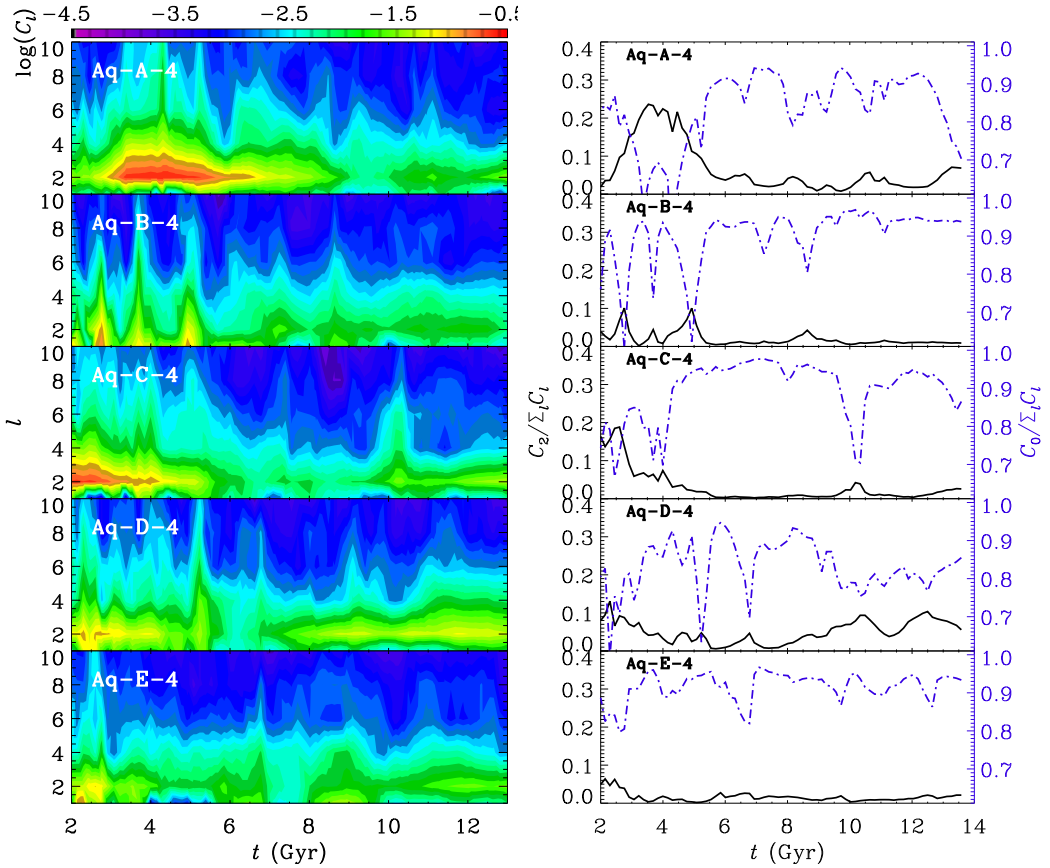

Figure 2.8: *Left:* Multipole expansion of the infalling material in the region $1.0 \leq r/r_{\rm vir} \leq 1.2$ as a function of time once the contribution from subhalos has been removed for the five Aquarius halos. *Right:* Relative contribution of the $l = 0$ (blue dot-dashed) and $l = 2$ (black solid) modes to the total power spectrum as a function of time for particles on their *first infall* onto each halo. While $C_2/\Sigma C_l$ provides information about the material infalling along a filament, large contributions from the monopolar term, $C_0/\Sigma C_l$, imply that the accretion is isotropic. Notice the good correlation between the time intervals with a clear signature of mass accretion through filaments (high power in $l = 2$ mode) and the more prolate shape in Fig. 2.5.

2.6 Conclusions

In this Chapter we analyzed the shape of five Milky Way-like dark matter halos selected from the Aquarius N-body simulations. We compared the performance of several methods proposed in the literature to measure the shapes of halos and found good agreement between all techniques, especially in the inner regions where substructures play only a minor role. Using an implementation of the normalized inertia tensor algorithm described in Allgood et al.

(2006), we have found excellent convergence between the several resolution levels of Aquarius, where the shapes can be robustly measured down to the convergence radius.

We find that mass assembly and environment are both responsible for setting the shapes of dark matter halos. The early evolutionary phases of $10^{12}M_{\odot}$ Milky Way-like halos are characterized by the accretion of matter through narrow filaments. In these circumstances the halos –as measured by their virial contours– are prolate and their minor axes tend to point perpendicular to the infall (filament) direction. Nonetheless, temporary tilting of the virial ellipsoids may occur when mass is accreted from a different direction. The latter is the case for just one of our halos located in a well defined filament at redshift $z = 0$.

On the other hand, at later times the cross-section of the filaments becomes larger than the typical size of Milky Way-like halos and as a result, accretion turns more isotropic and the objects evolve into a more oblate/triaxial configuration. This transition does not occur at the same time for all halos in the explored mass range but is strongly determined by their individual history of mass assembly and their surrounding environment.

The geometrical properties of halos at different epochs are not lost: halos retain memory of their structure at earlier times. This memory is imprinted in their present-day shape trends with radius, which change from typically prolate in the inner (earlier collapsed) regions to a triaxial in the outskirts (corresponding to the shells that have collapsed last and are now at the virial radius). These results are in excellent agreement with previous findings (Bailin & Steinmetz, 2005; Hayashi, Navarro & Springel, 2007).

A corollary of our results is that the strong link between halo properties and assembly history, which can show large variations from halo to halo, will make any *instantaneous* correlation between halos shape or orientation and mass or environment rather weak, explaining in part the relatively large scatter in such trends found in earlier studies (e.g. Bailin & Steinmetz, 2005; Bett et al., 2007).

It is important to stress that we have neglected the effects induced by the presence of baryons on the dark matter halo shapes (Kazantzidis et al., 2004; Bailin et al., 2005; Gustafsson, Fairbairn & Sommer-Larsen, 2006; Debattista et al., 2008; Pedrosa, Tissera & Scannapieco, 2009; Lau et al., 2011; Valluri et al., 2010). Therefore our results may only be directly applicable to dark matter dominated objects such as low surface brightness galaxies. However, the work of Tissera et al. (2010); Abadi et al. (2010); Bett et al. (2010) shows that even though the halo axis ratios increase when a disk is formed (i.e. they become rounder), the trends with radius appear to be preserved.

With the caveat of the neglected baryonic effects and the relatively low number of objects studied, our findings may be directly relevant to the modeling of stellar streams used to determine the gravitational potential of the

Milky Way. For example, the inconsistencies found between the constraints imposed by the positions and by the kinematics of stars in the Sagittarius stream could be indicative of a change in the shape of the Milky Way halo with radius (although see Law, Majewski & Johnston, 2009; Law & Majewski, 2010). Such a change could in principle be measured by using stellar streams which are on different orbits in the Galactic halo. Furthermore, it may even be possible to employ these to determine the growth history and early environment of the Milky Way. A validation of these ideas, however, is bound to a proper evaluation of the effect of the baryonic matter on our findings, as well as to the study of larger statistical samples, both issues that we plan to address in the near future.

Acknowledgments

LVS and AH gratefully acknowledge financial support from NWO and from the European Research Council under ERC-Starting Grant GALACTICA-240271. CSF acknowledges a Royal Society Wolfson Research Merit Award. This work was supported in part by an STFC rolling grant to the Institute for Computational Cosmology at Durham.

2.7 Appendix: The shape of dark matter halos: methods

In this section we provide a review of the various methods that have been proposed in the literature to measure dark matter halo shapes and compare the results when applied to the same object. The methods most commonly used are the diagonalization of the inertia tensor and the characterization with ellipsoids of either the interpolated density field or the underlying gravitational potential (Warnick, Knebe & Power, 2008). We introduce as well an additional scheme, which incorporates the advantages of different pre-existing methods, and where halo shapes are determined by fitting ellipsoids to the 3D iso-density surfaces.

2.7.1 Inertia tensor

One of the drawbacks of methods based on the determination of the inertia tensor is its quadratic relation with distance, which assigns the largest weight to particles residing far away from the center, an issue complicated further by the presence of substructures in the outskirts of the dark matter halos.

The bias introduced by this distance weighting can be alleviated by normalizing each coordinate with some measure of distance (Gerhard, 1983; Dubinski

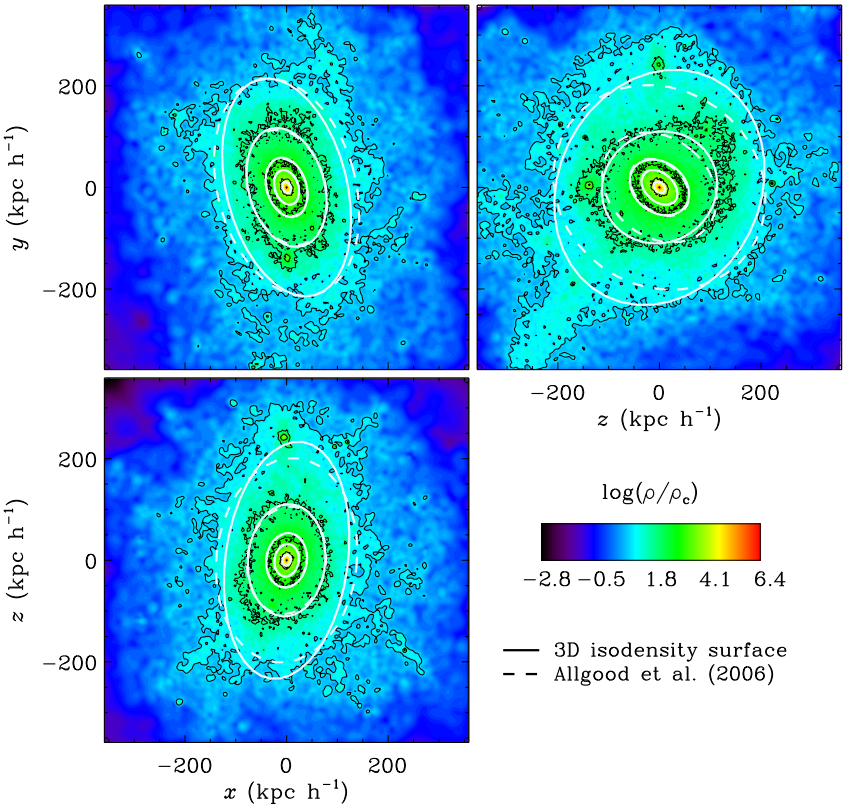

Figure 2.9: Dark matter density in thin slices centerd on the $z = 0$ (left) $y = 0$ (center) and $x = 0$ (right) planes. The black lines represent the isodensity contours. The solid white ellipses correspond to our new density-based method, while the dashed ones are for the inertia tensor method described by Allgood et al. (2006). In the inner regions both methods agree very well and follow the isodensity surface, however closer to the virial radius (the external most contour) the inertia tensor-based scheme predicts somewhat rounder shapes than the actual density distribution.

& Carlberg, 1991). In this case the "reduced" inertia tensor

$$I_{ij} = \sum_{\boldsymbol{x}_k \in V} \frac{x_k^{(i)} x_k^{(j)}}{d_k^2}, \tag{2.5}$$

where d_k is a distance measure to the k-th particle and V is a set of particles' positions. Assuming that dark matter halos can be represented by ellipsoids, the axis ratios are the ratios of the square-roots of the eigenvalues of $\boldsymbol{I}$, and the directions of the principal axes are given by the corresponding eigenvectors. To determine the axis lengths (e.g. b and c) however requires knowledge of the third axis (a). Therefore there are different choices to be made in this method, namely, which is the initial set of points V, the distance measure d and the

way in which a is defined. Different approaches have been followed to set these quantities.

- Warren et al. (1992) use an iterative scheme keeping the ellipsoid volume constant. The set V, initially chosen to be a spherical shell, is iteratively deformed and reoriented using the eigenvalues and eigenvectors of the reduced inertia tensor. These authors take d to be the Euclidean distance to a given particle. Bailin & Steinmetz (2005), however, argue that this systematically overpredicts the roundness of the halos. In the figures below we have modified Warren et al.'s method by using $d_k^2 = x_k^2 + y_k^2/q^2 + z_k^2/s^2$ instead, and where $q = b/a$ and $s = c/a$ are updated in each iteration. We define also the shell's radii using this definition of distance, instead of the Euclidean one.

- Allgood et al. (2006) also employ an iterative scheme but now keeping the largest axis length constant. Initially the set V is selected to be given by all particles located inside a sphere (as opposed to a spherical shell of a given radius) which is reshaped iteratively using the eigenvalues. As before, the orientation is determined from the eigenvectors of $\boldsymbol{I}$, and the distance measure used is $d_k^2 = x_k^2 + y_k^2/q^2 + z_k^2/s^2$. In the figures below we have removed all bound substructures contained in a halo. This alleviates the noise and artificial tilting of the ellipsoids that is introduced by such substructures. We use SUBFIND (Springel et al., 2001) to identify and remove particles associated to subhalos within the region of interest.

In our implementations the iterations are stopped when convergence in the axis ratios is reached, which we take to be when the relative change is smaller than 10^{-6}, or when V is composed by less than 3000 particles. If the latter condition is not fulfilled the shape of such a contour is not considered in our analysis.

2.7.2 Density

An alternative approach to determine halo shapes is to consider the underlying density field, which carries more information about the internal mass distribution of the halos than the inertia tensor. We explore here two different implementations.

- Jing & Suto (2002) determine the shape by fitting ellipsoids to sets of particles having (nearly) the same nearest neighbours-based density. Noise due to substructures is effectively removed by an implementation of the Friends of Friends (FOF) algorithm to these sets (Davis et al., 1985), and where the linking length is selected to vary from set to set of iso-density particles according to the empirical law $l = 3(\rho/m)^{-1/3}$.

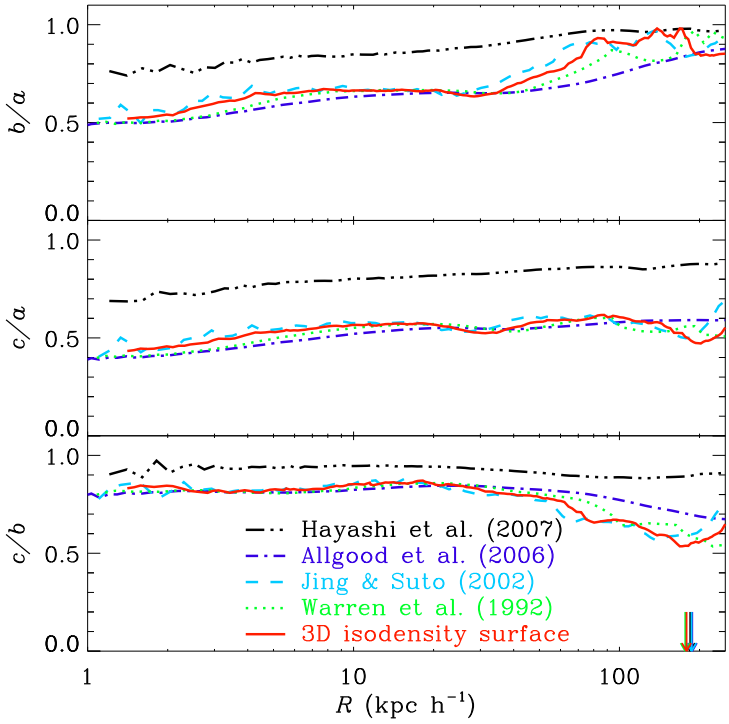

Figure 2.10: Axis ratios ($a \geq b \geq c$) for `Aq-A-4` as a function of the ellipsoidal distance $R = (abc)^{1/3}$. The solid red line corresponds to our new algorithm, while dot-dashed black, dashed cyan, dot-dashed blue and dotted green correspond respectively, to: iso-potential contours (Hayashi, Navarro & Springel, 2007), particle-based iso-density inertia tensor (Jing & Suto, 2002), normalized inertia tensor diagonalized upon hollow (Warren et al., 1992) and on solid (Allgood et al., 2006) ellipsoids. Vertical arrows indicate the size of the virial ellipsoid, $R_{\rm vir}$, for each method. All methods agree well, especially in the inner regions ($R \lesssim 100h^{-1}$ kpc).

- We present a new method based on fitting an ellipsoid to the particle density. We first create a continuous density field out of the particles positions. We do so by using a Cloud-In-Cell algorithm that allows the reconstruction of the density field on a regular grid (Hockney & Eastwood, 1988). For better resolution and to keep the computational cost relatively low, the region covered by the grid is iteratively increased. The second step involves the identification of iso-density contours. We select the cells with nearly the same density and a version of the FOF algorithm is used to get rid of cells associated to substructures artificially linked to

the main contour. Finally, we minimize the function:

$$\mathcal{S}(\boldsymbol{M}) = \frac{1}{n}\sum_{k=1}^{n}\left(1-\sqrt{\boldsymbol{x}_k^T\boldsymbol{M}\boldsymbol{x}_k}\right)^2, \tag{2.6}$$

with $\boldsymbol{M}$ the matrix representation of an ellipsoid, in order to determine the axis lengths (eigenvalues of $\boldsymbol{M}$) and directions (eigenvectors). Notice that the minimization is carried out in a 6 dimensional space ($\boldsymbol{M}$ has just 6 independent elements), therefore an educated initial guess for the iteration may reduce the numerical effort. We provide this guess by diagonalizing the inertia tensor of the cells with similar values of the density.

Fig. 2.9 shows 2D slices of the density map computed for halo `Aq-A-4`, together with several best-fit ellipsoids found by the method just outlined. An important feature of our method is that all the information about the 3D isodensity *surface* is taken into account; this is particularly useful towards the outskirts of the dark matter halos where, as can be appreciated from Fig. 2.9, density contours become less symmetric. For comparison, we also show the results of applying the algorithm by Allgood et al. (2006) (after subhalos subtraction) in dashed lines. Recall that in our new method ellipsoids are effectively independent of each other and therefore this method is more sensitive to local variations of the halo shapes. On the other hand, Allgood et al. (2006) use the whole set of particles within a given radius, which implies that the shape of a contour at a given distance is correlated with the shape at smaller radii, as a careful inspection of this figure shows.

2.7.3 Potential

A viable alternative to the density-based methods to measure the shape of a dark matter halo is to use the gravitational potential field defined by the particles. As first noticed by Springel, White & Hernquist (2004) and later confirmed by Hayashi, Navarro & Springel (2007), substructures cause significant fluctuations in the local density distribution, but their contribution to the gravitational potential is considerable less harmful (Springel, White & Hernquist, 2004; Hayashi, Navarro & Springel, 2007). Iso-potential contours are therefore smoother and more regular than those defined by the density field. Taking advantage of this feature, Hayashi, Navarro & Springel (2007) have implemented a method to characterize the structural shape of dark matter halos by fitting ellipses to the iso-potential contours computed on three orthogonal 2D planes. It is important to note here that the potential is intrinsically rounder than the density distribution, for example for a cored logarithmic potential $1-(c/a)_\rho \approx 3[1-(c/a)_\Phi]$ outside the core (Binney & Tremaine, 2008).

2.7.4 Results

In Fig. 2.10, we compare the shape as a function of the ellipsoidal radius obtained for the halo `Aq-A-4` using the methods described above. This figure shows very good agreement in the halo shapes measured by the different methods, especially in the inner regions ($R \lesssim 100h^{-1}$ kpc). There is however an indication that at large radii, density-based methods (red solid and light-blue dashed curves) tend to give slightly more oblate shapes (higher b/a) than those based on implementations of the inertia tensor, but the effect is only marginal. As expected, the method based on the gravitational potential (Hayashi, Navarro & Springel, 2007) produces higher axis ratios (blue dotted line).

2.8 Appendix: The size of filaments at different times

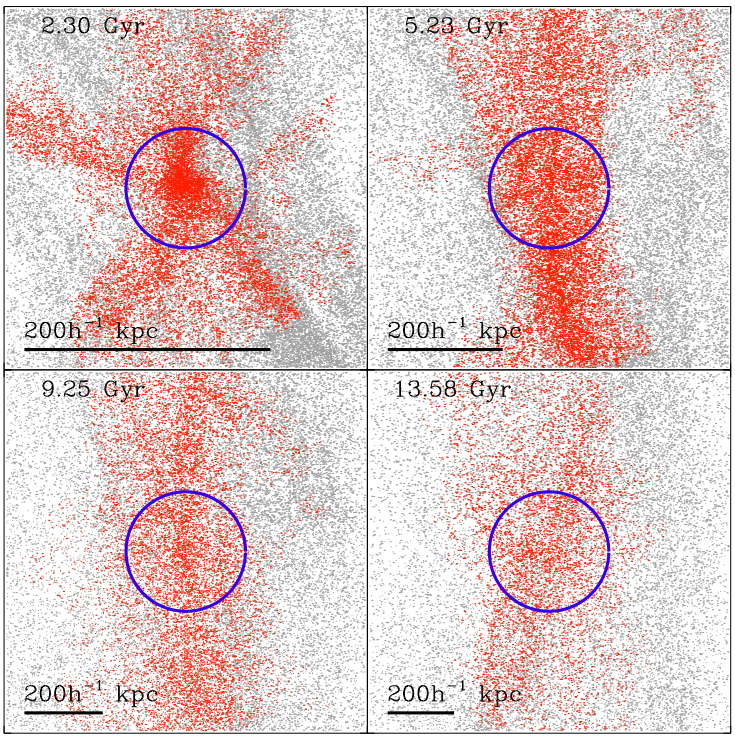

Figure 2.11: Distribution of particles around `Aq-A` halo at four different times. Particles with a single caustic crossing are plotted in red and are seen to trace reasonably well the filamentary structure surrounding the halo. Each box has been rotated according to the inertia tensor defined by this subset of particles.

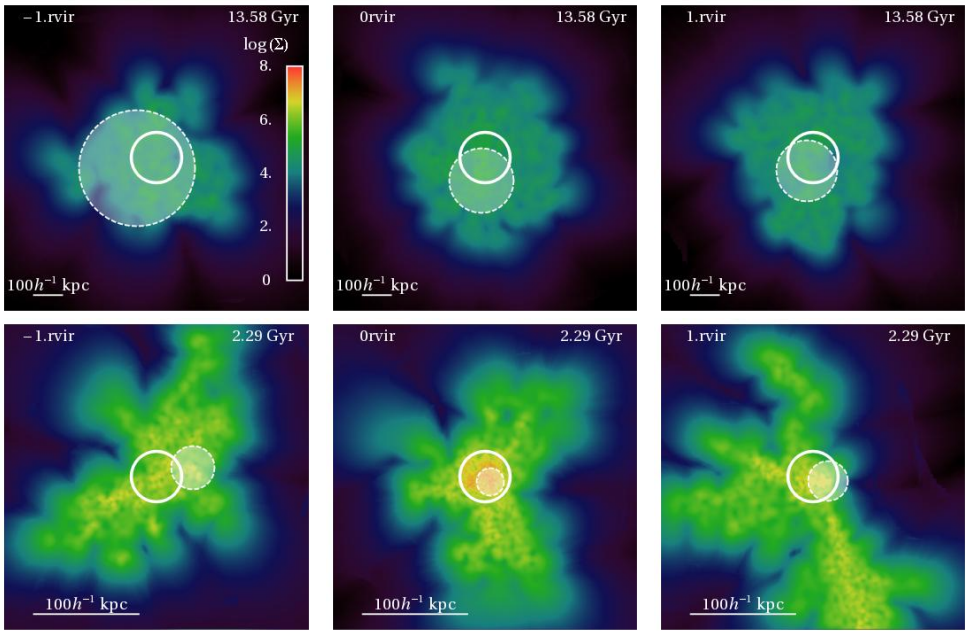

Figure 2.12: Projected mass density (in units of $h\mathrm{M}_{\odot}\mathrm{kpc}^{-2}$) for three different perpendicular planes located along the direction of the filament at positions $z_p = [-1, 0, 1]r_{\rm vir}$, and at two different times: $t = 13.6$ Gyr (top) and $t = 2.3$ Gyr (bottom). The solid white curve indicates the half the virial radius of the halo at each time and the highlighted filled disk shows the size assigned to the filament and centerd in the highest density point as described in the text. The geometry of the filaments is complicated, but their relative size with respect to that of the halo is clearly larger at present day ($t \sim 13.6$ Gyr) than it was at $t \sim 2.3$ Gyr.

Dark matter halos that reside in a filament will acquire their mass preferentially along the filament's longest axis. As discussed in Sec. 2.5, such infall of material gives rise to a power spectrum characterized by a significant $l = 2$ component. However, when the surrounding filament is sufficiently wide, i.e. of comparable or larger cross-section than the virial radius of the halo, the infalling particles will appear to be more isotropically distributed on the sky, shifting the power to the $l = 0$ term of the spectrum. We have argued in Section 2.5 of this Chapter that the latter case is characteristic of the late stages of mass assembly in $\sim 10^{12}\mathrm{M}_{\odot}$ objects. We analyze this statement in more detail in this Appendix, and provide a suitable measurement of a filament's size and compare it to that of the dark matter halo it hosts. For brevity we focus our analysis on halo `Aq-A`, but our conclusions should hold in the general case.

The measurement of the size of a filament is not completely straightforward and may depend on the particular algorithm used for its identification (Stoica et al., 2005; Zhang et al., 2009). In this work we define structures according to the number of caustic crossings of its constituent particles. Caustics arise during the gravitational collapse of a dynamical system. In the case of cold dark matter, the initial velocities of particles are negligible, and thus these are distributed in 3D sheets in phase-space (Bertschinger, 1985). Their collapse and subsequent virialization may be seen as the folding of these sheets, and the location of these folds in configuration space gives rise to caustics. Therefore the number of caustic crossings is indicative of the degree of virialization of a dynamical system.

For example particles with zero crossings remain under the quasi-linear regime and have therefore not collapsed into any virialized structure today. As gravitational collapse proceeds, the number of caustics that a particle experiences increases rapidly. As shown in Vogelsberger & White (2011, Fig. 4), particles with 1 or 2 caustic crossings delineate the surrounding filamentary structure of a halo, whereas those with a higher number of crossings belong to the host halo itself. Therefore, in this work we select particles with 1 caustic crossing to study the properties of the filamentary structure surrounding `Aq-A` halo at different epochs (Vogelsberger et al., 2009; Vogelsberger & White, 2011).

Fig. 2.11 shows the distribution of particles in a box of size $6r_{\mathrm{vir}}$ at four different times, where those with a single caustic crossing are highlighted in red. The circle indicates the corresponding virial radius of the `Aq-A` halo, and the horizontal bar gives the reference for conversion to the physical scale. At each time-step we have rotated the reference frame to the principal axis of the inertia tensor defined by the particles with 1 caustic crossing [4]. This figure

[4]Because we are interested in the set of filaments connected to the central object, we run a FOF algorithm over the particles with 1 caustic crossing, using a linking length of 0.7 the mean interparticle separation and retain for the analysis only those set of particles belonging

shows these particles successfully trace the filamentary structure around this halo. Interestingly, there is a hint of evolution in the relative size of the filament with respect to that of the halo: as we move back in time, the red particles change from fully encompassing the halo ($t \geq 9$ Gyr) to having a similar cross-section ($t \sim 5.25$ Gyr) to becoming even narrower at earlier times ($t \sim 2.3$ Gyr). At this point the geometry of the system is much more complex due to multiple filaments feeding material to the central object.

In order to quantify the evolution in the cross section of a filament we proceed as follows. We rotate the reference system such that the z-direction is that given by the inertia tensor of particles with 1 caustic crossing. We identify planes perpendicular to this direction and label the positions of such planes as z_p, where $z_p = [-2, -1.5, -1, ..., +1.5, +2]\ r_{\rm vir}$. We project in each plane all selected particles that satisfy $|z_i - z_p| \leq 0.5 r_{\rm vir}$. We compute the (projected) density of neighbours of each particle in the plane using a 2D SPH kernel and identify the particle with the highest density. This particle's location sets the centroid of the filament and its density at the core. We then define the radius of the filament $r_{\rm fil}$ as the distance from this centroid where the density has dropped to 60% of its central value. Although this definition is arbitrary, this allows a measurement of the relative size at different times.

Fig. 2.12 illustrates our procedure for two different times: $t = 13.6$ (top) and $t = 2.3$ (bottom) Gyr; applied to 3 different planes along the z-direction: $z_p = -r_{\rm vir}, 0, +r_{\rm vir}$. Each panel shows the projected density of particles belonging to the filamentary structure (one single caustic crossing), where the virial radius of the central halo is indicated with a white (empty) circle, and the highlighted full disk indicates the size of the filament centerd on the highest density point as described above. Fig. 2.12 suggests that filaments are not really straight in space (as indicated by the different positions of the centroids for panels located at different z_p) and also their geometry is complex since panels located symmetrically with respect to the center of the halo yield significantly different sizes (e.g. top row, $-r_{\rm vir}$, $+r_{\rm vir}$ panels). However, there is still a clear trend indicating that the filament's relative size was smaller at early times than at the present day.

This trend is more clearly seen in Fig. 2.13, where we show the average size of the filament (normalized to a fraction of the instantaneous virial radius) measured as the average over 9 equally distant planes located from $[-2r_{\rm vir}, +2r_{\rm vir}]$ as a function of time. The shaded region shows the scatter between the sizes derived for each of the individual planes at a fixed time. Notice that the relative filament-to-halo size at present day is almost twice as large than its value at $t \sim 2$ Gyr. This provides further support to our observation that the infall of particles at later times results from an increased size of the filament with respect to that of the halo.

---

to the most massive FOF group

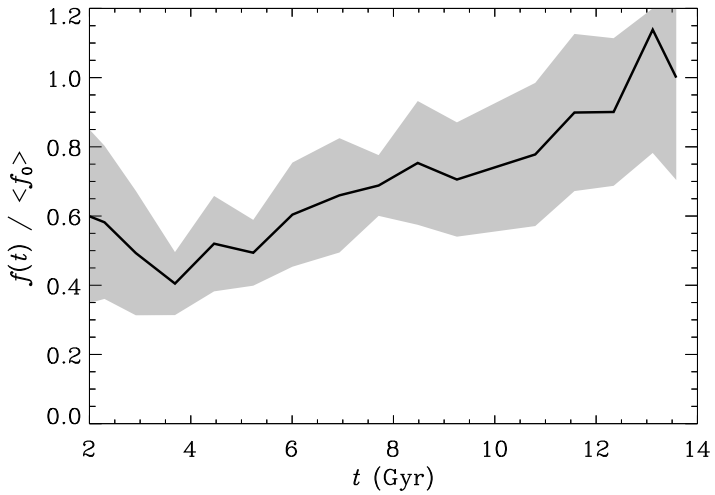

Figure 2.13: Filament size relative to the virial radius $f = r_{\rm fil}/(0.5r_{\rm vir})$ as a function of time. The solid black line is the average size of the filament measured on 9 planes perpendicular to the direction of the filament. The shaded region is 1σ scatter (see text for details) . The vertical axis has been normalized to its final value at redshift zero $f_0 = f(z = 0)$ for an easier comparison.

CHAPTER 3

The shape of dark matter sub-halos in the Aquarius simulations

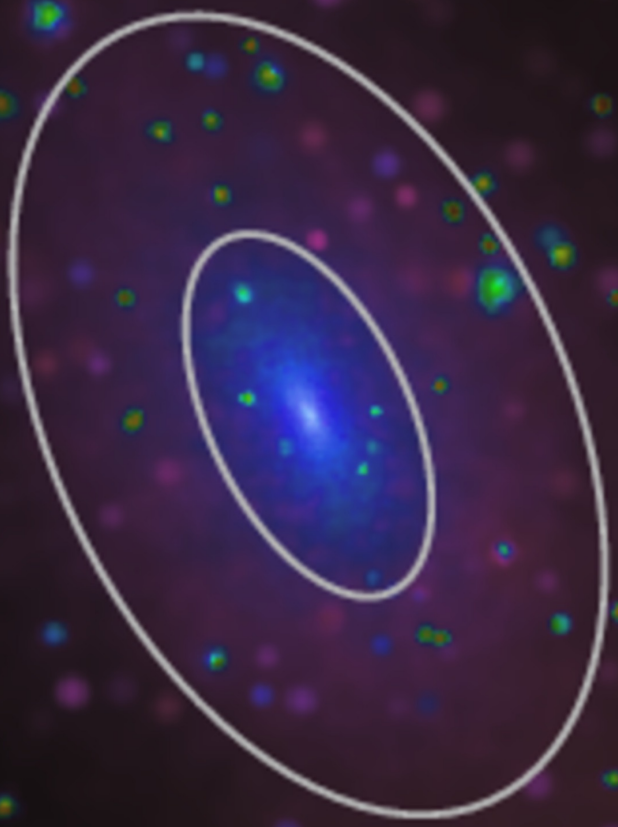

Carlos A. Vera-Ciro et al.

in preparation

Abstract

We analyze the Aquarius simulations to characterize the shape of dark matter halos with peak circular velocity in the range $8 < V_{\rm max} < 200$ km/s, and perform a convergence study using the various Aquarius resolution levels. For the converged objects, we determine the principal axis ($a \geq b \geq c$) of the normalized inertia tensor as a function of radius. In general we find that field halos are more triaxial with increasing halo mass, with our smallest halos being rounder by $\sim 40 - 50\%$ than Milky Way-like objects at the radius of peak circular velocity, $r_{\rm max}$. We find that the distribution of axis ratios for the subhalo population is consistent with that of field halos of comparable $V_{\rm max}$ within the scatter. Inner and outer contours within each object are well aligned, with the major axis preferentially pointing in the radial direction for subhalos close to the host, although with a large scatter. We specifically analyze the dynamical structure of subhalos likely to host luminous satellites comparable to the classical dwarf spheroidals in the Local Group. These halos have axis ratios that increase with radius, and which are mildly triaxial with $\langle b/a \rangle \sim 0.75$ and $\langle c/a \rangle \sim 0.60$ at $r \sim 1$ kpc. Their anisotropy profiles $\beta(r)$ become strongly tangentially biased in the outskirts as a consequence of tidal stripping.

Cover: $v_{\rm max}$ and tidal contour for a Sculptor-like subhalo of Aq-A-2 ($v_{\rm max} = 39$ km s^{-1}, $M_V = -11.1$)

3.1 Introduction

In the Λ cold dark matter cosmological paradigm structures build hierarchically, from the mergers of smaller objects (Press & Schechter, 1974; Gott & Rees, 1975; White & Rees, 1978; Blumenthal et al., 1984). As the merging proceeds, they exert tides on each other and at the present time, may be fully assembled into a single object or survive as composite system consisting of bound substructures (or subhalos) orbiting a larger host. Early N-body experiments of structure formation showed how this process took place with halos hosting a few dozen substructures down to the numerical resolution limit typical at that time (Tormen, 1997; Tormen, Diaferio & Syer, 1998; Ghigna et al., 1998; Klypin et al., 1999a,b; Moore et al., 1999). For systems like the Milky Way, current numerical simulations have extended the dynamical range of resolved substructures by 4-5 orders of magnitude (Diemand, Kuhlen & Madau, 2007; Diemand et al., 2008; Springel et al., 2008; Stadel et al., 2009).

The properties of these substructures are of great interest since luminous satellites such as the population of dwarf spheroidal (dSph) galaxies in the Local Group, are expected to be embedded in (some of) them (Stoehr et al., 2002; Strigari, Kaplinghat & Bullock, 2007; Boylan-Kolchin, Bullock & Kaplinghat, 2012a; Vera-Ciro et al., 2012). Furthermore, the large mass to light ratios of dSph, which range in the 10s to 1000s (Mateo, 1998; Gilmore et al., 2007; Walker, 2012), indicate that their internal dynamics are dominated by the dark matter. This suggests that the predictions of pure dark matter simulations may be more directly confronted with observations of these systems. For instance, it has been suggested that they provide an optimal place to look for signals of dark matter self-annihilation processes (Kamionkowski, Koushiappas & Kuhlen, 2010), due to the natural enhancement in density and the lack of significant contamination from the baryonic component.

The availability of large samples of line of sight kinematics for individual stars in dSph galaxies has also opened new possibilities to test the predictions of ΛCDM on the structural properties of dark matter subhalos. For instance, studies of N-body numerical simulations have shown that the inner slope of the dark matter density profile is expected to be cuspy in CDM models (Navarro, Frenk & White, 1996, 1997). This seems to contrast with the somewhat shallower slopes and even constant density cores supported by observations in local dwarf spheroidals (Amorisco & Evans, 2011; Walker & Peñarrubia, 2011; Amorisco & Evans, 2012; Jardel & Gebhardt, 2012). This however, is a subject of active debate, since various authors have shown that the stellar kinematics of Milky Way dwarfs are also consistent with the NFW cuspy profiles (Battaglia et al., 2008; Walker et al., 2009; Strigari, Frenk & White, 2010; Breddels et al., 2012a).

Most of the dynamical modeling performed in the studies of Local Group dwarf spheroidals rely on simple assumptions about the structure of their dark

matter component. In particular, spherical symmetry and specific anisotropy profiles have been extensively assumed. The orbital anisotropy has been taken to be constant (Richstone & Tremaine, 1986; Łokas, 2002; Łokas, Mamon & Prada, 2005; Łokas, 2009; Walker et al., 2009), or radially dependent (Kleyna et al., 2001; Wilkinson et al., 2002; Battaglia et al., 2008; Strigari et al., 2008; Wolf et al., 2010; Amorisco & Evans, 2011), while in Schwarzschild modeling or in made-to-measure N-body methods it does not need to be assumed (Long & Mao, 2010; Jardel & Gebhardt, 2012; Breddels et al., 2012a). The selection of geometric shape for the dark matter potential can also be relaxed. For example, Hayashi & Chiba (2012) considered axisymmetric dark matter halos to model some of the Milky Way dSph galaxies.

For isolated galaxies, numerical experiments of ΛCDM have clear predictions for these quantities. The shapes of (isolated) dark matter halos in the mass range $10^{10} - 10^{15}$ $M_{\odot}$, are generally found to be triaxial, with axis ratios depending on the mass of the object (Muñoz-Cuartas et al., 2011; Schneider, Frenk & Cole, 2012). In terms of their internal kinematics, the velocity ellipsoid is close to isotropic near the center of halos and becomes mildly radial towards the outskirts (Wojtak et al., 2005; Hansen & Moore, 2006; Ludlow et al., 2011).

For subhalos, however, less is known because of the demanding numerical resolution needed to model properly low mass halos orbiting within hosts of Milky Way mass. This situation has recently improved with simulations that are now able to successfully sample the mass function on these scales, such as the Via Lactea, CLUES, GHALO and Aquarius simulations (Diemand, Kuhlen & Madau, 2007; Diemand et al., 2008; Springel et al., 2008; Stadel et al., 2009; Libeskind et al., 2010). For instance, using the Via Lactea simulations Kuhlen, Diemand & Madau (2007) found that subhalos are also not spherical, although the effect of tides tend to make subhalos rounder than comparable objects in the field. These results prompt questions about the validity of some of the assumptions involved in the mass modeling of stellar kinematics in dwarfs. And although the orbital anisotropy of the stars in a dSph is likely unrelated to that of dark matter (and associated to the formation history), it might nonetheless be valuable to explore the dynamical structure of subhalos, although the results' direct applicability is limited.

A detailed study of the shape of the Milky Way mass Aquarius halos was presented in Vera-Ciro et al. (2011). Here we extend their analysis to lower mass objects, both subhalos of the main central halo and field halos, up to $1.5h^{-1}$Mpc from the center of the high resolution box. The Chapter is organized as follows. In Section 3.2 we describe the numerical simulations, introduce the methods we use to determine halo shapes and explore the convergence of the results. In Section 3.3 we compare the properties of subhalos and isolated objects of similar mass. We analyze subhalo shapes in the context of the kinematic modeling of dwarfs around the Milky Way in Section 3.4 and

summarize our main results in Section 3.5.

3.2 Shape measurements and convergence

We use the suite of cosmological $N-$body simulations from the Aquarius project (Springel et al., 2008). These consist of six $\sim 10^{12}$ $M_\odot$ dark matter halos (`Aq-A` to `Aq-F`), re-simulated with 5 different levels of resolution within the ΛCDM cosmology. The simulations use the zoom-in technique, with a high-resolution region that extends up to $\sim 2\ h^{-1}$Mpc from the center of each main halo. This exceeds the typical virial radius of the Aquarius halos by 5–10 times and allows to identify structures within the high-resolution region that have been unaffected by tidal forces from these main halos (see Springel et al., 2008, for further details).

In most of the analysis that follows we focus on the level-2 resolution runs, with a mass per particle $m_p \approx 10^4$ $M_\odot$. However, we use the other Aquarius levels to test the convergence of our results. Halos and subhalos are identified using the SUBFIND algorithm (Springel et al., 2001). We keep all structures identified with at least 20 particles.

To measure the shape of halos in the simulations we follow the same approach as Vera-Ciro et al. (2011) and iteratively compute the inertia tensor in ellipsoidal regions. At a given radius, the algorithm begins with a spherical contour which is reshaped and reoriented according to the principal axis of the normalized inertia tensor for the encompassed material, until convergence is reached (Allgood et al., 2006). More specifically, we define the normalized inertia tensor as

$$I_{ij} = \sum_{\boldsymbol{x}_k \in V} \frac{x_k^{(i)} x_k^{(j)}}{d_k^2}, \tag{3.1}$$

where d_k is a distance measure to the k-th particle and V is the set of particles of interest. Representing dark matter halos as ellipsoids of axis lengths $a \geq b \geq c$, the axis ratios $q = b/a$ and $s = c/a$ are the ratios of the square-roots of the eigenvalues of $\boldsymbol{I}$, and the directions of the principal axes are given by the corresponding eigenvectors. Initially the set V is given by all particles located inside a sphere which is re-shaped iteratively using the eigenvalues of $\boldsymbol{I}$. The distance measure used is $d_k^2 = x_k^2 + y_k^2/q^2 + z_k^2/s^2$, where q and s are updated in each iteration. In practice we find that the algorithm converges (i.e. the error in the shape between successive iterations is $< 1\%$) only when there are at least 200 particles in set V.

In Vera-Ciro et al. (2011) we showed that shapes can be robustly measured from the *convergence radius*, $r_{\rm conv}$ outwards (Power et al., 2003; Navarro et al., 2010), where:

$$\kappa(r) = \frac{N}{8 \ln N} \frac{r/V_c}{r_{200}/V_{200}} = \frac{\sqrt{200}}{8} \frac{N(r)}{\ln N(r)} \left[\frac{\overline{\rho}(r)}{\rho_c}\right]^{-1/2}, \tag{3.2}$$

and $N(r)$ is the number of particles inside the radius r, $\overline{\rho}$ is the spherically averaged density and ρ_c the critical density. This $r_{\rm conv}$ is defined such that the ratio between the local relaxation time and the dynamical time at the virial radius equals $\kappa = 7$. The value $\kappa = 7$ guarantees that the circular velocity profiles on the main halos deviate less than 2.5% between different resolutions (Navarro et al., 2010), and also shapes and orientations (Vera-Ciro et al., 2011). Notice that for subhalos we use the virial radius and virial velocity at the time of infall, although the critical density still corresponds to $z = 0$. As ρ_c increases with redshift, using its present day value provides a conservative estimate of the convergence radius.

Fig. 3.1 shows that the same criteria applied to our sample of subhalos also ensures convergence of the halo shapes for the low mass objects. We compare the results for the `Aq-A` run in all resolution levels 1-5 (red to black, respectively). The left panels show, as a function of halo maximum circular velocity $V_{\rm max}$, the mean axis ratios computed at the tidal radius $r_{\rm tidal}$, here defined as the ellipsoidal contour enclosing the 95% most bound particles. The thin lines correspond to the entire sample of subhalos, whereas the thick curve shows only converged objects (those where $r_{\rm tidal} \geq r_{\rm conv}$). At level 2, the one used for most of our analysis, the mean axis ratios agree with the highest resolution run `Aq-A-1` to better than 5% across the full spectrum of "converged" subhalos.

A similar conclusion is reached for the inner regions of subhalos, as shown by the right panels of Fig. 3.1. Here, c/a and b/a are computed at the radius of the peak circular velocity $V_{\rm max}$, which is typically ~ 9 times smaller than $r_{\rm vir}$ for field halos and ~ 6 times smaller than $r_{\rm tidal}$ for subhalos. The number of objects for which $r_{\rm conv} > r_{\rm max}$ is roughly ten times lower than those with $r_{\rm conv} > r_{\rm tidal}$. This explains the relatively more noisy behavior of the curves on the right column compared to those on the left (especially for the lowest two resolution runs, where typically less than 10 objects satisfy the convergence condition). In general, a subhalo whose shape has converged at the tidal radius has not necessarily converged at the $r_{\rm max}$ radius.

Besides the mean trends shown in Fig. 3.1, we also explored the convergence of halo shapes on an object-by-object basis. In order to do this, we identify the same subhalos in several resolution levels of the `Aq-A` halo by matching the Lagrangian positions of all the particles assigned to a substructure by SUBFIND back in the initial conditions (see Section 4.2 Springel et al., 2008, for further details) In addition to this criterion, we impose a maximum deviation on the orbital path of matched objects in different level runs. This is to ensure that the evolution of each subhalo has been comparable in the different resolution runs also in the non-linear regime. More specifically, we define

$$\Delta^2_{\boldsymbol{r}} = \frac{1}{N} \sum_{\rm snapshot} \frac{|\boldsymbol{r}_3(t) - \boldsymbol{r}_2(t)|^2}{|\boldsymbol{r}_2(t)|^2}, \tag{3.3}$$

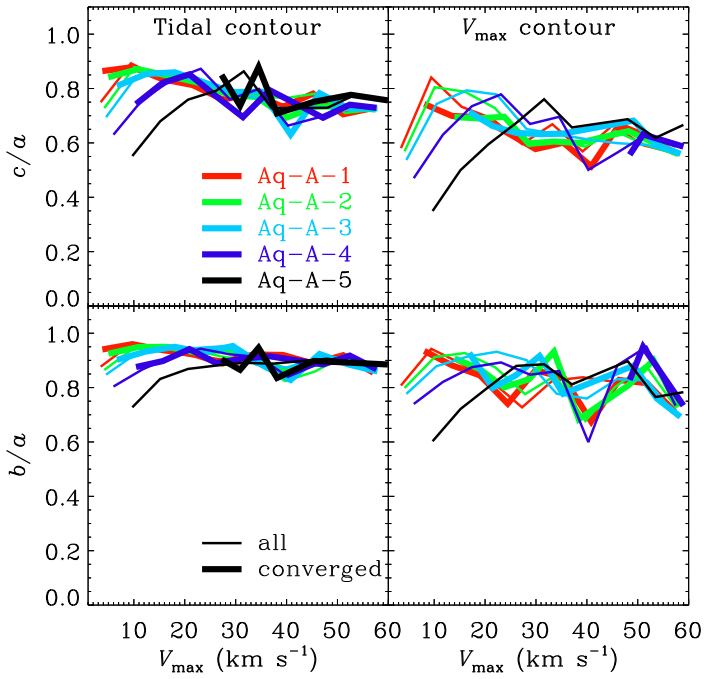

Figure 3.1: Shape of the tidal contour (left) and $V_{\rm max}$ contour (right) as a function of $V_{\rm max}$ for subhalos of the main halo at 5 different resolutions. With thick lines we plot subhalos for which $r_{\rm conv} \leq r_{\rm tidal}$ (left) and $r_{\rm conv} \leq r_{\rm max}$ (right), where $r_{\rm conv}$ is such that $\kappa(r_{\rm conv}) = 7$.

with $\boldsymbol{r}_j$ is the position[1] of the subhalo with respect to the main halo center at the j-th resolution level. This is computed for every snapshot from the time the object is first identified in the simulation box until present day. We consider only structures for which $\Delta_{\boldsymbol{r}} \leq 0.1$.

A total of 260 substructures are successfully matched in all levels 1,2 and 3 of the `Aq-A` halo by this procedure. For each object, we define $\delta_s = s_3/s_1 - 1$, where $s = c/a$ measured at $r_{\rm max}$ and the lower index indicate the resolution level (1 and 3 for our case). By construction, $\delta_s \sim 0$ for well converged objects. We show the distribution of δ_s in Fig. 3.2. The light gray histogram corresponds to all matched objects, and this is significantly broader than the distribution for the converged sample (i.e. cases where $r_{\rm max} > r_{\rm conv}$) shown in dark gray.

We illustrate this more clearly on the right panels in Fig. 3.2, which show the behavior of c/a as a function of distance $R = (abc)^{1/3}$ for three subhalos in the sample. Small colored dots indicate their δ_s value on the histogram on the left. The various curves correspond to the results for different resolution

[1]The positions of all halos and subhalos are defined by the particle with the minimum potential energy.

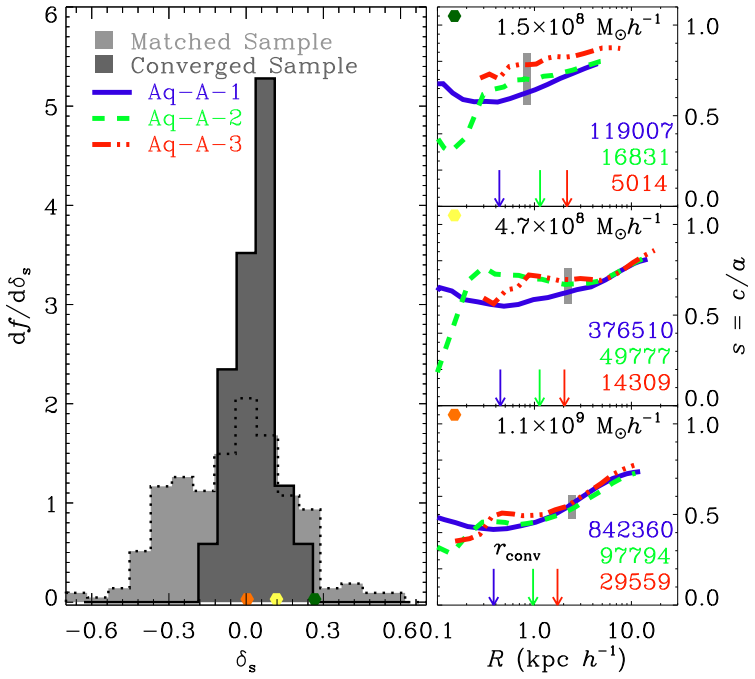

Figure 3.2: Left: Distribution function of the deviation of the major to minor axis ratio with respect to the highest resolution simulation δ_s. The light-gray histogram shows the distribution for the matched sample, while the dark-gray shows the results for the sample that satisfies that $r_{\rm conv}$ (vertical arrows in the right panels) is smaller than $r_{\rm max}$ (vertical gray line in the right panels) in all resolutions. The converged sample is narrower by a factor of 5. Right: Axis ratios as function of position for three different subhalos with the quoted number of particles in the respective resolutions.

levels as indicated by the labels. For each subhalo the convergence radius $r_{\rm conv}$ is marked with a vertical arrow and the position of the $V_{\rm max}$ contour by a vertical thick gray line. The top panel shows a typical example of an unconverged object: the peak of the circular velocity occurs at a smaller radius than $r_{\rm conv}$ for levels 2 and 3. On the other hand, subhalos in the middle and bottom panels have $r_{\rm max} > r_{\rm conv}$ and have therefore converged (according to our criterion) at all these levels.

Notice that a large number of particles does not guarantee convergence. For instance, the unconverged object on the top right panel of Fig. 3.2 has ~ 5000 and ~ 17000 particles in levels 3 and 2, respectively. These are significantly larger than the values previously used in the literature (e.g., Kuhlen, Diemand & Madau, 2007; Knebe et al., 2008a,b), and highlights the need to impose a second criterion to measure individual shapes reliably. With our criterion, for only $\sim 2\%$ of the halos with $5000-10000$ particles have the shapes at the $V_{\rm max}$ contour converged (i.e. $r_{\rm conv} > r_{\rm max}$). The situation improves significantly for

the tidal contour, where 99.6% of such objects have converged.

The distribution of axis ratios for converged objects shown in the left panel of Fig. 3.2 has a standard deviation $\sigma = 0.08$, meaning that 68.3% of the objects shapes determined at the Aquarius level-3 deviate less than 8% from their value in the highest resolution run. Since we focus on the level-2 runs for the analysis that follows, we expect resolution effects in our sample to be negligible.

The above discussion evidences that our criterion for convergence is relatively strict. There are 21403 subhalos with at least 200 particles within the tidal radius in all the Aquarius simulations, and we find that the inertia tensor algorithm converges for 11483 subhalos at the $r_{\rm max}$ contour, and for 13970 at the tidal contour. If we now impose our convergence criteria, there remain 412 and 6072 subhalos with well-determined shapes at the $r_{\rm max}$ and tidal contours respectively. For halos in the field our convergence criteria leads to a reduction of 96% and 35% for the $r_{\rm max}$ and tidal contours respectively. As expected, there is a larger proportion of field objects whose shapes can be measured at the tidal contour. However, despite this significant reduction in sample size, we have gained in the reliability of the shape determination for *individual* halos.

Therefore, in the next section we focus on those halos which satisfy our convergence criteria.

3.3 Halo shapes as a function of mass and environment

We proceed to characterize the variations in the axis ratios b/a and c/a of dark matter halos according to their mass, or equivalently their maximum circular velocity. The left column of Fig. 3.3 shows b/a and c/a for isolated objects measured at the tidal radius (labeled *tidal contour*) and at $r_{\rm max}$ ($V_{\rm max}$ *contour*) in the top and bottom panels, respectively. A thick line indicates the median trend of our sample and the open symbols at the high mass end show the results for the main Aquarius halos from Vera-Ciro et al. (2011). In agreement with previous work, we find that axis ratios tend to decrease gently with $V_{\rm max}$ (Allgood et al., 2006; Macciò et al., 2007; Hahn et al., 2007b; Bett et al., 2007; Muñoz-Cuartas et al., 2011), although we now explore a different mass regime.

Inspection of the top and bottom panels shows that the dependence of the axis ratios with circular velocity is somewhat steeper when measured at $r_{\rm max}$ than at the tidal contours. Typically, our lowest mass objects have inner axes that are rounder by $40-50\%$ than those of Milky Way-like halos. Nevertheless, the scatter from object to object at fixed circular velocity also is larger at $r_{\rm max}$, as indicated by the shaded regions. This is partially driven by the smaller number of converged objects in the $V_{\rm max}$ contour sample (735) compared to the tidal contour (3046).

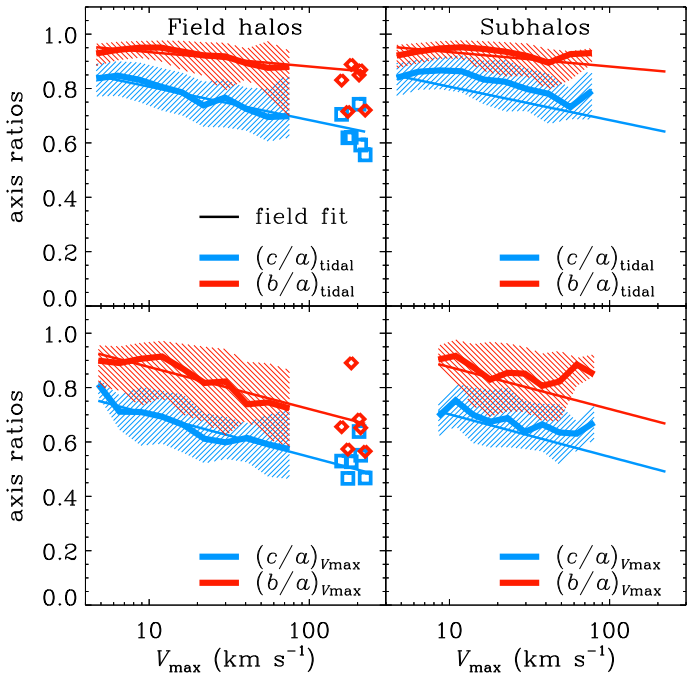

Figure 3.3: Shape as a function of $V_{\rm max}$ for field halos (left) and subhalos of the main halos in the suite of Aquarius simulations (right). Thick lines represent the median of the distribution of converged structures and the shadowed region represents $\pm 1\sigma$ equivalent dispersion around the median. Thin lines are fits to the objects in the field. The diamonds and squares indicate the axis ratios of the main Aquarius halos.

A comparison between the left and the right column of Fig. 3.3 reveals that there are only small differences between subhalos and isolated objects. To ease this comparison we overplot in the panels on the right the linear fits obtained for field halos. This shows that, on average, subhalos are slightly more spherical than field halos at a given $V_{\rm max}$, but differences are well within the scatter in the samples. The number of converged objects in the case of subhalos is 385 and 1522 for $V_{\rm max}$ and tidal contours, respectively.

Could the differences between field halos and subhalos be caused by measuring shapes at different physical radii? It has been shown in the literature that tidal evolution can significantly decrease $r_{\rm max}$ in satellites while affecting $V_{\rm max}$ significantly less (Hayashi et al., 2003; Kravtsov, Gnedin & Klypin, 2004). In that case, the measurement of the halo shape at $r_{\rm max}$ would be at a smaller radius for a subhalo than for a halo in the field with the same $V_{\rm max}$, and the same holds for the tidal contour. We address this in Fig. 3.4, where we show the minor-to-major axis profiles for individual field halos (left) and subhalos (right) of similar mass ($V_{\rm max} \sim 50$ km s^{-1}). The solid dots indicate that the location of the peak circular velocity are comparable in both samples

and therefore shows that this can not be reason for the different trends reported in Fig. 3.3. We thus confirm that, on average, subhalos of a given $V_{\rm max}$ are slightly more spherical than comparable field halos at all radii, particularly in the outskirts. Kolmogorov-Smirnov tests indicate that the difference between both samples is statistically significant only at the tidal contours (the KS probability is 0.09 in that case vs 0.42 at $r_{\rm max}$). However, the differences are well within the object-to-object scatter (see the bottom panel Fig. 3.4).

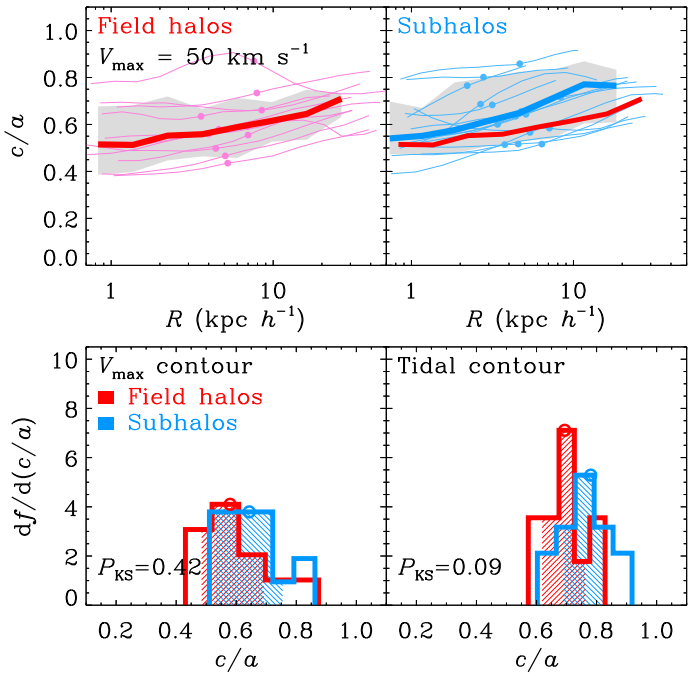

Figure 3.4: Top: The thin lines show the minor-to-major axis ratios profiles as a function of radius for objects with $V_{\rm max} \sim 50$ km s^{-1}. The thick lines correspond to the median and the shadowed region is 1σ equivalent scatter for objects in the field (left) and subhalos (right). The median for field halos is also plotted in the right panel for comparison. Bottom: Distribution of the axis ratios of the $V_{\rm max}$ (left) and tidal (right) contour for the field halos (red) and subhalos (blue) plotted in the top panels. Although the median axis ratio (open circle) is slightly larger for subhalos the differences are well within the scatter.

The similarity between the subhalo and field populations apparent in Fig. 3.3 and Fig. 3.4 explains the lack of appreciable trends as a function of distance d to the center of the main Aquarius halos, shown in Fig. 3.5. The typical axis ratios measured at the tidal as well as $V_{\rm max}$ contours do not depend on the distance to the host center up to distances $d \sim 5r_{\rm vir}$. However, the bottom panel of Fig. 3.5 shows that the tidal field of the host imprints a significant radial alignment on the subhalos, which tend to orient their major axis radially to the

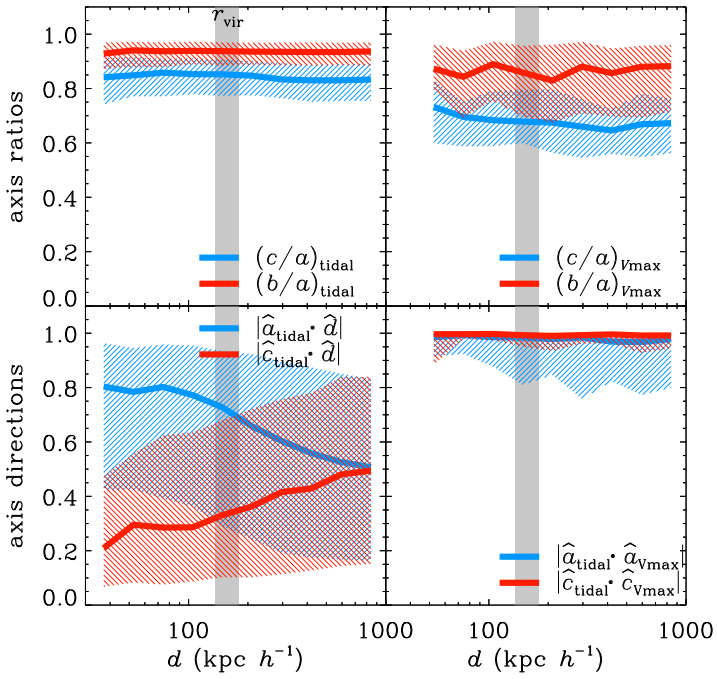

Figure 3.5: Shape and orientations of subhalos and objects in the field as a function of distance to the main halos d in each of the Aquarius simulations. The gray line indicates the positions of the virial radius of the main halos.

center of the host, albeit with a large scatter. The signal is stronger close to the center of the main host halos and decreases steadily until it disappears at $d \gtrsim 2r_{\rm vir}$, where the distribution is consistent with random. Interestingly, inner (at $r_{\rm max}$) and tidal contours are well aligned within each object, as shown in the bottom right panel; meaning that subhalos that venture close to the host appear to respond nearly as solid bodies. These results are consistent with similar analysis presented in Faltenbacher et al. (2007); Knebe et al. (2008a); Pereira, Bryan & Gill (2008); Kuhlen, Diemand & Madau (2007).

3.4 Application to the Modeling of Local Group Satellites

As discussed in the Introduction, the Local Group satellite galaxies are expected to inhabit dark matter subhalos comparable to those studied in the previous section. Since the contribution of the baryons to the gravitational potential of these systems is thought to be sub-dominant, the shape, dynamics and orbital structure of their host dark halos may be compared in a reasonably direct way to those of a suitable subset of the subhalos in the Aquarius

Parameter	Median	-1σ	$+1\sigma$
α	0.27	0.07	0.10
r_{-2} (kpc)	1.21	0.42	0.58
v_{-2} (km s^{-1})	9.06	1.87	1.72
c_Φ/a_Φ	0.70	0.07	0.10
b_Φ/a_Φ	0.83	0.10	0.09
r_a (kpc)	1.72	1.26	2.86
χ	1.60	0.13	0.09
$\ln A$	-2.42	0.15	0.20

Table 3.1: Best fit values for the profiles shown in Figs. 3.6 and 3.7. See text for details.

simulations.

To select subhalos likely to host luminous satellites comparable to local dwarfs we use the semi-analytical model of Starkenburg et al. (2012). The semi-analytic model includes physical prescriptions for the treatment of relevant processes such as radiative cooling, chemical enrichment, star formation, supernova feedback, etc. The parameters in the model are tuned to simultaneously reproduce the luminosity function and spatial clustering of bright galaxies as well as the properties of satellites in the Local Group (De Lucia & Blaizot, 2007; De Lucia & Helmi, 2008; Li, De Lucia & Helmi, 2010).

3.4.1 The subhalo shapes of luminous satellites

Fig. 3.6 shows the axis ratios as a function of distance along the major-axis r for our sample of subhalos. This consists of subhalos within the virial radius of their hosts at $z = 0$ and that resemble the *classical satellites* of the Milky Way in their luminosity, i.e., their V-band absolute magnitudes are in the range $-13.2 \leq M_V \leq -8.6$. Each curve is plotted from the convergence radius out to the tidal contour, and the blue color scale indicates the luminosity assigned by the semi-analytic model to the satellites.

Figure 3.6 shows that the dwarf galaxies in the model are surrounded by subhalos that are triaxial, with axis ratios b/a and c/a typically increasing from the inner regions to the tidal radius. The scatter from object to object is large, but the overall trend with radius is similar for all subhalos. The median profile, and 1σ-equivalent percentiles of the sample are given, respectively, by the black solid line and the gray shaded area. These dark matter subhalos have on average $c/a \sim 0.60$ and $b/a \sim 0.75$ at a radius of ~ 1 kpc, and turn more spherical close to the tidal radius, where $c/a \sim 0.8$ and $b/a \sim 0.9$.

The median dependence of the axis ratios with distance has a similar functional form to that modeled by Vogelsberger et al. (2008) for the main Aquarius

halos. These authors propose to use a generalized radius:

$$\widetilde{r} = \frac{r_a + r}{r_a + r_E} r_E, \tag{3.4}$$

where $r^2 = x^2 + y^2 + z^2$ is the Euclidean distance, $r_E^2 = (x/a_\Phi)^2 + (y/b_\Phi)^2 + (z/c_\Phi)^2$ is the *ellipsoidal* radius and r_a a characteristic scale. With this definition, $\widetilde{r} \approx r_E$ for $r \ll r_a$ and $\widetilde{r} \approx r$ for $r \gg r_a$. This formula uses the axis lengths characterizing the shape of the potential, $a_\Phi^2 + b_\Phi^2 + c_\Phi^2 = 3$, which will in general differ from the a, b, and c of the mass density (see e.g., Hayashi, Navarro & Springel, 2007). The potential at any point is,

$$\Phi(x, y, z) = \widetilde{\Phi}(\widetilde{r}), \tag{3.5}$$

where $\widetilde{\Phi}$ is a spherically symmetric potential model. Here we assume a spherical Einasto profile (Einasto, 1965).

We use Poisson's equation to derive a relation between the b/a and c/a of the density (which our method measures), and those of the potential b_Φ/a_Φ and c_Φ/a_Φ. This relation is then used for each of our subhalos, and as a result of this exercise, we obtain for our sample a median $b_\Phi/a_\Phi = 0.83$ and $c_\Phi/a_\Phi = 0.70$. When these values are plugged into the derived analytic expressions for b/a and c/a they are found to give a good representation of the median (density) axis ratios as a function of radius, as shown by the red dashed curve in Fig. 3.6. The median and $\pm 1\sigma$ error of the parameter fits for the density and axis ratios obtained in this way are given in Table 3.1.

3.4.2 The subhalo kinematics of luminous satellites

Fig. 3.7 shows the radial velocity dispersion σ_r (top) and the orbital anisotropy β (bottom), both as a function of distance along the major axis. As before, individual objects are shown with thin lines color-codded according to their V-band absolute magnitude. The median trend of the sample is indicated by a black solid curve, 1σ-equivalent percentiles in gray shading. The quantities are computed in ellipsoidal coordinates that follow the axis ratios of the mass density at each radius. In practice, we calculate the component of the velocity in the direction tangential to a given ellipsoid, σ_T, and the radial component σ_r is derived by subtraction in quadrature of σ_T from the total velocity dispersion. Both the radial velocity dispersion and anisotropy computed in this way (black solid curves) behave in a similar way to those obtained using simply spherical bins (black dotted lines).

The spread in σ_r seen in the top panel of Fig. 3.7 is due to the difference in mass of the subhalos, which span a range $m = 1.6 \times 10^8 - 5.8 \times 10^9$ $M_\odot$. The declining velocity dispersion profile is expected in CDM halos and is driven by the fall-off of the density and of the pseudo phase-space density $Q = \rho/\sigma_r^3$

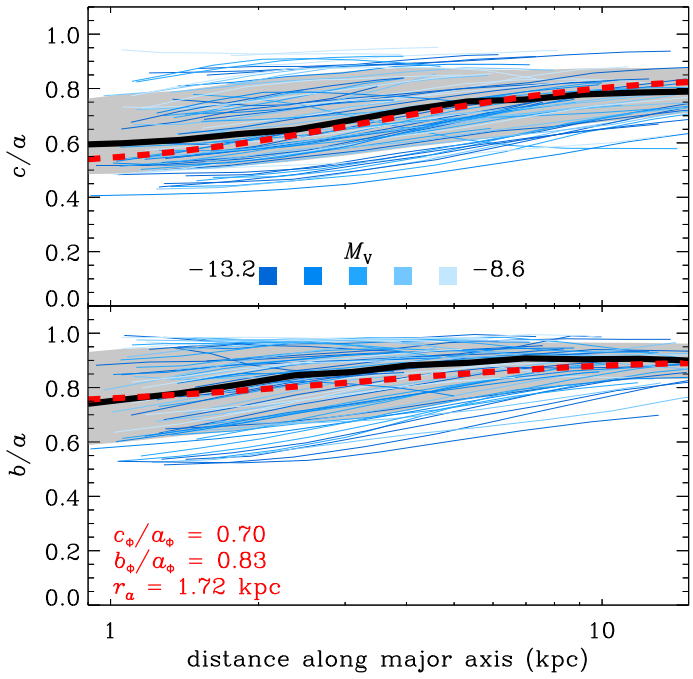

Figure 3.6: Shape as a function of the distance along the major axis, r, for the subhalos hosting luminous satellites. The dashed red lines correspond to the prediction of the model of Vogelsberger et al. to the axis ratios using the quoted values.

(Taylor & Navarro, 2001):

$$\frac{\varrho}{\widetilde{\sigma}_r^3} = Ax^{-\chi}, \tag{3.6}$$

with A a normalization constant, $\varrho \equiv \rho/\rho_{-2}$, $\widetilde{\sigma}_r \equiv \sigma_r/v_{-2}$ and $x \equiv r/r_{-2}$, where ρ_{-2}, v_{-2} and r_{-2} are the characteristic density, velocity and radius for the Einasto density profile respectively (See Appendix 3.6). We show in Fig. 3.10 of the Appendix that a power-law fit is a reasonable description of the pseudo phase-space of subhalos just like it is for field halos. However, unlike field halos, stripping induces some departure from the power-law behavior on the outer regions of subhalos. Such deviations start to be significant only beyond $\log_{10}(r/r_{-2}) > 0.6$.

We fit the Q-profiles individually for each subhalo, obtaining medians $\ln A = -2.42$ and $\chi = 1.60$ (see Table 3.1). These parameters, together with the median density profile, are then used in Eq. (3.6) to derive a mean radial velocity dispersion profile (green dashed line). As the figure shows, this provides an accurate description of the median σ_r obtained directly from the individual curves.

In the bottom panel in Fig. 3.7 we plot the ellipsoidal velocity anisotropy β profiles. In analogy to the spherical case, this is defined as $\beta = 1 - \sigma_r^2/\sigma_T^2$,

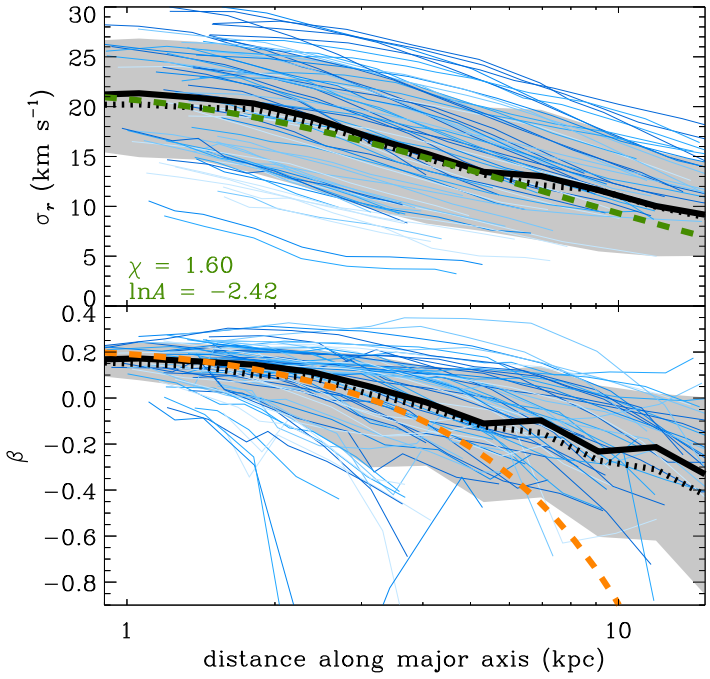

Figure 3.7: Radial velocity dispersion and anisotropy as a function of the distance along the major axis, r, for the subhalos hosting luminous satellites. The thick solid black line is the median when the velocity structure is averaged on elliptical bins and the dotted corresponds to the spherical case. The green line for σ_r is the value obtained assuming a power-law for the pseudo phase-space density distribution. For all models we assume that the density follows an Einasto profile with shape parameters α and scale radius r_{-2} given in Table 3.1. The orange line results from computing the anisotropy using Eq. (3.7) (the spherical Jeans equation).

where we calculate the component of the velocity tangential and radial to a given ellipsoid as explained above. Note that with this definition, β reduces to the usual anisotropy in the spherical limit.

The velocity anisotropy profiles of dark matter subhalos tend to decline with radius. In the inner regions the motions are slightly radially biased ($\beta \sim 0.2$ at $r \sim 1$ kpc), while the ellipsoid becomes increasingly tangential ($\beta < 0$) at larger radii. This behavior is markedly different from the radially-biased ellipsoids found in isolated ΛCDM halos, particularly in the outskirts (Cole & Lacey, 1996; Taylor & Navarro, 2001; Wojtak et al., 2005; Ludlow et al., 2010). This difference is a result of tidal forces, which preferentially remove particles with large apocenters on radial orbits. Fig. 3.7 also shows that subhalos rarely have a constant β profile.

Based on the similarity between the velocity anisotropy computed in ellip-

tical and spherical bins, we derive an expression for β using the spherical Jeans Equation, which relates the density, anisotropy and radial velocity dispersion of a system (Binney & Tremaine, 2008). In the case of an Einasto profile:

$$3\beta(r) = -\frac{6\pi\mu}{x\widetilde{\sigma}_r^2} + 5x^\alpha - \chi, \tag{3.7}$$

where $\widetilde{\sigma}_r = \sigma_r/v_{-2}$ as before and $\mu = \mu(x, \alpha)$ is given by Eq. (3.12) (see Appendix 3.6 for a more detailed derivation of this expression). The velocity anisotropy is therefore dependent on the logarithmic slopes of the mass density and of the pseudo phase-space density, α and χ, respectively.

The orange dashed line in the bottom panel of Fig. 3.7 shows the anisotropy obtained from Eq. (3.7) when using the median values of these parameters quoted in Table 3.1. It provides a reasonable fit out to $r \sim 2.5r_{-2}$. In the inner regions, a Taylor expansion of Eq. (3.7) yields:

$$3\beta(x) \approx -2\pi A^{2/3}\mathrm{e}^{2/3\alpha}x^{2-2\chi/3} + 5x^\alpha - \chi, \quad x \ll 1 \tag{3.8}$$

which allows to compute the asymptotic value of β close to the center from the parameters involved in the density and velocity profiles (see Appendix 3.6). In this regime $\lim_{r\to 0}\beta = -\chi/3$, which implies a negative anisotropy in the center. This however, is not necessarily inconsistent with studies of more massive, isolated objects which find $\beta \sim 0$ down to the resolution limit (e.g. Ludlow et al., 2011). For the typical values of α and χ found in our simulations, Eq. (3.8) predicts β to be positive (and very close to zero) up to $r \gtrsim 0.03r_{-2}$, typically $r \sim 30$ pc for our sample.

Whereas the limiting behavior of the anisotropy in the inner regions is similar for all subhalos, beyond a radius of ~ 1 kpc large variations are seen from object-to-object. These variations are still accounted for by Eq. (3.7) when each β profile is fitted individually. We find that the exact shape of the anisotropy profile depends most strongly on α, while χ determines where the velocity ellipsoid becomes tangential at large radii. On the other hand, variations in $\ln A$ have a very minor effect.

Although we have shown that the velocity ellipsoid in ellipsoidal coordinates is not very different from its spherically averaged version, we may ponder how to describe it in an axisymmetric sense. This is especially interesting since we have found that the subhalos are not significantly triaxial, and their b/a approaches unity at large radii. To this end, in Fig. 3.8 we explore the velocity structure in the radial and vertical direction. Each object is rotated such that the minor axis coincides with the z-direction. The velocity dispersion components along the vertical (z) and radial (R) axes provide information on how dynamically hot a system is in both directions. We compute this along the two preferential axis, minor (left) and major (right), using at each radius a sphere that contains 400 particles. The velocity dispersion σ_z and σ_R are then computed within these volumes and displayed as a function of distance along

the axes. As before, individual halos are shown in thin blue lines, the median values with solid thick lines.

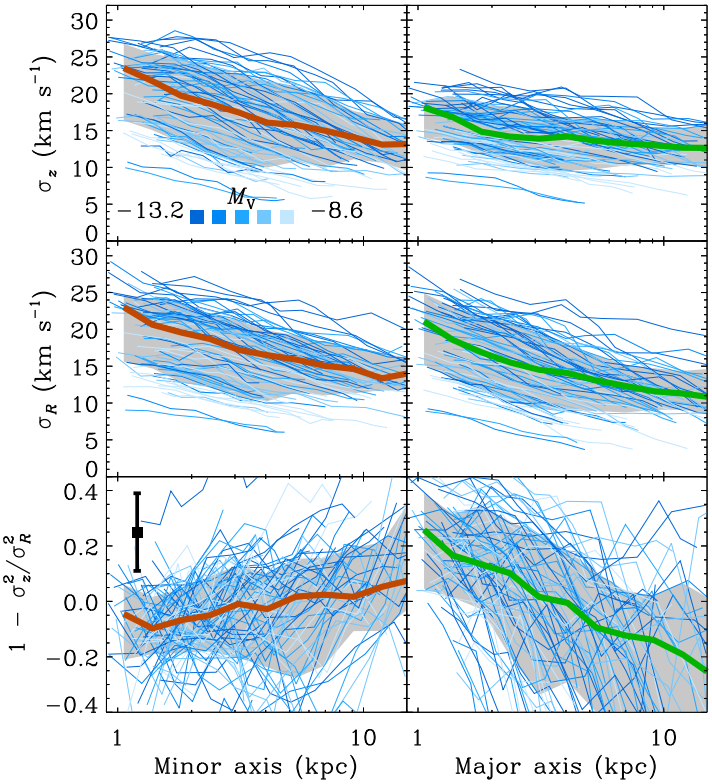

Figure 3.8: Velocity dispersion as a function of distance along the minor (left) and major axis (right) for subhalos hosting luminous satellites. In each case the system is rotated such that the minor axis lies along the z direction. The cylindrical velocity dispersions σ_z^2 and σ_R^2 are estimated in spheres containing 400 particles.

The velocity dispersion profiles show a steady decline with radius, with a trend somewhat flatter than the 3D radial velocity dispersion shown in Fig. 3.6. As in that case, there is scatter from object-to-object likely due to the range in subhalo mass. The anisotropy β_z is defined as $\beta_z = 1 - \sigma_z^2/\sigma_R^2$ and is shown in the bottom panels of Fig. 3.8. Interestingly, along the minor axis we find $\sigma_z \sim \sigma_R$, in agreement with the assumptions by Hayashi & Chiba (2012) when modeling stars in the dSph. However, this is not true for the velocity dispersions along the major axis as shown in the right panel, where we find positive values of β_z close to the center and $\beta_z < 0$ at the tidal radius. This trend, although systematic, is quite weak, with large scatter amongst the individual objects. It is important to realize that our measurements are subject to significant noise as we are now restricted to consider a small region

around a given radius (i.e. we do not average over entire ellipsoidal shells as before and so each sphere contains fewer particles). The typical uncertainty for the individual curves is shown by the black vertical error bar, computed as the dispersion obtained from drawing 100 samples with replacement in each bin.

The shapes of the subhalos are consistent with dynamical support by the velocity ellipsoid, as shown by Fig. 3.9. The vertical axis shows the local anisotropy $\delta = 1 - \sigma_z^2/\sigma_x^2$, where x is again the direction of the major axis and z points along the minor axis. These quantities are calculated in a sphere with 400 particles located at $x = 1$ kpc and the individual points in this figure correspond to the different subhalos. In the axisymmetric case, the virial theorem in tensor form (Binney, 2005) gives:

$$\frac{v_0^2}{\sigma_0^2} = 2(1-\delta)\frac{W_{xx}}{W_{zz}} - 2, \tag{3.9}$$

where W_{ij} are the components of the potential-energy tensor (Binney & Tremaine, 2008). For ellipsoidal systems W_{xx}/W_{zz} is a function of the ellipticity $\epsilon = 1 - c/a$ and is independent of the radial density profile (Roberts, 1962). v_0 is the streaming velocity along the y axis and σ_0 is the velocity dispersion in the x direction. The solid line in Fig. 9 indicates the prediction from Eq. (3.9) in the case of a dispersion supported system with $v_0/\sigma_0 = 0$.

3.5 Conclusions

We have used the Aquarius simulations to study the shapes of field and satellite dark matter halos with emphasis on the mass range expected for the hosts of the dwarf galaxies in the Local Group. We have used an iterative method based on the normalized inertia tensor to characterize the principal axis lengths $a \geq b \geq c$ of halos and subhalos as a function of radius. In particular, we have explored in detail halo shapes measured in the inner regions (radius of maximum circular velocity $r_{\rm max}$) and in the outskirts or *tidal contour*.

Through a comparison of objects in common between the different resolution levels of the Aquarius simulations, we have noticed that simple number of particles cuts do not guarantee convergence in the measured halo shapes, especially in the inner regions. We find that instead the *convergence radius* $r_{\rm conv}$ (defined as the threshold $\kappa = 7$ in the ratio between the local relaxation time and the dynamical time at the virial radius (Power et al., 2003)) provides a good estimate of the radius where the axis ratios are robustly determined (with an error $< 8\%$).

We have found that the typical axis ratios of isolated halos in the Aquarius simulations decrease with increasing mass, or equivalently maximum halo circular velocity $V_{\rm max}$, i.e. low mass objects tend to be more spherical than

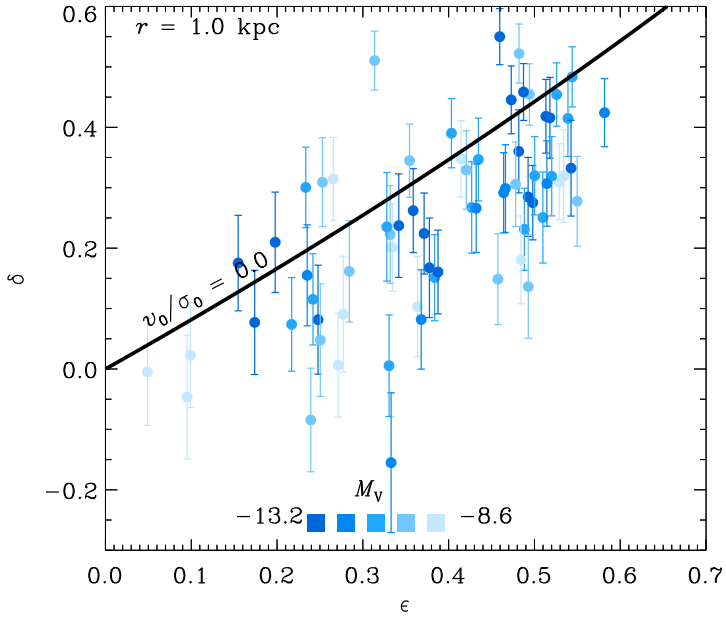

Figure 3.9: Relation between the anisotropy $\delta = 1 - \sigma_z^2/\sigma_x^2$ and the elliptical of the halos $\epsilon = 1 - c/a$ measured at a distance $x = 1$ kpc along the major axis. The solid black line shows the prediction of the virial tensor theorem when applied to axysimmetric systems supported by random motion (Binney, 2005).

Milky Way-like objects. These trends are well approximated by a relation between the axis ratio measured at the tidal radius $c/a|_{r_{\rm tidal}}$ and $V_{\rm max}$, i.e. $c/a|_{r_{\rm tidal}} \sim -0.021 \log V_{\rm max}$, while this relation is slightly steeper if the axis ratio is measured at $r_{\rm max}$ contour in which case $c/a|_{r_{\rm max}} \sim -0.032 \log V_{\rm max}$. The differences in the shapes of field vs satellite halos are small and within the intrinsic scatter of the samples. Nonetheless, at a fixed $V_{\rm max}$, subhalos tend to have larger axis ratios than isolated objects in the field.

The similarity between subhalos and field objects is also apparent in the lack of significant trends in the axis ratios with distance to the main host halo, d. We find, however, that the alignment of the ellipsoids varies with d: dark matter halos at close distances from the host center tend to be oriented preferentially with their major axis pointing radially. The signal disappears only for $d \gtrsim 2.5\ r_{\rm vir}$, where the orientations are consistent with random.

We have also focused on the properties of subhalos likely to host analogs of the *classical satellites* of the Milky Way ($-13.2 \leq M_V \leq -8.6$), according to the semianalytic model of galaxy formation run on the Aquarius suite by Starkenburg et al. (2012). Our analysis indicates that these galaxies are hosted by mildly triaxial dark matter objects with minor-to-major axis ratios $c/a \approx 0.60$ and intermediate-to-major $b/a \approx 0.75$ in the first kiloparsec with a clear

trend towards becoming axisymmetric in the outskirts. Their internal orbital structure shows evidence of being affected by tidal forces from their hosts (i.e. the main Aquarius halos), since the velocity anisotropy becomes tangential with radius, in clear contrast to what is found for isolated systems. We have also found that this orbital structure may be modeled in the axisymmetric context, where the velocity anisotropy $\beta_z \sim 0$ along the minor axis, and shows a very mild decline with distance along the major axis. These results may be used to motivate more realistic models of the subhalos hosting satellite galaxies like those observed around the Milky Way.

Acknowledgements

We thank Else Starkenburg for access to the semi-analytical catalog of the Aquarius simulations. AH gratefully acknowledges financial support from the European Research Council under ERC-Starting Grant GALACTICA-240271. The authors thank the hospitality of the Kavli Institute for Theoretical Physics, Santa Barbara during the program "First Galaxies and Faint Dwarfs: Clues to the Small Scale Structure of Cold Dark Matter", where part of this work was completed under the support of the National Science Foundation Grant No. NSF PHY11-25915.

3.6 Appendix: Einasto Profiles and The spherical Jeans equation

Following the method of Vera-Ciro et al. (2012) we fit a Einasto profile to the circular velocity profile of each individual subhalo of our sample. For each object we take 20 bins equally spaced in logarithmic space between $r_{\rm conv} < r < 0.9 r_{\rm tidal}$. We compute the cumulative circular velocity profile and fit an Einasto model by minimizing the merit function $E = \sum_{i=1}^{N_{\rm bins}} (\ln v_c^2(r_i) - \ln v_{c,i}^2)^2 / N_{\rm bins}$ against the free parameters r_{-2}, ρ_{-2} and α. Here, $v_{c,i}$ is the circular velocity corresponding to an Einasto profile with a scale radius r_{-2} (the radius at which the density profile has a slope -2), a characteristic density at r_{-2} equal to ρ_{-2} and a shape parameter that controls the overall slope of the profile, α. We deliberately chose the circular velocity profile over the more widely used density profile which is more sensitive to shot noise in each bin (see Vera-Ciro et al., 2012, for more details).

The density profile can be written as,

$$\rho(r) = \rho_{-2} \varrho(r/r_{-2}), \tag{3.10}$$

where

$$\ln \varrho(x) = -\frac{2}{\alpha}(x^\alpha - 1). \tag{3.11}$$

ϱ is therefore a dimensionless function of the dimensionless variable $x = r/r_{-2}$. In this spirit, it is possible to define a set of scaling factors in which we can express the dynamics of the system, namely, a characteristic mass $m_{-2} \equiv r_{-2}^3 \rho_{-2}$ and characteristic velocity $v_{-2}^2 \equiv G r_{-2}^2 \rho_{-2}$ (note that v_{-2} is not $v_{\rm circ}(r_{-2})$). The enclosed mass within a radius r is therefore $m(r) = 4\pi m_{-2} \mu(r/r_{-2})$, where

$$\begin{aligned} \mu(x) &= \int_0^x dx\, x^2 \varrho(x) \\ &= \frac{1}{\alpha} \exp\left(\frac{3\ln\alpha + 2 - \ln 8}{\alpha}\right) \gamma\left(\frac{3}{\alpha}, \frac{2x^\alpha}{\alpha}\right), \end{aligned} \tag{3.12}$$

with γ the lower incomplete gamma function. In a similar fashion we can define a dimensionless version of the radial velocity dispersion $\widetilde{\sigma}_r(x) \equiv \sigma_r(r_{-2}x)/v_{-2}$.

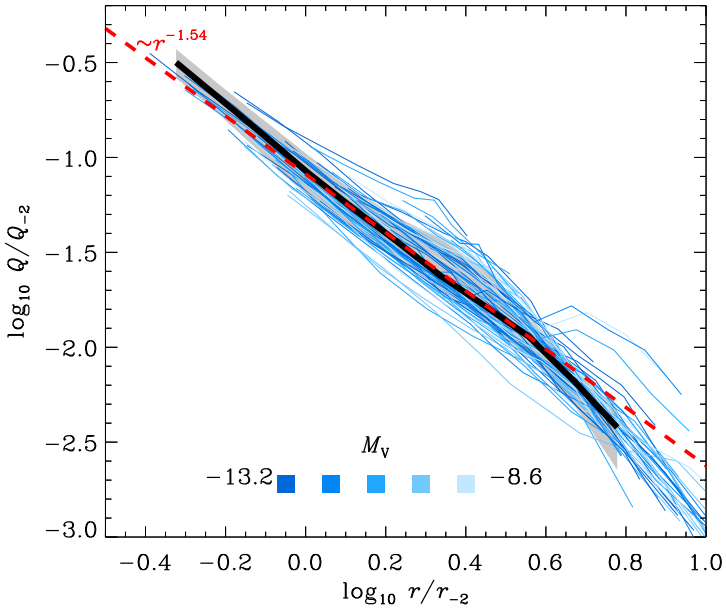

Figure 3.10: Pseudo-phase space density profile $Q/Q_{-2} = \varrho/\widetilde{\sigma}_r^3$ for the subhalos hosting luminous dwarfs in our sample. The black line shows the mean profile of all subhalos and the red curve indicates the best power law fit $Q \sim r^{-1.54}$.

It has been previously reported in the literature that the pseudo phase-space density profile of isolated dark matter halos can be well modeled by a single power law $Q \equiv \rho/\sigma_r^2 \sim r^{-\chi}$, $\chi > 0$ (Taylor & Navarro, 2001; Dehnen & McLaughlin, 2005; Navarro et al., 2010; Ludlow et al., 2011). Fig. 3.10 shows Q measured for our sample of subhalos hosting luminous satellites. We have found that the slope χ is slightly shallower than for objects in the field ($\chi \sim 1.6$ versus $\chi \sim 1.8$ for isolated halos). The best fit values of the parameters, and their variance, are given in Table 3.1.

Notice that the pseudo-phase-space profiles start to deviate from a power-law in the outer regions, likely induced by ongoing tidal stripping. This typically occurs for $\log r/r_{-2} \geq 0.6$, which is roughly the same scale at which our fit for the radial velocity dispersion σ_r deviates from the mean subhalo trends shown in Fig. 3.7.

Using the dimensionless quantities introduced before, we can now write the spherical Jeans equation as:

$$\begin{aligned} & \frac{d}{dx}(\varrho\widetilde{\sigma}_r^2) + 2\frac{\beta}{x}(\varrho\widetilde{\sigma}_r^2) = -\frac{4\pi\varrho\mu}{x^2} \\ \Rightarrow \quad & \frac{d\ln\varrho}{d\ln x} + 2\frac{d\ln\widetilde{\sigma}_r}{d\ln x} + 2\beta = -\frac{4\pi\mu}{x\widetilde{\sigma}_r^2}. \end{aligned} \tag{3.13}$$

We can use Eq. (3.11) to further reduce this expression:

$$3\beta(x) = -\frac{6\pi\mu}{x\widetilde{\sigma}_r^2} + 5x^\alpha - \chi. \tag{3.14}$$

The limiting value of this expression at small radii can be obtained from a Taylor expansion around zero. For $x \ll 1$ we may use that $\lim_{x\to 0}\gamma(s,x)/x^s = 1/s$ (Abramowitz & Stegun, 1972). Finally

$$\begin{aligned} \ln\varrho(x) &\approx \frac{2}{\alpha}, \\ \mu(x) &\approx \frac{1}{3}x^3\mathrm{e}^{2/\alpha}, \\ \widetilde{\sigma}_r(x) &\approx A^{-1/3}\mathrm{e}^{2/3\alpha}x^{\chi/3}, \qquad x \ll 1, \end{aligned}$$

which leads to,

$$3\beta(x) \approx -2\pi A^{2/3}\mathrm{e}^{2/3\alpha}x^{2(1-\chi/3)} + 5x^\alpha - \chi, \qquad x \ll 1. \tag{3.15}$$

CHAPTER 4

Not too big, not too small: the dark halos of the dwarf spheroidals in the Milky Way

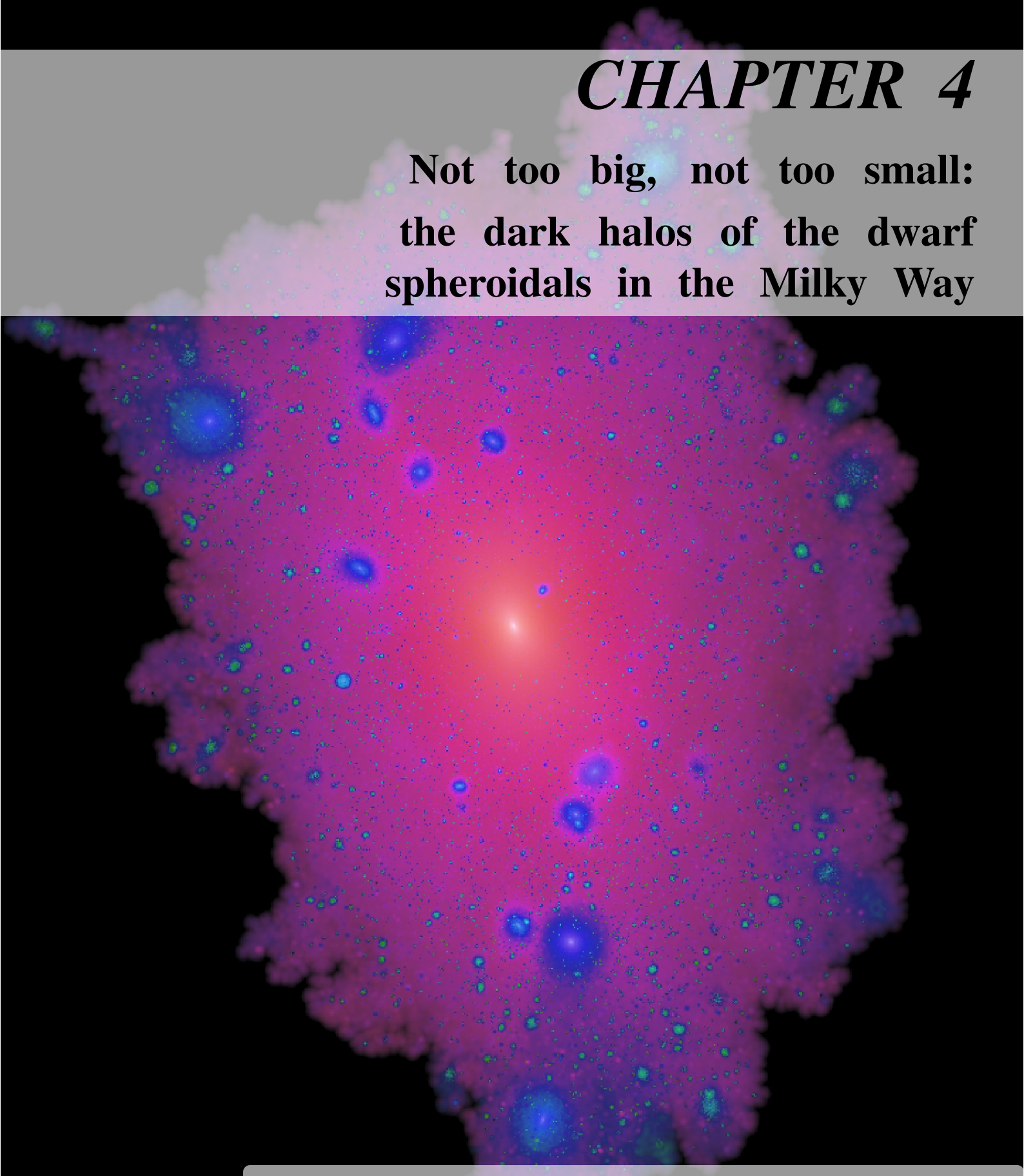

Carlos A. Vera-Ciro, Amina Helmi, Else Starkenburg and Maarten A. Breddels

Accepted for publication in MNRAS

Abstract

We present a new analysis of the Aquarius simulations done in combination with a semi-analytic galaxy formation model. Our goal is to establish whether the subhalos present in ΛCDM simulations of Milky Way-like systems could host the dwarf spheroidal (dSph) satellites of our Galaxy. Our analysis shows that, contrary to what has been assumed in most previous work, the mass profiles of subhalos are generally not well fit by NFW models but that Einasto profiles are preferred. We find that for shape parameters $\alpha = 0.2 - 0.5$ and $v_{\rm max} = 10 - 30$ km/s there is very good correspondence with the observational constraints obtained for the nine brightest dSph of the Milky Way. However, to explain the internal dynamics of these systems as well as the number of objects of a given circular velocity the total mass of the Milky Way should be $\sim 8 \times 10^{11}$ $M_\odot$, a value that is in agreement with many recent determinations, and at the low mass end of the range explored by the Aquarius simulations. Our simulations show important scatter in the number of bright satellites, even when the Aquarius Milky Way-like hosts are scaled to a common mass, and we find no evidence for a missing population of massive subhalos in the Galaxy. This conclusion is also supported when we examine the dynamics of the satellites of M31.

Cover: Aq-A-2 and its most massive satellites ($v_{\rm max} > 30$ km s^{-1})

4.1 Introduction

Despite the great success of the ΛCDM concordance cosmological model on large scales, on the scales of galaxies and below the theory is often defied. Some of the issues on small scales have been consistently explained within the theory itself with the inclusion of physical processes that mostly affect baryons. This is the case for the "missing satellite problem" (Klypin et al., 1999b; Moore et al., 1999), namely the overabundance of satellites in dark matter only simulations compared to the observed number of luminous objects around the Milky Way and other nearby galaxies. It is now widely accepted that the shallow potential wells of small dark matter halos must be strongly affected by reionization and feedback, making star formation highly inefficient in such systems (Couchman & Rees, 1986; Efstathiou, 1992; Kauffmann, White & Guiderdoni, 1993; Thoul & Weinberg, 1996; Bullock, Kravtsov & Weinberg, 2000; Somerville, 2002; Benson et al., 2002; Li et al., 2009; Okamoto & Frenk, 2009; Macciò et al., 2010; Stringer, Cole & Frenk, 2010; Font et al., 2011; Guo et al., 2011).

Recently, Boylan-Kolchin, Bullock & Kaplinghat (2011) have argued that the dark matter satellites (subhalos hereafter) predicted by ΛCDM are persistently too dense to host the observed population of dwarf spheroidal galaxies (dSph) in the Milky Way if these are embedded in halos following Navarro, Frenk & White (1996, 1997, hereafter NFW) profiles. More recently, Boylan-Kolchin, Bullock & Kaplinghat (2012b) presented an even stronger argument (free of the assumption of a specific density profile) and argued that the Milky Way is missing a population of massive satellites. A few studies have been published in the literature that address this conundrum. Lovell et al. (2011a) showed that in warm dark matter cosmological simulations of Milky Way-like halos, the circular velocity curves of subhalos are consistent with the constraints derived by Wolf et al. (2010) for the Milky Way satellites (see also Walker et al., 2009). Following a similar line, Vogelsberger, Zavala & Loeb (2012) carried out simulations of self-interacting dark matter and showed that the most massive subhalos develop cores, what could partially solve the problem. On the other hand, Di Cintio et al. (2011) pointed out that by including baryons in the cold dark-matter context the problem becomes more severe probably due to the additional adiabatic contraction experienced by the dark matter subhalos hosting gas.

There are two assumptions sometimes implicit in the models which may lead to biased answers if overlooked. These concern (i) the actual mass of the Milky Way[1] and, (ii) the density profiles followed by dark matter satellites

[1]In fact, shortly after we submitted our manuscript for publication, Wang et al. (2012) analysed the Millennium Simulation series and used the invariance of the scaled subhalo velocity function to argue that the absence of massive subhaloes might indicate that the MW is less massive than commonly assumed.

assembled in ΛCDM. The first issue has been addressed with a plethora of methods leading to measures that, usually, are consistent with a total mass of $0.7 - 2.0 \times 10^{12}$ $M_\odot$ (Kochanek, 1996; Wilkinson & Evans, 1999; Sakamoto, Chiba & Beers, 2003; Battaglia et al., 2005, 2006; Smith et al., 2007; Li & White, 2008; Xue et al., 2008; Kallivayalil et al., 2009; Guo et al., 2010; Watkins, Evans & An, 2010; Gnedin et al., 2010; Busha et al., 2011a). The measurements suffer from uncertainties in the modeling as well as limitations in the kinematics of the tracers used. Therefore comparisons to simulations of Milky Way dark matter halos should take into account this uncertainty.

On the second issue, namely the density profile of subhalos, significant progress has been made, especially in recent years. Already Stoehr et al. (2002) found that the circular velocity curves of subhalos in cosmological N-body simulations are more narrowly peaked (in a log-log plot) than the widely used NFW models and explored how consistent these were with the internal kinematics of the Milky Way satellites. The outstanding numerical resolution achieved in the latest of such cosmological N-body simulations has enabled a closer examination of the shape of the density profile down to the innermost few parsecs of dark matter halos (Springel et al., 2008; Madau, Diemand & Kuhlen, 2008). Such studies have shown that Einasto models provide better matches to the density profiles found in the simulations than the NFW form (Navarro et al., 2010; Reed, Koushiappas & Gao, 2011; Di Cintio et al., 2012), confirming previous results on the subject (Navarro et al., 2004; Merritt et al., 2005, 2006; Graham et al., 2006; Prada et al., 2006; Gao et al., 2008).

In this Chapter, we will reconsider both these issues and establish how much they affect the conclusions drawn by Boylan-Kolchin, Bullock & Kaplinghat (2011, 2012b). Like these authors we use the Aquarius halos, but we supplement the dynamical information provided by the simulations with a semi-analytic galaxy formation model (Starkenburg et al., 2012). One of the advantages of this approach is that it enables us to directly compare objects in the simulation with those observed. We introduce some relevant features of the simulations in Section 4.2, while in Section 4.3 we present in detail the results of our analysis. We draw our conclusions in Section 4.4.

4.2 Numerical Preliminaries

We use the simulations of the Aquarius project, six Milky Way-sized dark matter halos assembled in a background cosmology consistent with the constraints yielded by WMAP-1. Each halo (labeled from `A` to `F`) was simulated at different resolutions, starting from a particle mass $m_p = 3.143 \times 10^6$ $M_\odot$ for the lowest and $m_p = 1.712 \times 10^3$ $M_\odot$ for the highest resolution. In what follows we focus on the level `2` which is the highest level at which *all* the Aquarius halos were simulated (For more details see Springel et al., 2008).

Subhalos in these simulations are identified as bound overdensities with

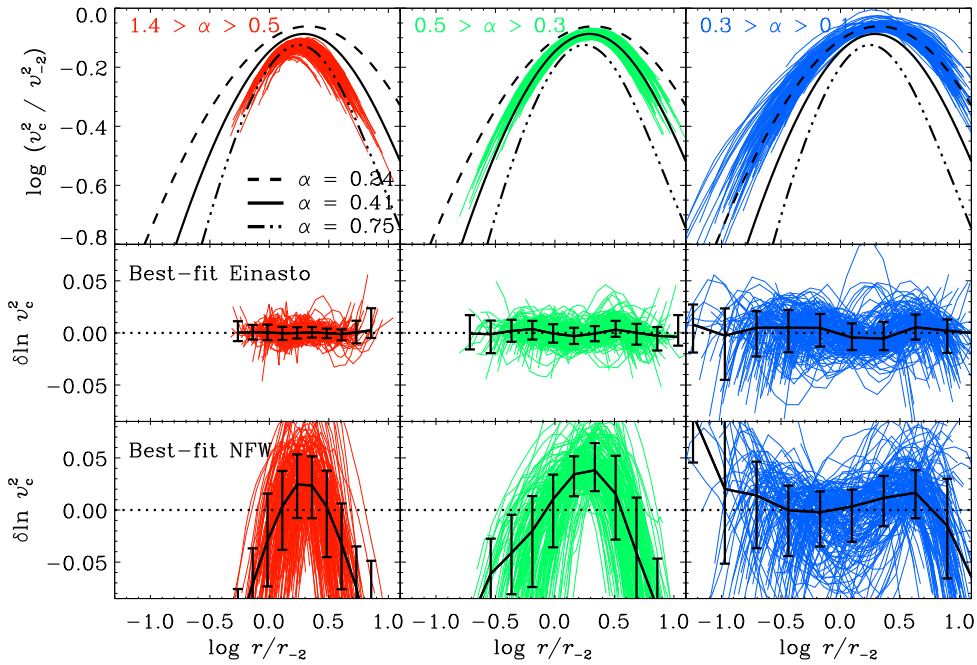

Figure 4.1: Spherically averaged circular velocity profiles $v_c^2(r) = Gm(r)/r$ for the subhalos that are predicted to host stars by our semi-analytic model. Velocities have been scaled to $v_{-2}^2 \equiv 4\pi G\rho_{-2}r_{-2}^2$. As already reported in Stoehr et al. (2002) the velocity profiles of subhalos tend to be more narrowly peaked than in the NFW form. The sample of subhalos has been grouped according to the best fit value of α, and plotted with different colors. The number of objects in each α-bin is 154. An Einasto profile with the average value of α for each bin is overplotted, while the median $v_{\rm max}$ in each α-bin is 13.6, 20.3 and 27 km s^{-1} from left to right, and the $v_{\rm max}$ ranges given by the 68% percentiles for each panel are (10, 26.2), (15.9, 26.2) and (20.5, 44.8) km s^{-1}, respectively. The residuals from the best-Einasto (NFW) fits are shown in the middle (bottom) panel, and in general are consistent with zero for the Einasto profile and exhibit systematic deviations from zero for the NFW case. In the column $\langle\alpha\rangle = 0.24$ both models yield similar results, which is naturally expected since the NFW equivalent is reached with $\alpha = 0.22$. The systematic change of $r_{\rm conv}/r_{-2}$ with α is a consequence of setting the convergence parameter κ to a fixed value.

SUBFIND (Springel et al., 2001). For each subhalo we compute the circular velocity profile as $v_c^2(r) = Gm(r)/r$, where $m(r)$ is the mass enclosed within the spherical radius r. The maximum circular velocity $v_{\rm max}$ is defined as the peak of the circular velocity curve, and is reached at position $r_{\rm max}$, i.e. $v_c(r_{\rm max}) = v_{\rm max}$.

Numerical convergence is established by looking at the convergence radius as defined by Power et al. (2003). Navarro et al. (2010) showed that the roots

of the equation

$$\kappa = \frac{\sqrt{200}}{8} \frac{n(r)}{\ln n(r)} \left[\frac{\overline{\rho}(r)}{\rho_c} \right]^{-1/2}, \tag{4.1}$$

correspond to different degrees of convergence depending on the value of the parameter κ. In this equation $n(r)$ is the number of particles enclosed within the radius r and $\overline{\rho}(r)/\rho_c$ is the spherical density at this position in units of the critical value. Comparing the various resolutions of the Aquarius simulations, Navarro et al. (2010) showed that $\kappa = (7.0, 1.0, 0.4)$ correspond to deviations in the circular velocity profile of about $(2.5\%, 10\%, 15\%)$ respectively. Here, we use $r_{\rm conv}(\kappa = 0.4)$ for each subhalo. We also define the tidal radius $r_{\rm tidal}$ of a subhalo as that which encompasses 95% of the bound particles. The results from our definition show good agreement with the output from more sophisticated expressions for the tidal radius (Tormen, Diaferio & Syer, 1998).

To make more direct comparisons to the satellite population of the Milky Way, we have also run a semi-analytic model of galaxy formation for all the Aquarius halos. This model is based on that originally developed by Kauffmann et al. (1999); Springel et al. (2001); De Lucia, Kauffmann & White (2004); Croton et al. (2006); De Lucia & Blaizot (2007) and later modified to describe more accurately processes on the scales of dwarf galaxies (Li, De Lucia & Helmi, 2010). The implementation used here also includes recipes for stellar stripping and tidal disruption. The resulting satellite luminosity function agrees well with that of the Milky Way as reported by Koposov et al. (2008) (see Section 4.3.3). Also the internal properties of the satellites, such as scaling relations, metallicities and star formation histories are in good agreement with those observed (for more details see Starkenburg et al., 2012).

4.3 Results

4.3.1 About the density profiles

It is has been already reported in the literature that the mass profiles of ΛCDM halos deviate from the NFW functional form (Stoehr et al., 2002; Navarro, Abadi & Steinmetz, 2004; Merritt et al., 2005, 2006; Graham et al., 2006; Prada et al., 2006; Gao et al., 2008). Using the Aquarius simulations, Navarro et al. (2010) showed that a parametric model with a density profile with logarithmic slope described by a power-law (Einasto profile) provides better fits for objects of virial mass $\sim 10^{12}$ $M_\odot$. The power index α adds another free parameter, therefore the fits are expected to improve. Nevertheless, it was shown by Springel et al. (2008) that even after fixing $\alpha = 0.16$ the Einasto profile still yields much better results. The nature of the shape parameter α has been recently investigated for isolated objects with masses in excess of 5×10^{12} $M_\odot$ and the results suggest a deep connection with the pseudo-phase-space density

distribution (Ludlow et al., 2011). For subhalos Springel et al. (2008) also showed that the mass profiles follow much closer the Einasto than the NFW model. For both models, the mass enclosed within the spherical radius r can be written as

$$m(r) = 4\pi r_{-2}^3 \rho_{-2} g(r/r_{-2}), \tag{4.2a}$$

where r_{-2} is the radius at which the logarithmic slope of the density profile reaches the isothermal value and ρ_{-2} is the density at that position. The details of each model are inherited by the function g, which takes the form

$$g_{\rm NFW}(x) = 4\ln(1+x) - \frac{4x}{1+x}, \tag{4.2b}$$

for the NFW profile, and

$$g_{\rm Einasto}(x) = \frac{1}{\alpha}\exp\left(\frac{3\ln\alpha + 2 - \ln 8}{\alpha}\right)\gamma\left(\frac{3}{\alpha}, \frac{2x^\alpha}{\alpha}\right), \tag{4.2c}$$

for the Einasto model. Here $\gamma(a,x)$ is the lower incomplete gamma function. Although intrinsically different, these profiles resemble each other for $\alpha \approx 0.22$ in $0.01 \leq r/r_{-2} \leq 100$. That means that objects that have a shape parameter close to this value are well fitted by either model. Fig. 4.1 shows the spherically averaged circular velocity profiles $v_c^2 = Gm(r)/r$ for all the subhalos that are predicted to host stars according to our semi-analytical model. In total we calculate 20 bins in the region $r_{\rm conv} \leq r \leq 0.9\, r_{\rm tidal}$, we use this upper cutoff to ensure that our fits are not driven by tidal effects. All objects have at least 200 particles, but generally significantly more than 1000. For each of the plotted subhalos we calculate the merit function

$$E = \frac{1}{N_{\rm bins}}\sum_{i=1}^{N_{\rm bins}} (\ln v_c^2(r_i) - \ln v_{c,i}^2)^2, \tag{4.3}$$

and minimize it against the free parameters of each model. We have deliberately chosen to use the cumulative mass instead of the differential profile since it is less sensitive to the shot-noise of each bin, as a consequence we can go to low number of particles, whenever the restriction $n(0.9\, r_{\rm tidal}) - n(r_{\rm conv}) \geq 200$ is met.

Fig. 4.1 shows the results of our fitting procedure. Here the subhalos have been distributed in bins with equal number of objects (namely 154), and according to their best fit α value. The three different columns show the subhalos that fall into each α-bin, the average α within each bin is quoted in the top-left panel. Each curve in the top row has been conveniently normalized to a characteristic velocity $v_{-2}^2 \equiv 4\pi G\rho_{-2} r_{-2}^2$ and the characteristic radius r_{-2}. We have also overplotted the predicted Einasto profiles for the average α. The middle panels show the residuals of the best-Einasto fit for each subhalo, the thick line represent the median and 1σ equivalent dispersion. The residuals are

consistent with zero indicating that the Einasto profile fits better than NFW (whose residuals are shown in the bottom panel), especially for large α values. Interestingly, for $\langle\alpha\rangle = 0.24$ the NFW model provides a good and comparable fit to the Einasto model (see bottom-right panel). This is actually expected, since $\alpha = 0.22$ represents a model that nearly follows the NFW profile.

On average lower mass subhalos tend to have larger values of α. However this correlation has a large scatter, for instance the maximum circular velocity for objects in the central panel of Fig. 4.1, i.e. those with $0.3 < \alpha < 0.5$ is in the range $10.5 < v_{\rm max}/{\rm km\ s^{-1}} < 48.2$.

4.3.2 MW's dSphs constraints revisited

Wolf et al. (2010) have shown that the mass enclosed within the half light radius $r_{1/2}$ of a dynamical system can be robustly determined as $m_{1/2} = 3G^{-1}\langle\sigma_v^2\rangle r_{1/2}$, without (precise) knowledge of its velocity anisotropy. Here $\langle\sigma_v^2\rangle$ is the light-weighted average line-of-sight velocity dispersion of the system. In the case of dSph galaxies, this effectively implies a measurement of the circular velocity at $r_{1/2}$, which therefore constrains the possible family of circular velocity curves for a given dark matter density profile. Following Boylan-Kolchin, Bullock & Kaplinghat (2011) we plot in Fig. 4.2 the 2σ constraints derived in this way for the 9 most luminous dSphs satellites of the MW (i.e. excluding the Sagittarius dwarf galaxy and the Small and Large Magellanic Clouds). Like Boylan-Kolchin, Bullock & Kaplinghat (2011) here we assume these systems are embedded in NFW profiles, which leads to the gray band shown in the figure. This band is also nearly consistent with the masses enclosed within 300 pc as reported by (Strigari et al., 2008) $2.5\times10^6 \leq m(300\ {\rm pc})/{\rm M}_\odot \leq 3.0\times10^7$.

The advantage of using this plot is that one can directly compare against the results extracted from ΛCDM simulations. The filled circles in Fig. 4.2 show the distribution of $(r_{\rm max}, v_{\rm max})$ measured directly from our simulations for the satellites hosting stars. The colors indicate the predicted luminosities and the sizes correspond to the bound mass fraction at present day, i.e. $f_{\rm bound} = m(0)/m(z_{\rm infall})$, where $z_{\rm infall}$ is the lowest redshift at which the progenitor of a given subhalo was not associated to one of the main Aquarius halos. Here, the values $(r_{\rm max}, v_{\rm max})$ have been corrected for softening length effects following the expressions given by Zavala, Springel & Boylan-Kolchin (2010). As highlighted in the Introduction, there are important differences in the location of the points from the simulations and those derived for the dSph satellites of the Milky Way, which may lead to the conclusion that there is a significant problem with our currently preferred cosmological model.

However, this comparison may be need to be revisited since we demonstrated in the previous section that an NFW profile is not expected to describe well the dark matter halos of satellites in ΛCDM. Therefore, we have computed the family of $(r_{\rm max}, v_{\rm max})$ values that are consistent with the measurement of

$v_c(r_{1/2})$ for the dSph of the Milky Way, but now we have considered Einasto profiles. The 2σ constraints are shown in Fig. 4.2. Given the freedom we have in choosing the extra parameter α, we have plotted 3 different bands corresponding to $\alpha = (0.22,\ 0.30,\ 0.50)$. The $\alpha = 0.22$ (solid lines) is consistent with the NFW predictions, as expected. For values of $\alpha \lesssim 0.5$ (dashed line) the constraints from observations actually overlap with those found in the simulations. This range of values of α lies well within the range observed in Fig. 4.1, since $\sim 2/3$ of our sample has $\alpha < 0.5$.

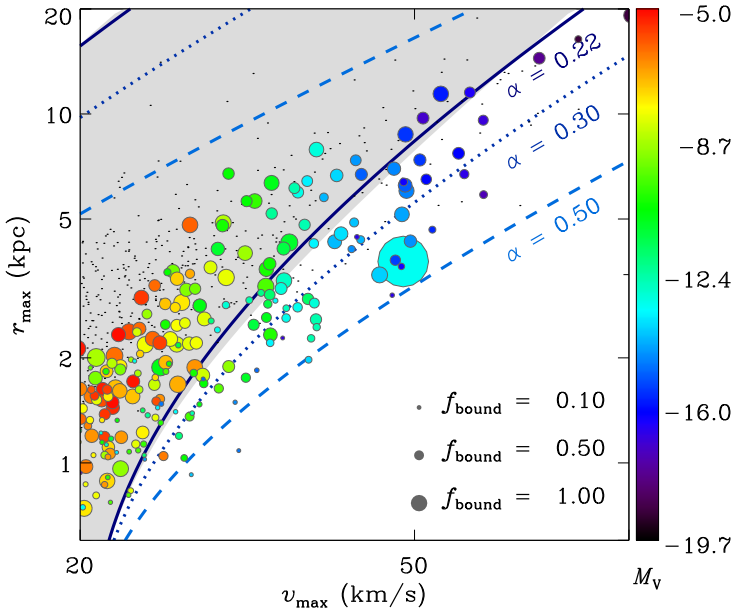

Figure 4.2: Constraints for the MW's dwarf spheroidals using NFW (gray band) and Einasto (blue curves) profiles. Points are the results from the six Aquarius halos, colored according to their predicted luminosity and sized using the fraction of mass retained after infall. The cyan point at $v_{max} \sim 50$ km s^{-1} represents a subhalo that underwent a merger with another substructure after infall, therefore increasing its mass. The black dots correspond to isolated halos in the simulations.

From Fig. 4.2 we note that there is a correlation between the value of α and f_{bound} i.e. the amount of stripping a subhalo has experienced. Very heavily stripped objects require, on average, higher α, and deviate the most from NFW profiles. The black dots in this figure correspond to the location of isolated dark matter halos in the same v_{max} range as the satellites. This confirms that such isolated dark matter halos are well-fit by NFW profiles, and that tidal stripping is acting on the subhalos to change the shape of their circular velocity profile to the Einasto form (see also Hayashi et al., 2003).

The mismatch between the observations (with the assumption of NFW,

Boylan-Kolchin, Bullock & Kaplinghat, 2011) and the simulations is only partly alleviated with the use of an Einasto profile as Fig. 4.2 shows. The Milky Way does not have many very luminous dwarf galaxy satellites. Brighter than Fornax ($M_V \sim -13.2$), only the Sagittarius dwarf and the Magellanic Clouds are known, and none is included in Fig. 4.2. According to our semi-analytic model such luminous objects would populate the upper-right of this plot, i.e. $v_{\rm max} \gtrsim 40$ km/s and $r_{\rm max} \gtrsim 2.5$ kpc. Therefore, in this region of the diagram, the mismatch between the observations and the simulations *has* to be entirely attributed to the absence of other bright dSph in the Milky Way, which is the point originally raised by Boylan-Kolchin, Bullock & Kaplinghat (2011). In other words, the lack of objects brighter (or more massive) than Fornax around the Milky Way cannot be explained away through a change in the density profile of the dark matter subhalos in the context of the ΛCDM model, unless these have been very heavily stripped. However, such massive subhalos are typically accreted late, and hence have not suffered significant amounts of stripping. It is the region with $v_{\rm max} \sim 20-40$ km/s, where we expect to find the subhalos hosting most of the classical dSph according to this plot, where the difference between assuming an NFW or an Einasto profile needs to be taken into account to bring the simulations in agreement with the observations.

4.3.3 Effects of the host halo mass

Springel et al. (2008) have shown that the mass function of dark matter halos is independent of mass, i.e. that it is self-similar. This implies that the number of subhalos of a given mass scales directly with the mass of the host (although Gao et al., 2012, suggest that the slope is slightly larger for 10^{15} $M_\odot$ objects). Therefore, we can expect that, down to a certain scale, brighter or more massive central galaxies will host a larger number of satellites. This is indeed shown in the top panel Fig. 4.3, where we have plotted the luminosity function of all Aquarius halos. It is clear from this figure that this is the case, since the three heavier of the Aquarius halos `Aq-A-2`, `Aq-C-2` and `Aq-D-2` have 57, 62 and 67 satellites respectively, while the lightest, `Aq-B-2` has only 36 satellites with $M_V \leq -5$, and hence has the shallowest luminosity function in the faint end. It is possible to show that a doubling of the mass of the host halo roughly leads to an increase by a factor of ~ 2 in the number of satellites brighter than $M_V = -5$ (Starkenburg et al., 2012).

We thus explore the effect of host halo mass on the properties of our simulated satellites, by re-scaling all halos to a common value following Helmi, White & Springel (2003). Because of the scale-free nature of gravity, we may assume that if a halo of mass $M_{\rm Aq}$ is scaled to have a mass $M_{\rm MW}$ then the subhalos's masses m should be scaled as

$$\widetilde{m} = m\frac{M_{\rm MW}}{M_{\rm Aq}} \equiv \mu m. \tag{4.4a}$$

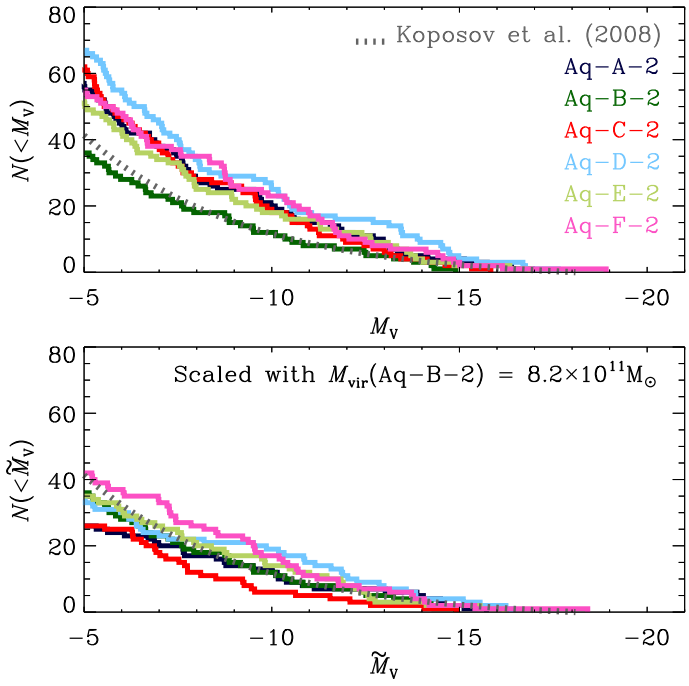

Figure 4.3: Luminosity function for the original Aquarius simulations (top) and once they have scaled to the mass of `Aq-B-2` (bottom). For reference we have added the luminosity function derived by Koposov et al. (2008) for the Milky Way. This takes into account incompleteness issues for satellites with $M_V > -11$ and, for brighter objects it considers the average for the Milky Way and M31. Although in the scaled version the simulations follow much more closely the observations, some differences remain in the number of satellites of a given luminosity.

Naturally the distances will become

$$\widetilde{r} = \mu^{1/3} r, \tag{4.4b}$$

while the circular velocity profiles

$$\widetilde{v_c} = \left(\frac{G\widetilde{m}}{\widetilde{r}}\right)^{1/2} = \mu^{1/3} v_c. \tag{4.4c}$$

To determine the factor $\mu \equiv M_{\rm MW}/M_{\rm Aq}$, we need to specify $M_{\rm MW}$. As discussed in the Introduction, the value of the total mass of the Milky Way is quite uncertain. However, motivated by the remarkable match between the luminosity function of `Aq-B-2` and that of the Milky Way (Koposov et al., 2008), we set $M_{\rm MW} = M_{\rm vir}$(`Aq-B-2`) $= 8.2 \times 10^{11} {\rm M}_\odot$[2]. This value is consistent

[2]In this Chapter we denote $M_{\rm vir} = M_{200}$, i.e. the the mass enclosed in a sphere with mean density 200 times the critical value.

with many recent studies using different techniques (e.g. Battaglia et al., 2005, 2006; Smith et al., 2007; Xue et al., 2008). This implies that the value of μ ranges from unity to 2.2 at most, which implies that distances and velocities in the scaled simulations will be at most decreased by a factor of 1.3.

We run our semi-analytic galaxy formation model now for the re-scaled Aquarius simulations. The resulting luminosity function is shown in the bottom panel of Fig. 4.3, where the new predicted magnitudes are denoted by $\widetilde{M}_V$. It is evident from this figure that each halo now follows much more closely the Milky Way's luminosity function. It is important to note that there is still some halo-to-halo dispersion, which can be attributed to the stochastic nature of the mass assembly of each object. That is, not all the galaxies with the same mass are expected to have the same number of satellites with the same luminosity, although some form of statistical equivalence should be present.

We now study more closely the circular velocity profiles of the subhalos hosting satellites, since previous works have highlighted a discrepancy between the observations and the simulations (Boylan-Kolchin, Bullock & Kaplinghat, 2011; Lovell et al., 2011a). Fig. 4.4 shows the scaled circular velocity profiles for all the subhalos hosting satellites with luminosities in the quoted range. As in previous sections, we have also included the estimates for the 9 most luminous dSphs of the Milky Way following Wolf et al. (2010). The first conclusion is that our semi-analytic model places (satellite) galaxies of a given luminosity in the right mass (sub)halos, since the amplitude of the rotation curves in all cases are consistent with those observed. Secondly, the number of objects per luminosity bin is in good agreement with the number observed, as established in Fig. 4.3. For example, in the most luminous bin (top panel) the median number of bright satellites per halo is 3, while for intermediate luminosities it is 4, and for the faintest considered here, it is 4. We emphasize however that the range within a given luminosity bin is quite broad. For example for the brightest bin, the scaled `Aq-A-2` has just 1 satellite, while the scaled `Aq-D-2` has 7. Such large variations are not unexpected, but stresses that strong conclusions cannot be drawn when the number of objects is so small as in the case of the bright end of the luminosity function.

The galaxies shown in the fainter two bins agree quite well with the predictions of our models. There is no systematic mismatch, with the dSph circular velocity measurements at the half-light radius lying close to the median velocity profile of the simulated satellites. An apparent discrepancy is present in the most luminous bin $-13.2 \leq \widetilde{M}_V \leq -11.9$ in the sense that there is a larger number of subhalos with circular velocities above the measured values for Fnx and Leo I than there is below. Nevertheless as discussed above, this comparison is limited by statistics and affected by stochastic aspects in the luminosity function.

We quantify this by comparing the observed value of the circular velocity at $r_{1/2}$ for each dSph, with the probability distribution function of v_c calculated at

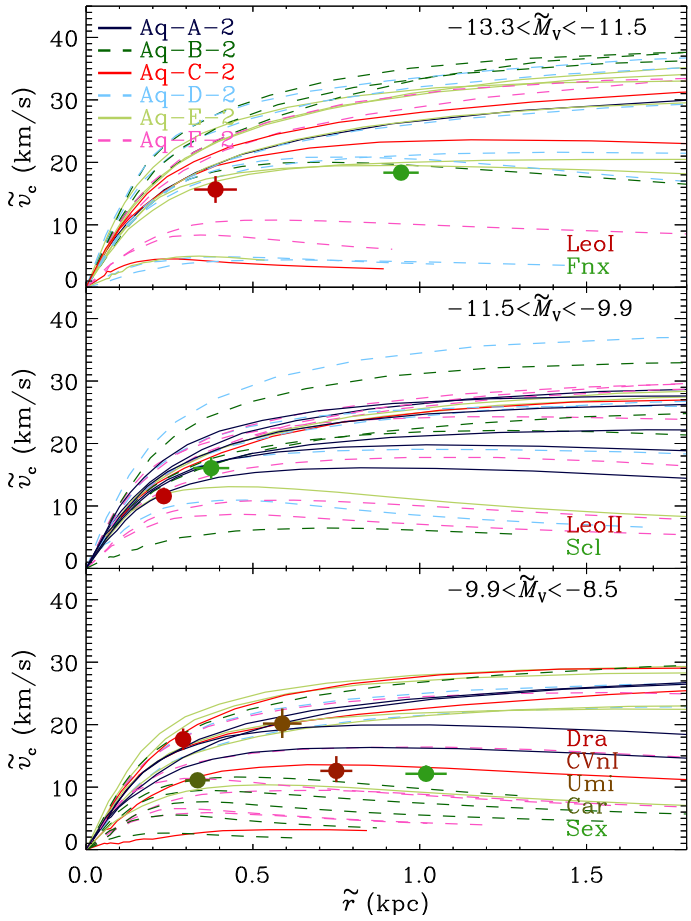

Figure 4.4: Circular velocity profiles for scaled subhalos in three different luminosity bins, following the absolute magnitudes of the nine classical dSph of the Milky Way. The subhalos are colored according to the host halo they are associated with. This figure shows that the number of satellites per bin, as well as the velocities profiles are consistent with the measurements obtained for the dSph.

dSph	$N\sigma$ away	Observed $v_c(r_{1/2})$	Median $v_c(r_{1/2})$	med(v_c) -1σ	med(v_c) $+1\sigma$
Fnx	-0.72	18.3	25.4	6.0	32.0
LeoI	-0.73	15.7	19.4	8.2	24.5
Scl	-0.47	16.1	17.6	12.8	20.8
LeoII	-1.03	11.6	14.2	11.9	16.8
Sex	-0.22	12.1	16.4	4.4	25.3
Car	-0.40	11.1	13.6	6.6	20.0
Umi	$+0.62$	20.2	16.2	5.8	22.4
CVnI	-0.23	12.6	16.3	5.1	23.0
Dra	$+1.03$	17.7	13.6	6.7	17.6

Table 4.1: Statistical comparison of the 9 most luminous classical dSphs with the simulated velocity profiles in Fig. 4.4.

the same radius using all the subhalos that lie in the corresponding luminosity bin. We compute the median v_c and two percentiles of the distribution, namely a lower (15.9%) and an upper (84.1%) value, which would correspond to $\pm 1\sigma$ in the case of a Gaussian. The results of this experiment are shown in Table 4.1 for the different satellites. Note that here we have translated the probability into an "equivalent" $N\sigma$ away from the median. The table shows that all satellites are consistent with being drawn from the population of subhalos hosting galaxies found in our simulations.

Thus far we have focused on the nine classical dSph, and have excluded from the analysis the Sagittarius dwarf and the Magellanic Clouds. One of the questions originally posed by Boylan-Kolchin, Bullock & Kaplinghat (2012b) is that there may be a hidden population of very massive subhalos in the Milky Way, since the circular velocities of the classical dwarfs are lower than those found for the nine most massive (at infall) subhalos in any of the Aquarius simulations. So far we have shown that our model predicts the satellites of a given luminosity to be hosted in subhalos of the right mass, when comparing to the classical dSph. However we also need to explore what happens for systems brighter than Fnx, and whether we indeed expect a missing population from our models. As expected, the scaled Aquarius halos show a diverse number of systems with $\widetilde{M}_V < -14$, ranging from 2 for `Aq-C-2` to 5 for `Aq-A-2`. A simple comparison to the Milky Way satellite system would suggest that we cannot argue that there is a population of massive satellites that is missing.

This conclusion is also reached when considering $v_{\rm max}$ instead of luminosity. Although in general the most luminous objects are hosted by the most massive subhalos, for $v_{\rm max} < 40$ km/s and $\widetilde{M}_V > -14$ there is significant scatter, and objects as bright as Fnx are hosted in subhalos with $v_{\rm max} \sim 5-35$ km/s as the

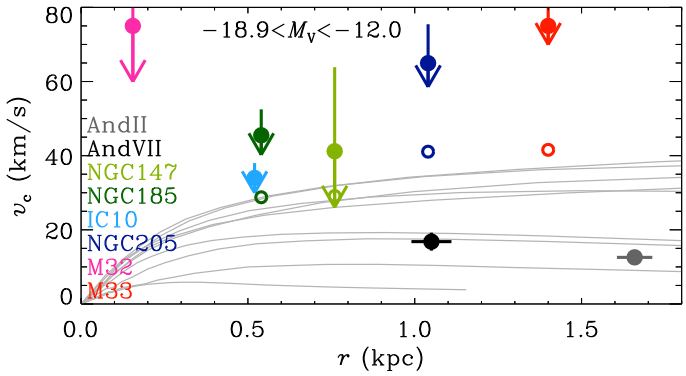

Figure 4.5: Circular velocities for the subhalos present in halo `Aq-C-2` associated to satellites with luminosities $M_V \leq -12$. The symbols represent observations of the satellites of M31 in the same luminosity range. Open symbols represent the estimated dark matter contribution to $v_c(r)$ when the decomposition is available (see text for details).

top panel of Fig. 4.4 shows. On the other hand, objects brighter than Fnx are generally hosted by subhalos with $v_{\rm max} > 40$ km/s. We find a median number of such subhalos of 2 within 280 kpc from the center for the scaled-down main Aquarius halos, with 3 for `Aq-A-2` and none for `Aq-C-2`.

As suggested by multiple authors, the dark matter mass of M31 is almost twice that of the Milky Way (e.g. Li & White, 2008; Kallivayalil et al., 2009; Guo et al., 2010). This would imply that M31 should host more, and also brighter, satellites than the Milky Way itself. This indeed appears to be the case, as M31 has 8 satellites within 280 kpc that are brighter than Leo I ($M_V = -11.9$) compared to 2 (or 5 when Sgr and the Magellanic Clouds are included) for the Milky Way.

Aquarius halo `Aq-C-2` has $M_{\rm vir} = 1.77 \times 10^{12}$ M$_\odot$ which is ~ 2.2 times larger than our candidate for the Milky Way, making this object a good match for M31. In Figure 4.5 we show the velocity profiles of all the nine satellites in `Aq-C-2` with $M_V \leq -12$. We have also included measurements for M31's satellites with luminosities in that range. It is important to bear in mind that these measurements have been derived using a variety of methods that range from HI rotation curves for IC10 (Wilcots & Miller, 1998) and M33 (Corbelli, 2003), to 3 integral dynamical modelling for NGC147, NGC185 and NGC2005 De Rijcke et al. (2006). For the dSph AndII and AndVII the method presented by Wolf et al. is used to estimate $v_c(r_{1/2})$ (Kalirai et al., 2010), while for M32 the mass is derived through Jeans modelling (Magorrian & Ballantyne, 2001). Many of these bright dwarf galaxies are not as dark matter dominated within the region populated by the stars as the dSph, and hence a direct comparison to the circular velocity of the subhalos is not quite correct. For example, for

NGC147, NGC185 and NGC2005 the dark matter content is estimated to be 50%, 40% and 40%, respectively (De Rijcke et al., 2006). The open symbols in Fig. 4.5 correspond thus to the dark matter contribution to the circular velocity as estimated by these authors, while the solid points represent the total enclosed mass at the given radius. Clearly for M32, a very compact dwarf elliptical, the shown circular velocity is also an upper limit for the dark matter contribution.

This comparison shows that the velocity profiles for our most luminous satellites in `Aq-C-2` are very consistent with the observations of the dwarfs in M31 over a similar luminosity range. We therefore must conclude there is no evidence of a missing population of very massive of dark satellites.

4.4 Discussion and Conclusions

We have used the state of the art cosmological N-body simulations of Milky Way-like dark matter halos of the Aquarius project, supplemented with a semi-analytic galaxy formation model, to study the dynamical properties of the satellite population in the Local Group.

We have found that the mass profiles of the subhalos associated to bright satellites according to our model deviate from the standard NFW form (see also Stoehr et al., 2002), and that Einasto profiles provide much better fits. The shape parameter α exhibits a correlation with the amount of mass stripped since the time of accretion, indicating that tidal effects may be responsible for the changes in the profiles of dark matter halos once they become satellites (Hayashi et al., 2003).

The comparison of our models to current measurements of the mass enclosed within the half mass radius for the classical dwarf spheroidals suggests that they are embedded in dark matter halos of $v_{\rm max} \sim 10 - 30$ km/s with $\alpha \sim 0.2 - 0.5$. In principle, this prediction for the values of the shape parameter α could be tested observationally. However this requires very extensive sampling of the kinematics of stars near the center of the dwarf galaxies. It is also necessary to perform more sophisticated dynamical models, that are free of assumptions regarding the velocity anisotropy of the systems. For example Schwarzschild models of the Sculptor dSph constrain the inner logarithmic slope of the dark matter density profile to be $d\log\rho/d\log r > -1.5$ (Breddels et al., 2012b). Better constraints could be obtained if the sample size were increased by a factor ~ 10.

We have also shown that the number and internal dynamics of the classical dSph in the Milky Way are consistent with the predictions of the ΛCDM model, if the Milky Way's mass is $\sim 8 \times 10^{11}$ $M_\odot$. This value well within the range measured using the dynamics of stellar tracers, but suffers from significant uncertainties. However, it is important to note that this low value lowers the probability of a galaxy like the Milky Way to host two satellites as bright as

the Small and Large Magellanic Clouds (Busha et al., 2011b; Boylan-Kolchin et al., 2010), although such systems appear to be rare in any case, as shown by Liu et al. (2011) using the Sloan Digital Sky Survey.

We have also found significant scatter in the number of subhalos expected to host bright satellites for the Aquarius halos, even when scaled to a common mass of 8×10^{11} $M_\odot$. For example, the scaled `Aq-A-2` has five satellites brighter than Fornax, while the scaled `Aq-C-2` has only two (making it consistent with our Galaxy). Therefore, care should be taken to draw strong conclusions from this region of the luminosity function since the number of objects is small and heavily influenced by the host mass as well as by stochastic effects associated to particular histories. Another example that emphasizes this point is given by M31, which plausibly is nearly a factor of two more massive than the MW, and also has a larger number of bright satellites. Just like for the Milky Way, our models for the satellite population of M31 are consistent with the observational constraints on the internal dynamics of the brighter satellites, after taking into account the differences in host mass.

A similar conclusion was reached by Wang et al. (2012) in a paper submitted shortly after ours, and based on the Millenium simulation series. These authors show that the cumulative number of subhalos with a given peak circular velocity depends roughly linearly on host halo mass, and that it is a highly stochastic quantity. In fact, once normalized to the mass of the host, this function is close to Poissonian. Based on this result, they conclude that $\sim 46\%$ of the halos with $M = 10^{12}$ $M_\odot$ have no more than 3 subhalos more massive than $v_{\rm max} = 30$ km/s, and that the percentage increases to $\sim 61\%$ for halos with $M = M(\texttt{Aq-B-2}) = 8.2 \times 10^{11}$ $M_\odot$, in good agreement with our own inferences. Hence we must conclude that we have found no evidence of a missing massive satellite problem in the Local Group.

Acknowledgments

The Aquarius simulations have been run by the VIRGO consortium, and we are very thankful to this collaboration, and especially indebted to Volker Springel. We are very grateful to Gabriella De Lucia and Yang-Shyang Li in relation to the semi-analytic model of galaxy formation, and to Simon White, Mike Boylan-Kolchin and the referee for a critical reading of the manuscript. AH gratefully acknowledges financial support from the European Research Council under ERC-Starting Grant GALACTICA-240271. ES is supported by the Canadian Institute for Advanced Research (CIfAR) Junior Academy and a Canadian Institute for Theoretical Astrophysics (CITA) National Fellowship.

CHAPTER 5

Constraints on the shape of the Milky Way's dark matter halo from the Sagittarius stream

Carlos A. Vera-Ciro & Amina Helmi

In preparation

Abstract

We present a new model for the dark matter halo of the Milky Way that fits the properties of the stellar streams associated with the Sagittarius dwarf galaxy. In the inner regions, the halo potential is axisymmetric and oblate with $q_z = 0.9$, and therefore is consistent with the expected response to the formation of a baryonic disk in its center. In the outskirts, the halo follows the shape proposed by Law & Majewski (2010), namely a nearly oblate ellipsoid oriented perpendicular to the Galactic plane. This outer halo can be made more triaxial, with minor-to-major axis ratio $c/a = 0.8$ and intermediate-to-major axis ratio $b/a = 0.9$ if the effect of the Large Magellanic Cloud is taken into account, and thereby made reconcilable with the predictions of ΛCDM simulations.

5.1 Introduction

In the last decade, the stellar stream associated with the Sagittarius (Sgr) dwarf galaxy, has been extensively used as a probe of the mass distribution in the Milky Way (MW). Of particular interest is the constraining power that the properties of the stream have on the dark matter component out to ~ 60 kpc from the Galactic center. However, it has turned out to be particularly challenging to put this idea into practice.

Early results showed, for example, that the halo may be spherical and that extreme oblate configurations ($q_z < 0.7$) could be confidently rejected (Ibata et al., 2001). However, the advent of new data led to new puzzles. The most well known being that the line of sight velocities of Sgr's leading stream favor a prolate halo (Helmi, 2004), while the tilt of its orbital plane would require an oblate mass distribution (Johnston, Law & Majewski, 2005). On the other hand, the so-called bifurcation of the leading arm was proposed by Fellhauer et al. (2006) to be an older stream wrap, but this would be possible only if the halo potential were close to spherical. Recent observations by Koposov et al. (2012) have cast doubt that both bifurcation arms have originated in the Sgr dwarf galaxy. In fact, Helmi et al. (2011) found in the cosmological Aquarius simulations (Springel et al., 2008; Cooper et al., 2010) that streams associated with different progenitors may overlap on the sky as a consequence of their correlated infall directions (Libeskind et al., 2011; Lovell et al., 2011b) and their tendency to infall in groups (Li & Helmi, 2008). In this case, the bifurcation would not offer any direct constraints on the Milky Way halo shape.

A possible solution to the oblate vs. prolate conundrum was recently proposed by Law & Majewski (2010) (see also Deg & Widrow, 2012) and requires that the Milky Way is embedded in a triaxial halo, with its intermediate axis aligned with the spin of the Galactic disk. Although the halos assembled in ΛCDM are expected to be triaxial (Jing & Suto, 2002; Hayashi, Navarro & Springel, 2007; Schneider, Frenk & Cole, 2012), this configuration is difficult to reconcile with the prediction of the formation of MW-like objects. For example, cosmological N-body simulations predict that Milky Way-like halos have shapes that vary as a function of radius. Typically they are prolate in the inner kiloparsecs and smoothly transit towards a more triaxial geometry at the virial radius (Vera-Ciro et al., 2011). Furthermore, the settling of a disk at the center of the halo leads to a change in its orbital structure, and to a more oblate shape in its inner regions (Dubinski, 1994; Debattista et al., 2008; Kazantzidis, Abadi & Navarro, 2010; Abadi et al., 2010; Tissera et al., 2010; DeBuhr, Ma & White, 2012; Bryan et al., 2012). Moreover, even if the halo is assumed to be static, and insensitive to the presence of baryons, the stability of the disk would not be naturally ensured in the potential of Law & Majewski (2010) (because of the lack of tube orbits around the intermediate axis,

see Heiligman & Schwarzschild, 1979). Interestingly, evidence a halo changing shape with radius has been reported by Banerjee & Jog (2011). These authors used the flaring of the HI layer of the MW disk to show that an axisymmetric halo model with increasing major to minor axis ratios as a function of radius, is favored by these observations.

When modeling the dynamics of the stellar streams associated with the Sagittarius dwarf galaxy, the presence of substructures in the halo has often been neglected (although see Zhao, 1998; Johnston, Spergel & Haydn, 2002). Although we expect a large number of dark matter satellites in the halos of galaxies (Klypin et al., 1999b; Moore et al., 1999), and these may affect the appearance of streams (Yoon, Johnston & Hogg, 2011), only the most massive exert significant heating. Furthermore, objects as massive as the Large Magellanic Cloud (LMC) could also affect the orbital path of the stream. If the present day LMC mass is $\sim 10^{11}$ $M_\odot$ (Besla et al., 2007), its contribution to the gravitational pull on the stars in the Sgr streams is as important as the one generated by the enclosed mass inside the orbit of Sgr, and therefore, strong enough to alter their dynamics.

Motivated by the above discussion and given the limitations of the available models, in this Chapter we take a fresh look at the dynamics of the Sgr streams. In Section 5.2 we introduce a model for the halo that takes into account the effect of a baryonic disk. Section 5.3 is devoted to study the effect of the LMC on the Sgr stream. In this section we also compare the predictions of the new models, and explore in addition the differences for older wraps. Finally in Section 5.4 we summarize our conclusions.

5.2 Inner halo: Accounting for baryonic effects on the halo shape

5.2.1 Description of the potential

As discussed in the introduction and despite the success of the triaxial model by Law & Majewski (2010), it is difficult to reconcile the proposed mass distribution with the prediction from simulated halos assembled in ΛCDM. The triaxial model that better fits the observations is nearly oblate, with its minor axis pointing almost parallel to the direction of the Sun. This halo model has constant axis ratios, and although the potential in the inner few kiloparsecs is almost axisymmetric, it does not follow the symmetry of the visible components, as its symmetry plane is perpendicular to the disk. Furthermore, the natural expectation is that the dark halo should become more oblate as a response to the presence of gas forming a disk in the center of the potential

well.

In this context, a sensible conjecture would be that the Milky Way halo transits from an oblate to a triaxial configuration with increasing Galactocentric distance. To model such profile we follow the approach of Vogelsberger et al. (2008). Consider the spherical potential,

$$\Phi_s(r) = v_{\rm halo}^2 \ln(r^2 + d^2), \tag{5.1}$$

where the s subscript is used to emphasize the spherical nature of this model. We want to construct a model for the potential of the halo that satisfies the following requirements:

1. It is axisymmetric in the inner parts, with its symmetry plane coinciding with the plane of the disk. This will guarantee the stability of the latter, as well as account for the effects of the disk on the dark halo.

2. It is triaxial in the outer parts. More specifically, we want it to follow the model of Law & Majewski (2010) which is known to fit well the dynamics of the stream.

3. It has a smooth transition between these two regimes.

It is clear that the information about the geometrical properties of the potential are encapsulated in the variable $r = (x^2 + y^2 + z^2)^{1/2}$. Therefore we replace $r \rightarrow \widetilde{r}$, with

$$\widetilde{r} \equiv \frac{r_a + r_T}{r_a + r_A} r_A, \tag{5.2}$$

where r_a is a scale radius, and

$$r_A^2 \equiv x^2 + y^2 + \frac{z^2}{q_z^2} = R^2 + \frac{z^2}{q_z^2}, \tag{5.3}$$

$$r_T^2 \equiv C_1 x^2 + C_2 y^2 + C_3 xy + \frac{z^2}{q_3^2}, \tag{5.4}$$

with

$$\begin{aligned} C_1 &= \frac{\cos^2\phi}{q_1^2} + \frac{\sin^2\phi}{q_2^2}, \\ C_2 &= \frac{\cos^2\phi}{q_2^2} + \frac{\sin^2\phi}{q_1^2}, \\ C_3 &= 2\sin\phi\cos\phi\left(\frac{1}{q_1^2} - \frac{1}{q_2^2}\right). \end{aligned} \tag{5.5}$$

Note that for $r \ll r_a$ $\widetilde{r} \approx r_A$, and similarly $r \gg r_a$ $\widetilde{r} \approx r_T$. We have thus defined the quantity r_T in the same way as Law & Majewski (2010). The potential

$$\Phi_{\rm halo}(x, y, z) = \Phi_s(\widetilde{r}(x, y, z)), \tag{5.6}$$

therefore behaves as asymmetric for $r \ll r_a$ (Helmi, 2004), and triaxial for $r \gg r_a$ (Law & Majewski, 2010). Note that the Sun is assumed to be located along the x axis, at $x = -R_\odot$, and the z axis points perpendicular to the disk.

As often assumed in the literature, we model the disk and bulge components following a Miyamoto-Nagai (Miyamoto & Nagai, 1975) distribution and a Hernquist spheroid (Hernquist, 1990), respectively. The corresponding gravitational potentials of these components are

$$\Phi_{\rm disk}(R, z) = -\frac{GM_{\rm disk}}{\sqrt{R^2 + (a + \sqrt{z^2 + b^2})^2}}, \tag{5.7}$$

and

$$\Phi_{\rm bulge}(r) = -\frac{GM_{\rm bulge}}{r + c}, \tag{5.8}$$

we set the values of the parameters to those used by Helmi (2004).

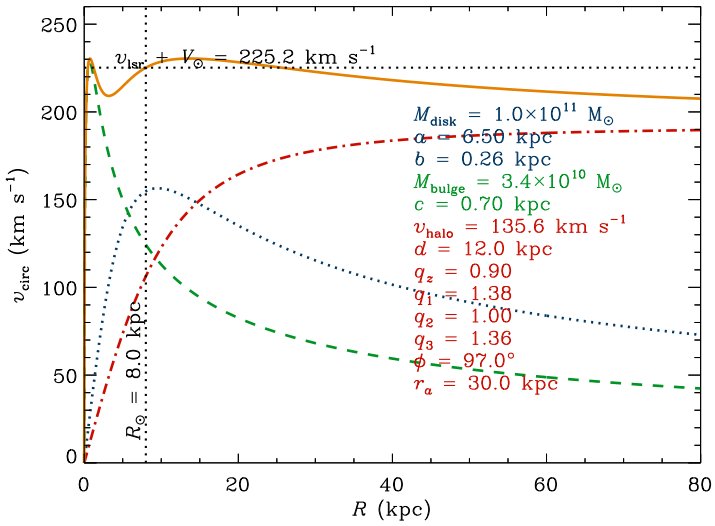

Figure 5.1: Circular velocity profile for the disk (dotted blue), bulge (dashed green) and halo (dash dotted red). The halo makes a transition from oblate to triaxial at $r_a = 30$ kpc, and its amplitude is constrained by the circular velocity at the position of the Sun. The profile including all components is shown with the solid orange line.

In Fig. 5.1 we show the circular velocity profile of this composite model. Since it is not symmetric, we define $v_c^2 = \boldsymbol{r} \cdot \partial\Phi/\partial\boldsymbol{r}$, and plot this quantity

along the axis $R = x$. For this particular model we chose the flattening of the axisymmetric component to be $q_z = 0.9$, the value required to fit the tilt in the orbit of the leading arm of the stream in the axisymmetric case (e.g. Johnston, Law & Majewski, 2005). The axis ratios for triaxial component (q_1, q_2, q_3), as well as its tilt ϕ, are taken from the model proposed by Law & Majewski (2010). The amplitude of the potential $v_{\rm halo}$ (Eq. 5.1) is fixed to ensure that $v_{\rm circ}(R = R_\odot = 8\,{\rm kpc}) = v_{\rm LSR} + V_\odot = 225.2$ km s^{-1}. The transition radius $r_a = 30$ kpc, is selected such that the region of dominance of the disk (as measured from the rotation curve) resides inside the axisymmetric component of the halo potential.

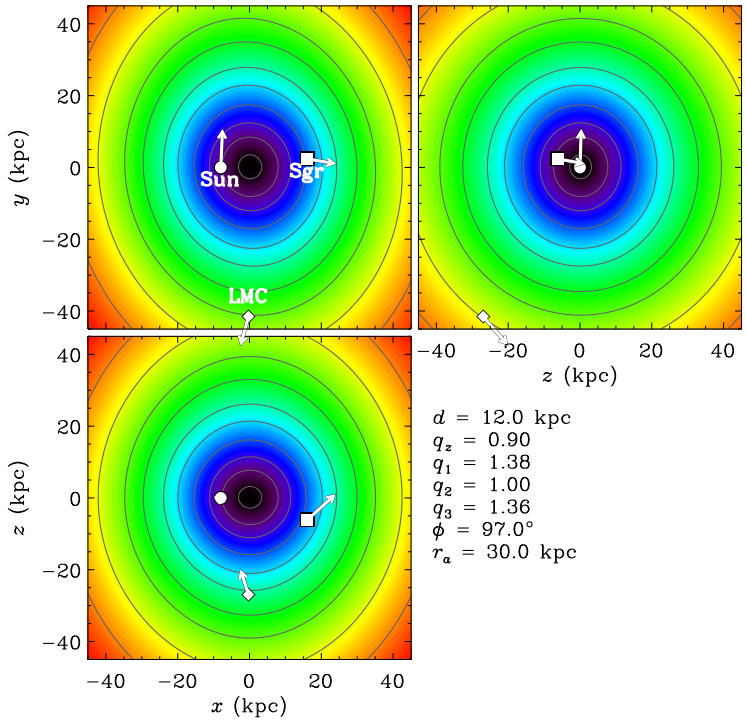

Figure 5.2: Dark matter halo potential on the plane $z = 0$ (top left), $y = 0$ (bottom left) and $x = 0$ (top right). For reference we have included the positions and directions of motions for the Sun (circle), the Sagittarius dwarf galaxy (square) and the Large Magellanic Cloud (diamond).

Fig. 5.2 shows slices of the dark halo potential given by Eq. (5.6) on three different planes. For reference we have added the positions and directions of motion for the Sun (circle), the Sagittarius dwarf galaxy (square) and the Large Magellanic Cloud (diamond), where the length of each arrow is proportional to the projection of the velocity vector on each of the planes. By construction, the potential is nearly oblate near the center, with its axis of symmetry in the z direction. Then it becomes increasingly triaxial as one moves outwards. Recall that in the triaxial regime, the potential in Eq. (5.6) actually describes

an extreme oblate mass distribution aligned with the x axis, and with an effective flattening $\sim 1/q_1 \approx 0.7$.

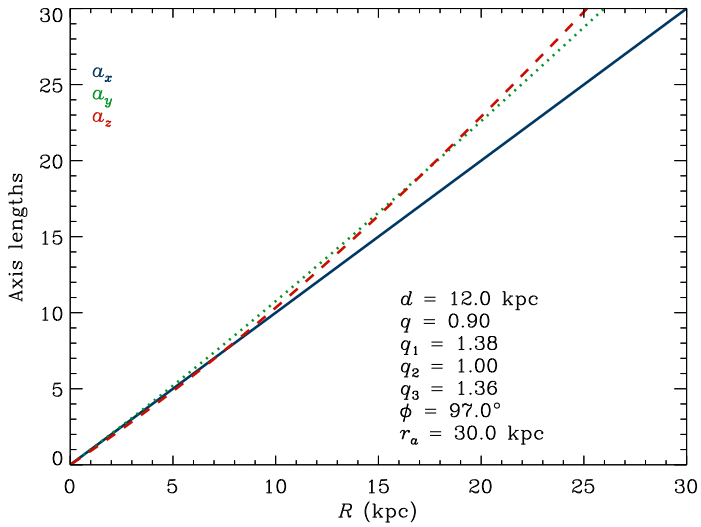

Figure 5.3: Lengths along x (solid blue), y (dotted green) and z (dashed red) of the equipotential of the dark halo model of (5.6)

Note also that although the transition radius is set at $r_a = 30$ kpc, the effective transition between the axisymmetric and triaxial regimes, occurs at a smaller distance ($r \approx 10$ kpc). This can be best concluded from Fig. 5.3, where we plot the axis lengths calculated assuming that $\widetilde{r} \approx (x/a_x)^2 + (x/a_y)^2 + (x/a_z)^2$, which given that $\phi \approx 90°$, is a reasonable approximation. At the center of the halo $a_x = a_y > a_z$, which means that it is axisymmetric here (oblate in the xy plane). However, in the outskirts $a_z \gtrsim a_y > a_x$, leading to an almost oblate potential, but now with its minor axis pointing along the x direction.

Figures 5.1, 5.2 and 5.3 encapsulate the properties of our fiducial model for the potential: the mass of each component is consistent with observations, and the geometry of the dominant (by mass) halo is, by construction, more consistent with simulations of MW-like objects. Whether this potential reproduces the dynamics of the Sgr stream is the focus of the next section.

5.2.2 Generating the stream

We proceed to integrate test particles in the compound potential described in the previous section. In what follows we work under the assumption that the orbit of the center of mass of Sgr will follow closely the path of the tidal streams, although it has been reported in the literature that this might not be the case (Choi, Weinberg & Katz, 2007; Eyre & Binney, 2009). However, our approach is cost-effective and it serves as a good approximation when compared

to actual N-body simulations (Law & Majewski, 2010). In the future we also plan to include the effect of dynamical friction (Jiang & Binney, 2000).

For each orbit we generate a set of initial conditions consistent with the present day six dimensional phase-space coordinates of the Sgr dwarf galaxy. More specifically, we sample each observable from a Gaussian distribution, with its mean and variance taken from the values reported in the literature. The position is assumed to be at $(l, b) = (5.6°, -14.2°)$ (Majewski et al., 2003), the heliocentric distance $d = 25 \pm 2$ kpc (Kunder & Chaboyer, 2009), the line of sight velocity $v_r = 140 \pm 2$ km s^{-1} (Ibata et al., 1997) and the proper motions $(\mu_l \cos b, \mu_b) = (-2.4 \pm 0.2, 2.1 \pm 0.2)$ mas yr^{-1} (Dinescu et al., 2005). Orbits are integrated forward and backward in time for 2 Gyr, to generate the set of observables associated with the known parts of the leading and trailing arm, respectively.

We probe each integrated orbit at 10 randomly selected times, in the interval of ± 1 Gyr, which corresponds to the time that takes to give rise to one full stream wrap on the sky. The full 6D coordinates at each point are transformed into the set of observables often used to represent the stream: position in the sky $(\Lambda_\odot, B_\odot)$ following (Majewski et al., 2003), heliocentric distance d, line of sight velocity in the Galactic standard of rest coordinate system $v_{\rm gsr}$, and proper motions in the Galactic coordinate system $(\mu_b, \mu_l \cos b)$.

Since we generate 5×10^4 initial conditions for the orbit integration, our sampling procedure leads to 5×10^5 points in the observable quantities, which are then assigned to a grid using the Cloud in Cell algorithm (Hockney & Eastwood, 1988). Fig. 5.4 shows the projected density for different observables as a function of the angular coordinate $\Lambda_\odot$. For example, in the top left panel we show the density associated with the line of sight velocity $v_{\rm gsr}$ along the leading arm. The algorithm to reconstruct the density yields a function of the form $P(\Lambda_\odot, v_{\rm gsr})$. We marginalize this quantity over $v_{\rm gsr}$ at each $\Lambda_\odot$, $P(v_{\rm gsr}|\Lambda_\odot) = \int dv_{\rm gsr} P(v_{\rm gsr}, \Lambda_\odot)$. The solid black line shows the median of this new quantity as a function of $\Lambda_\odot$, and with gray bands we represent the 1 and 2σ equivalent scatter around this median.

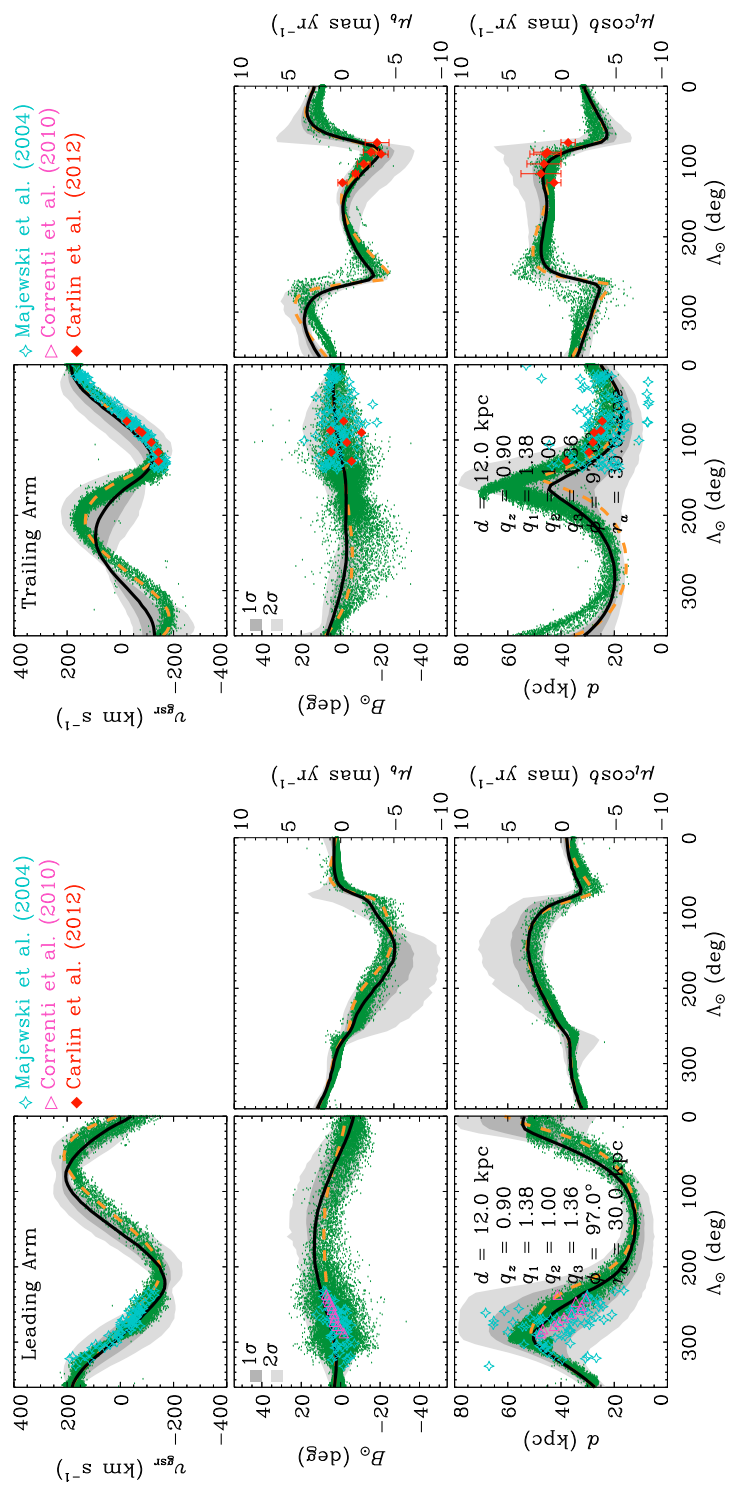

Figure 5.4: Radial velocity $v_{\rm gsr}$, position in the sky $B_\odot$, heliocentric distance d and proper motions $\mu_l \cos b, \mu_b$ as a function of the angular distance along the stream $\Lambda_\odot$ for the leading arm (left) and trailing arm (right). The potential used is the same described in Fig. 5.1 in which the halo makes a transition from oblate to triaxial at $r_a = 30$ kpc. The solid black line is the median orbit and the shaded regions represent 1σ and 2σ equivalent dispersion. The green dots are extracted from the N-body of Law & Majewski, and the center of mass orbit is given by the orange dashed curve.

In Fig. 5.4 we have included also the mean orbit in the triaxial model proposed by Law & Majewski (2010) (orange dashed line), and their N-body model (green dots). Additionally, we compare our results with the measurements of Majewski et al. (2004) (cyan stars), Correnti et al. (2010) (green triangles) and Carlin et al. (2012) (red diamonds).

Interestingly, both the radial velocities $v_{\rm gsr}$ and the positions on the sky $B_\odot$ are well reproduced by our model, showing that it is possible to find a halo potential that takes into account the effect of a baryonic disk and that also fits the orbit of the Sgr stream. The largest differences between this model and the purely triaxial by Law & Majewski (2010) are found in the leading stream at $0^\circ < \Lambda_\odot \lesssim 200^\circ$ (especially distances and radial velocities at a $\pm 25\%$ level) and in the trailing stream for $100^\circ \lesssim \Lambda_\odot \lesssim 300^\circ$ in the distances and $150^\circ \lesssim \Lambda_\odot \lesssim 360^\circ$ in the line of sight velocities.

The differences are not very large, and so it may be worthwhile to confirm our model with N-body simulations, or the technique proposed by Varghese, Ibata & Lewis (2011) to account for the energy offset between stream stars and the center of mass of the system. For instance, a comparison between the green dots (from the N-body) and the dashed orange curve (representing the trajectory of the center of mass) shows that the heliocentric distances d are somewhat offset in the case of the leading arm, and that the radial velocities also deviate at $\Lambda_\odot \lesssim 100^\circ$. On the other hand, for the trailing arm the orbit of the center of mass systematically underestimates the distances of the particles in the full simulation.

In test runs we found that the dependence of plausible orbits on the halo parameter r_a is not strong, whenever this is kept within reasonable values. Of course, a value of $r_a \gg r_{\rm apo}$ will lead to potential that is purely oblate in the region probed by the stream, and therefore will not be able to fit the line of sight velocities of the leading arm. The dependence of the stream orbits on the flattening parameter, q_z, is shown in Fig. 5.5. We explore here four different values of $q_z = \{0.7, 0.8, 0.9, 1.1\}$ keeping $r_a = 30$ kpc. For $q_z < 1$ the effect of changing this parameter is not very strong for $\Lambda_\odot \gtrsim 200^\circ$ for all observables. However, there are significant differences for $\Lambda_\odot \lesssim 300^\circ$ especially in the radial velocities. Note that $q_z < 0.9$ are disfavored by the available measurements of the line of sight velocities.

Prolate halo mass distributions close to the center affect more the tilt of the orbit and do not significantly improve the fit to the velocities compared to the $q_z = 0.9$ case. We find that in general $0.90 < q_z < 0.95$ yield a good fit to the observables in the leading arm. The trailing arm is not shown here as we find that it is rather insensitive to these changes in the region where observations are available, namely for $120^\circ \gtrsim \Lambda_\odot > 0^\circ$.

In this section we have taken a pragmatic approach since our goal was to show that it is possible to find a halo potential that reproduces the dynamics of the Sgr stream, while at the same time being consistent with the predictions of

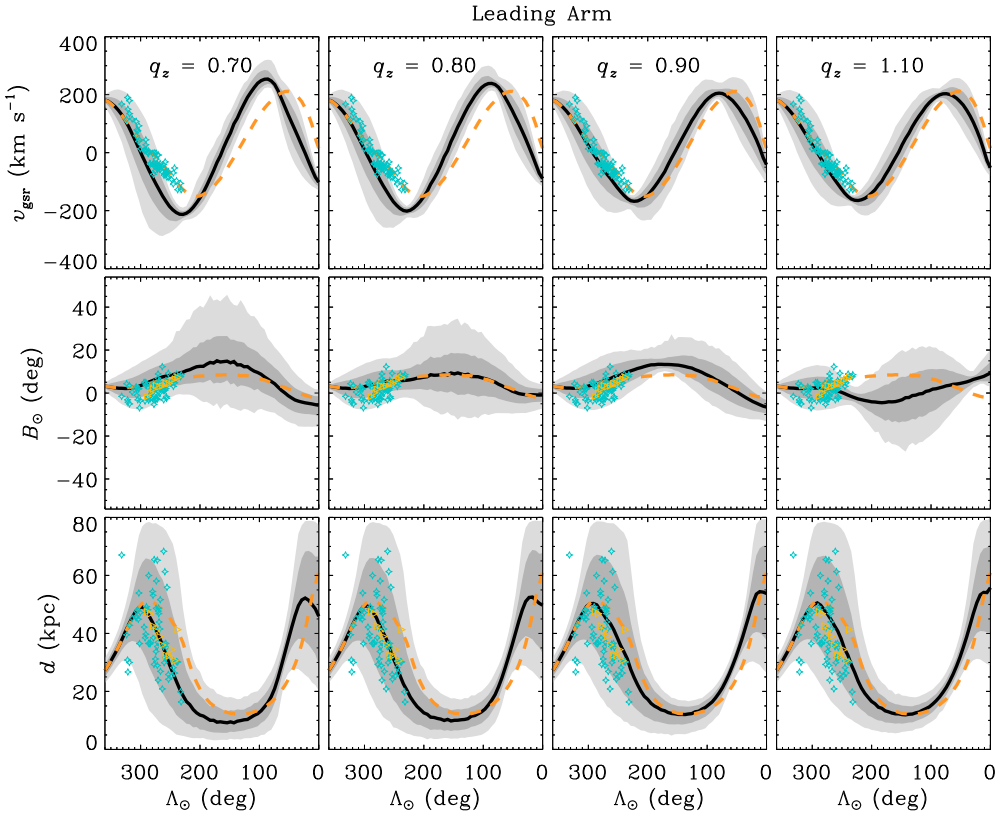

Figure 5.5: Line of sight velocities (top), position on the sky (middle) and heliocentric distances (bottom) for the leading arm and for four different values of q_z while keeping $r_a = 30$ kpc. The dashed orange line is the orbit of the center of mass from Law & Majewski.

galaxy formation models. To establish the best fit parameters of this potential would require e.g. a MCMC approach, as in Deg & Widrow (2012), which is however, beyond the scope of this Chapter.

5.3 Outer halo: The effect of LMC

In the previous section we showed that the mass distribution of the inner dark halo could be made consistent with the expectation that it should be flattened towards the Galactic disk. The outer halo on the other hand seems to be too flattened to reconcile it with the predictions of ΛCDM simulations (Allgood et al., 2006). For instance the typical minor-to-major axis ratio for $M_{\rm vir} = 10^{12}$ M$_\odot$ is $\langle c/a \rangle = 0.9 \pm 0.1$ (Hayashi, Navarro & Springel, 2007), compared with $(c/a) = 0.72$ for the triaxial model of Law & Majewski (2010).

It is very suggestive from Fig. 5.2 that the direction along which Law & Majewski's potential is elongated, approximately lies in the direction of the

Large Magellanic Cloud (LMC). It appears plausible that this elongation is a consequence of the presence of the LMC, given its significant mass $\sim 10^{11}$ $M_\odot$ (Besla et al., 2007). We explore this possibility below and proceed to model the effect of a perturbation like the LMC on the dynamics of the Sgr stream.

Note that since $\phi \approx 90°$, the principal axes of the potential of the halo at $r \gg r_a$ are nearly aligned with the Galactocentric coordinate system introduced in the previous section. Consequently, we can simplify Eq. (5.6) with

$$\widetilde{r}^2 \approx x^2 + \frac{y^2}{q_1^2} + \frac{z^2}{q_3^2} \qquad \text{for } r \gg r_a. \tag{5.9}$$

The torque that this halo potential exerts on the (approximate) plane of motion of the Sgr dwarf is simply $\boldsymbol{\tau} = -\boldsymbol{r} \times \partial\Phi_{\rm halo}/\partial\boldsymbol{r}$. Of the three components of this field, the x and z components are controlled by gradient of the force along the y direction, which is that of the strongest elongation in the Law & Majewski's halo ($q_1 = 1.38$). For instance the z component of the torque induced by this halo is

$$\begin{aligned} \tau_z^{\rm halo} &= -\frac{\partial\Phi_{\rm halo}}{\partial\widetilde{r}}\frac{xy}{\widetilde{r}}\left(\frac{1}{q_1^2}-1\right) \approx -\frac{v_{\rm circ}^2}{\widetilde{r}^2}xy\left(\frac{1}{q_1^2}-1\right) \\ &\approx -\frac{GM_{\rm halo}(\widetilde{r})}{\widetilde{r}^3}xy\left(\frac{1}{q_1^2}-1\right). \end{aligned} \tag{5.10}$$

Let us now consider the torque induced by the LMC. In our reference system the present day position of the LMC is nearly on the plane $x = 0$ (see Fig. 5.2). The force generated at $\boldsymbol{r} = x\boldsymbol{i} + y\boldsymbol{j} + z\boldsymbol{k}$ by a point mass $M_{\rm LMC}$ at the position of the LMC, $\boldsymbol{r}_{\rm LMC}$, is

$$\boldsymbol{F}_{\rm LMC} = -GM_{\rm LMC}\frac{\boldsymbol{r}-\boldsymbol{r}_{\rm LMC}}{|\boldsymbol{r}-\boldsymbol{r}_{\rm LMC}|^3}, \tag{5.11}$$

that generates a torque on the plane of motion of Sgr,

$$\boldsymbol{\tau}^{\rm LMC} = \boldsymbol{r} \times \boldsymbol{F}_{\rm LMC}, \tag{5.12}$$

and whose z component is,

$$\tau_z^{\rm LMC} = -\frac{GM_{\rm LMC}}{|\boldsymbol{r}-\boldsymbol{r}_{\rm LMC}|^3}(yx_{\rm LMC} - xy_{\rm LMC}) \approx \frac{GM_{\rm LMC}xy_{\rm LMC}}{|\boldsymbol{r}-\boldsymbol{r}_{\rm LMC}|^3}. \tag{5.13}$$

With the results of Eq. (5.10) and Eq. (5.13) we can quantify the importance that the triaxial halo has on the tilt of the orbit of Sgr, relative to the effect of the LMC,

$$\frac{\tau_z^{\rm LMC}}{\tau_z^{\rm halo}} \sim \frac{M_{\rm LMC}}{M_{\rm halo}(\widetilde{r})}\frac{\widetilde{r}^3}{r_{\rm sgr/LMC}^3}\frac{y_{\rm LMC}}{y}\frac{1}{1/q_1^2-1}. \tag{5.14}$$

In our model the mass of the halo enclosed within the Sgr orbit is $M_{\rm halo} \sim 3 \times 10^{11}$ M$_\odot$ which is not very different from $M_{\rm LMC} \sim 10^{11}$ M$_\odot$ (Besla et al., 2007). At the present day, the distance to Sgr and between Sgr and the LMC are comparable (15 vs $\sim$ 40 kpc), and since $y_{\rm LMC} \gg y$, the numerical value of this expression is of order unity. Additionally, since $q_1 > 1$ the torque generated by the LMC points in the same direction of the one produced by the triaxial halo ($y_{\rm LMC} < 0$, c.f. Fig. 5.2). This means that the torque generated by the LMC is as important as the one generated by the triaxial halo of Law & Majewski, at the position of Sgr. This implies that the elongation along the y-direction in the triaxial model could effectively be decreased if the LMC would be considered as well in the orbital integrations.

To implement the contribution of the LMC to the total potential in the integration of the Sgr stream orbits we proceed as follows. We integrate backward and forward in time the orbit of the LMC, starting from measurements of its current position $(\alpha, \delta) = (5^{\rm h}, 27.^{\rm m}6, -69^\circ, 52.2')$ (Piatek, Pryor & Olszewski, 2008), heliocentric distance $d = 50.1$ kpc (Freedman et al., 2001), radial velocity 278 km s^{-1} (van der Marel et al., 2002) and proper motions $(\mu_l \cos b, \mu_b) = (1.96, 0.44)$ mas yr^{-1} (Piatek, Pryor & Olszewski, 2008). We then place a Hernquist spheroid of mass $M_{\rm LMC,0} = 8 \times 10^{10}$ M$_\odot$ and scale radius $r_{\rm LMC,0} = 2$ kpc on this orbit. The Sgr orbit is then integrated in the presence of this new additional perturbation.

Fig. 5.6 show the results obtained for a model that includes the LMC, and where the flattening of the dark halo potential along its principal axes has been changed to: $q_1 = 1.1$, $q_2 = 1.0$ and $q_3 = 1.25$. The orientation of this potential is kept the same as before, with $\phi = 97^\circ$. The model of Law & Majewski (2010) is shown for comparison with the dashed orange line. It is interesting to note that after including the LMC, the orbital tilt of the leading arm is well fit in our model, despite the quite significant change we have introduced to the axis ratios of the dark halo. The torque of the orbital plane is, of course, also felt by the trailing arm and compared to the Law & Majewski (2010) model this results in different location of this stream on the sky $(B_\odot, \Lambda_\odot)$ for $\Lambda \lesssim 100^\circ$, which is a region not yet probed by observations.

The analysis of this section therefore shows that perturbations on the potential, such as the one generated by the LMC, have a non-negligible effect on the orbit of the Sgr stream. In a more realistic scenario including dynamical friction, the LMC might have been even more massive than at the present day, and as a consequence, its role in shaping the orbit of Sgr even is more dramatic. However, the LMC may be on its first infall and its effect would be negligible on the dynamics of streams formed more than 2-3 Gyr ago. This is clearly visible from Fig. 5.7, where we show the relative distance between the LMC and Sgr. The present day position ($t = 0$ Gyr in this plot) is actually the time of the closest encounter between these two objects where $d_{\rm sgr/LMC} \approx 37$ kpc.

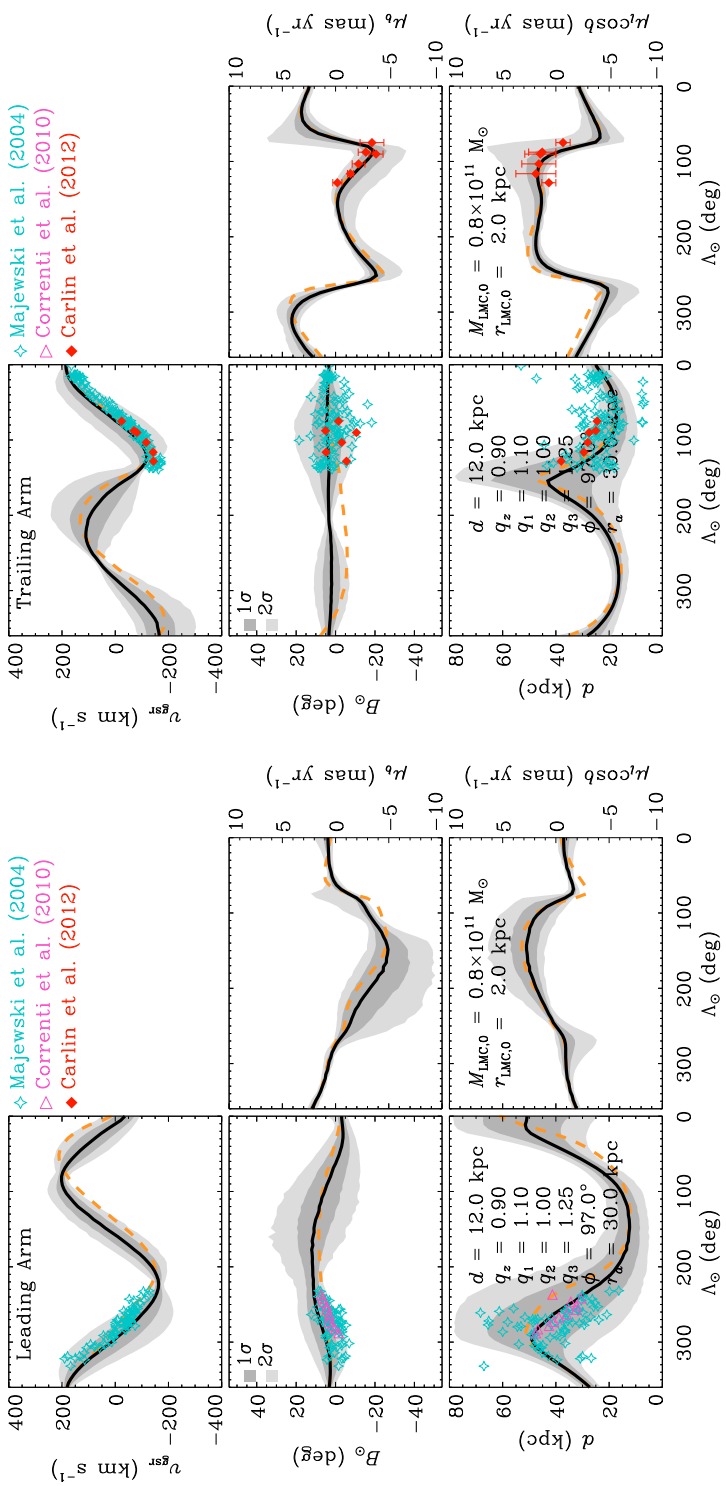

Figure 5.6: Radial velocity $v_{\rm gsr}$, position on the sky $B_\odot$, heliocentric distance d and proper motions $\mu_l \cos b, \mu_b$ as a function of the angular distance along the stream $\Lambda_\odot$ for the leading arm (left) and trailing arm (right). The potential used is similar to that described in Fig. 5.1 in which the halo transits from oblate to triaxial at $r_a = 30$ kpc and includes the potential of the LMC. The axis ratios of this halo potential are more in accordance with ΛCDM.

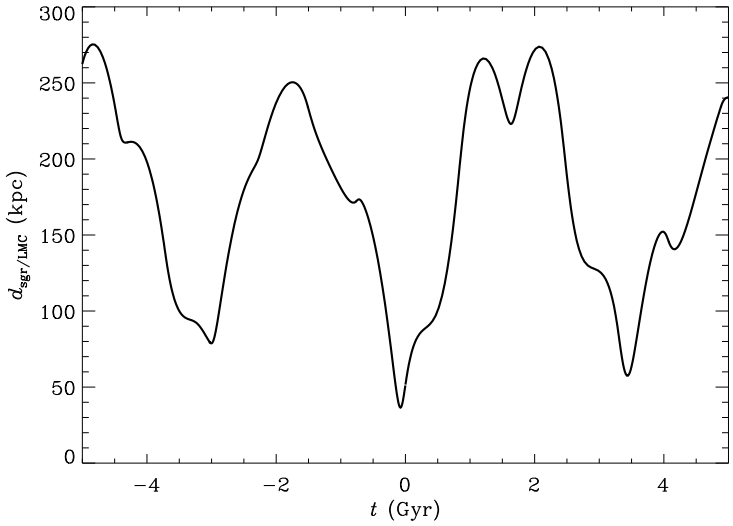

Figure 5.7: Relative distance between Sgr and the LMC as a function of time for a typical orbit integrated in the potential described in Section 5.3 (the same of Fig. 5.6). The present day corresponds to $t = 0$ Gyr.

It is important to stress that the model presented in this section, including the effect of the LMC, is by no means a unique solution, nor the most likely one. A thorough search of the parameter space for this case is required if we are to make stronger predictions. Nevertheless, the arguments shown here strongly suggest that the effect of the LMC cannot be neglected and that it should be taken into account if one wants to properly model the dynamics of the Sgr stream.

With this caveat in mind, we nonetheless show in Fig. 5.8 predictions for the observables associated to the first (solid line) and second (dashed line) wraps of the leading (left) and trailing (right) streams. With different colors we show the three different models of the potential discussed so far. Black is our fiducial model discussed in Section 5.2, green is the model that includes the LMC and red is the triaxial model of Law & Majewski (2010). We have also included here observations of different stellar tracers of the Sgr streams: RR Lyraes (Ivezić et al., 2000; Vivas, Zinn & Gallart, 2005; Prior, Da Costa & Keller, 2009), Carbon Giants (Ibata et al., 2001), Red Clump Giants (Dohm-Palmer et al., 2001; Starkenburg et al., 2009; Correnti et al., 2010), M Giants (Majewski et al., 2004) and Red Horizontal Branch stars (Shi et al., 2012). It is important to stress that Shi et al. preselected stars according to the triaxial model of Law & Majewski (2010), and so constraints obtained from this dataset may be biased.

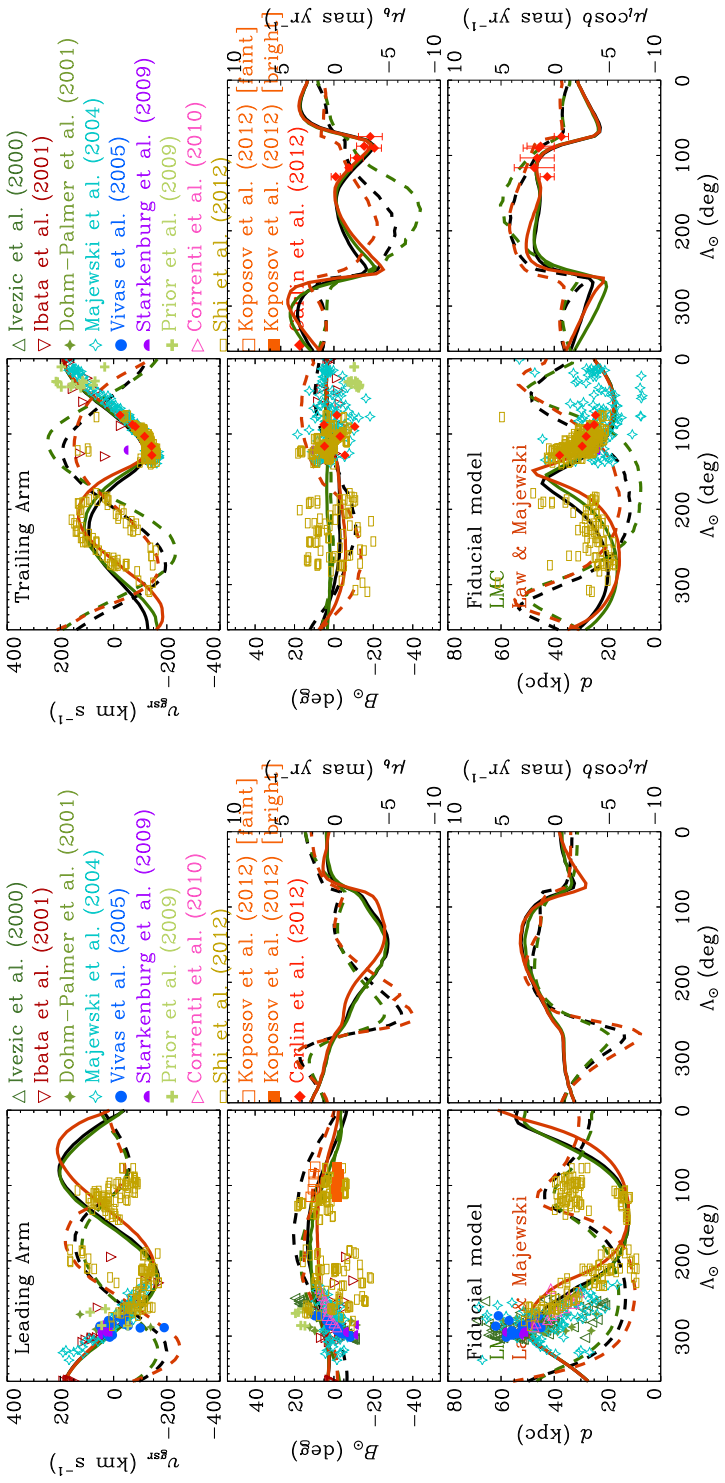

Figure 5.8: First (solid line) and second (dashed line) wraps of the leading (left) and trialing (right) arms of the Sgr stream. With black we show the fiducial model discusses in Section 5.2. Green shows the model including the LMC, and the triaxial model is shown in red.

We also show the observations in Southern Galactic hemisphere reported by Koposov et al. (2012) for the extension of the bifurcation of the leading stream. We have plotted the positions on the sky for the bright (orange filled squares) and the faint (orange open squares) stream in the left panels of Fig. 5.8 at $75^\circ < \Lambda_\odot < 115^\circ$.

Fig. 5.8 shows that several features could be used to constrain and differentiate the models. For instance the predictions for the line of sight velocities and heliocentric distances of the leading arm in the first wrap for $200^\circ \gtrsim \Lambda_\odot > 0^\circ$ exhibit differences larger that the expected observational uncertainties. Therefore, more detailed studies in the Southern Galactic hemisphere will likely help to better constrain our current knowledge of the properties of the MW dark matter halo.

5.4 Conclusions

In this Chapter we have presented an alternative model that fits the observations of the Sagittarius stream and that is consistent with current predictions of galaxy formation theories. Our model for the potential of the Milky Way's dark matter halo is axisymmetric and flattened towards the disk plane for $R \lesssim 10$ kpc, and asymptotically approaches the triaxial model presented by Law & Majewski (2010) at larger radii. With a flattening of $q_z = 0.9$ in the halo potential at small radii, we are able to successfully reproduce both the observed line of sight velocities and the tilt in the orbit of the leading arm. A gratifying property of this potential is that its oblate shape close to the center accounts for the effect of the formation of the Galactic disk and ensures its stability.

The triaxial part of this potential, however is still not entirely consistent with the expectations of the ΛCDM model. The odd configuration of the outer halo of Law & Majewski (2010) can be changed, and brought to a more reasonable shape, if the gravitational field generated by the Large Magellanic Cloud is taken into account. The integration of orbits in a composite potential including the LMC and an outer triaxial halo with $q_1 = 1.10$, $q_2 = 1.00$ and $q_3 = 1.25$ (that is as before, oblate in the inner regions), is also found to reproduce well the properties of the Sgr streams in the region where these have been constrained observationally.

We also show how observations in the Southern Galactic hemisphere can be used to break degeneracies in the model, and in particular to assess the relative importance of the LMC on the dynamics of the Sgr streams. This would help also to understand whether the Magellanic system is in first infall or has been a member of the MW for a longer time.

The conclusions drawn in this work are based on heuristic searches of the high-dimensional parameter space that characterizes the gravitational potential of the Milky Way. By no means do they represent best fit models in a

statistical sense. Therefore, the predictions made cannot be considered exclusive or definitive, but serve to guide where future observations could focus to distinguish between various models. Notwithstanding these caveats, we have been able to demonstrate in this Chapter that the dynamics of the Sgr streams can be understood in a context that is consistent with expectations from the ΛCDM cosmological model.

Acknowledgments

We are very grateful to Shoko Jin in relation to some of the datasets used in this work, and to Laura V. Sales for her critical input in the preparation of this Chapter. AH gratefully acknowledges financial support from the European Research Council under ERC-Starting Grant GALACTICA-240271.

Bibliography

Abadi M. G. et al., 2010, MNRAS, 407, 435

Abramowitz M., Stegun I. A., 1972, Handbook of Mathematical Functions. Dover Publications

Allgood B. et al., 2006, MNRAS, 367, 1781

Altay G., Colberg J. M., Croft R. A. C., 2006, MNRAS, 370, 1422

Amorisco N. C., Evans N. W., 2011, MNRAS, 411, 2118

Amorisco N. C., Evans N. W., 2012, MNRAS, 419, 184

Angulo R. E. et al., 2012, MNRAS, 425, 2722

Aragón-Calvo M. A. et al., 2007a, A&A, 474, 315

Aragón-Calvo M. A. et al., 2007b, ApJ, 655, L5

Aubert D., Pichon C., 2007, MNRAS, 374, 877

Aubert D., Pichon C., Colombi S., 2004, MNRAS, 352, 376

Avila-Reese V. et al., 2005, ApJ, 634, 51

Avila-Reese V. et al., 2001, ApJ, 559, 516

Bahcall J. N., Serenelli A. M., Basu S., 2005, ApJ, 621, L85

Bailin J. et al., 2005, ApJ, 627, L17

Bailin J. et al., 2008, MNRAS, 390, 1133

Bailin J., Steinmetz M., 2005, ApJ, 627, 647

Banerjee A., Jog C. J., 2011, ApJ, 732, L8+

Barnabè M. et al., 2011, MNRAS, 415, 2215

Basilakos S. et al., 2006, MNRAS, 365, 539

Battaglia G. et al., 2005, MNRAS, 364, 433

Battaglia G. et al., 2006, MNRAS, 370, 1055

Battaglia G. et al., 2008, ApJ, 681, L13

Becquaert J., Combes F., 1997, A&A, 325, 41

Belokurov V. et al., 2006, ApJ, 642, L137

Benson A. J. et al., 2012, MNRAS, 142

Benson A. J. et al., 2002, MNRAS, 333, 177

Bertschinger E., 1985, ApJS, 58, 39

Besla G. et al., 2007, ApJ, 668, 949

Betancort-Rijo J. E., Trujillo I., 2009, preprint (ArXiv:0912.1051)

Bett P. et al., 2007, MNRAS, 376, 215

Bett P. et al., 2010, MNRAS, 404, 1137

Binggeli B., 1982, A&A, 107, 338

Binney J., 2005, MNRAS, 363, 937

Binney J., Mamon G. A., 1982, MNRAS, 200, 361

Binney J., Tremaine S., 2008, Galactic Dynamics: Second Edition. Princeton University Press

Blumenthal G. R. et al., 1984, Nature, 311, 517

Bonaca A., Geha M., Kallivayalil N., 2012, ApJ, 760, L6

Bond J. R. et al., 1991, ApJ, 379, 440

Bosma A., 1981a, AJ, 86, 1791

Bosma A., 1981b, AJ, 86, 1825

Boylan-Kolchin M., Bullock J. S., Kaplinghat M., 2011, MNRAS, 415, L40

Boylan-Kolchin M., Bullock J. S., Kaplinghat M., 2012a, MNRAS, 422, 1203

Boylan-Kolchin M., Bullock J. S., Kaplinghat M., 2012b, MNRAS, 2657

Boylan-Kolchin M. et al., 2010, MNRAS, 406, 896

Brainerd T. G., 2005, ApJ, 628, L101

Breddels M. A. et al., 2012a, arXiv:1205.4721

Breddels M. A. et al., 2012b, Assembling the Puzzle of the Milky Way, Le Grand-Bornand, France, Edited by C. Reylé; A. Robin; M. Schultheis; EPJ Web of Conferences, Volume 19, id.03009, 19, 3009

Bryan S. E. et al., 2012, arXiv: 1207.4555

Bullock J. S., 2002, in The Shapes of Galaxies and their Dark Halos, P. Natarajan, ed., pp. 109–113

Bullock J. S., Kravtsov A. V., Weinberg D. H., 2000, ApJ, 539, 517

Buote D. A., Canizares C. R., 1998, MNRAS, 298, 811

Buote D. A., Humphrey P. J., 2012, MNRAS, 421, 1399

Buote D. A. et al., 2002, ApJ, 577, 183

Busha M. T. et al., 2011a, ApJ, 743, 40

Busha M. T. et al., 2011b, ApJ, 743, 117

Carlin J. L. et al., 2012, ApJ, 744, 25

Carr B. J., Rees M. J., 1984, MNRAS, 206, 801

Carroll S. M., Press W. H., Turner E. L., 1992, ARA&A, 30, 499

Choi J.-H., Weinberg M. D., Katz N., 2007, MNRAS, 381, 987

Colberg J. M. et al., 1999, MNRAS, 308, 593

Cole S., Lacey C., 1996, MNRAS, 281, 716

Cooper A. P. et al., 2010, MNRAS, 406, 744

Corbelli E., 2003, MNRAS, 342, 199

Correnti M. et al., 2010, ApJ, 721, 329

Couchman H. M. P., Rees M. J., 1986, MNRAS, 221, 53

Croton D. J. et al., 2006, MNRAS, 365, 11

Cuesta A. J. et al., 2008, MNRAS, 389, 385

Davis M. et al., 1985, ApJ, 292, 371

de Blok W. J. G., 2010, Advances in Astronomy, 2010

de Blok W. J. G. et al., 2001, ApJ, 552, L23

De Lucia G., Blaizot J., 2007, MNRAS, 375, 2

De Lucia G., Helmi A., 2008, MNRAS, 391, 14

De Lucia G., Kauffmann G., White S. D. M., 2004, MNRAS, 349, 1101

De Rijcke S. et al., 2006, MNRAS, 369, 1321

Debattista V. P. et al., 2008, ApJ, 681, 1076

DeBuhr J., Ma C.-P., White S. D. M., 2012, MNRAS, 426, 983

Deg N., Widrow L., 2012, MNRAS, 96

Dehnen W., McLaughlin D. E., 2005, MNRAS, 363, 1057

Di Cintio A. et al., 2012, arXiv: 1204.0515

Di Cintio A. et al., 2011, MNRAS, 417, L74

Diemand J., Kuhlen M., Madau P., 2007, ApJ, 657, 262

Diemand J. et al., 2008, Nature, 454, 735

Diemand J., Moore B., 2011, Adv. Sci. Lett., 4, 297

Dinescu D. I. et al., 2005, ApJ, 618, L25

Dohm-Palmer R. C. et al., 2001, ApJ, 555, L37

Dreyer J. L. E., 1888, Mem. R. Astron. Soc, 49, 1

Dubinski J., 1994, ApJ, 431, 617

Dubinski J., Carlberg R. G., 1991, ApJ, 378, 496

Efstathiou G., 1992, MNRAS, 256, 43P

Efstathiou G. et al., 1985, ApJS, 57, 241

Einasto J., 1965, Trudy Astrofiz. Inst. Alma-Ata, 5, 87

Eisenstein D. J., Loeb A., 1995, ApJ, 439, 520

Eyre A., Binney J., 2009, MNRAS, 400, 548

Faltenbacher A. et al., 2005, MNRAS, 362, 1099

Faltenbacher A. et al., 2008, ApJ, 675, 146

Faltenbacher A. et al., 2007, ApJ, 662, L71

Faltenbacher A. et al., 2009, Research in Astronomy and Astrophysics, 9, 41

Fardal M. A., PAndAS Collaboration, 2011, in American Astronomical Society Meeting Abstracts #218, p. 106.01

Fasano G. et al., 1993, MNRAS, 262, 109

Fellhauer M. et al., 2006, ApJ, 651, 167

Fillmore J. A., Goldreich P., 1984, ApJ, 281, 1

Flores R. A., Primack J. R., 1994, ApJ, 427, L1

Font A. S. et al., 2011, MNRAS, 417, 1260

Franx M., Illingworth G., de Zeeuw T., 1991, ApJ, 383, 112

Freedman W. L. et al., 2001, ApJ, 553, 47

Frenk C. S. et al., 1988, ApJ, 327, 507

Friedmann A., 1924, Zeitschrift fur Physik, 21, 326

Gao L. et al., 2008, MNRAS, 387, 536

Gao L. et al., 2012, MNRAS, 425, 2169

Gao L. et al., 2004, MNRAS, 355, 819

Gerhard O. E., 1983, MNRAS, 202, 1159

Ghigna S. et al., 1998, MNRAS, 300, 146

Gilmore G. et al., 2007, ApJ, 663, 948

Gnedin O. Y. et al., 2010, ApJ, 720, L108

Gnedin O. Y. et al., 2005, ApJ, 634, 344

Godłowski W., Flin P., 2010, ApJ, 708, 920

Gott, III J. R., Rees M. J., 1975, A&A, 45, 365

Gottlöber S., Turchaninov V., 2006, in EAS Publications Series, Vol. 20, EAS Publications Series, G. A. Mamon, F. Combes, C. Deffayet, & B. Fort, ed., pp. 25–28

Governato F. et al., 2012, MNRAS, 422, 1231

Graham A. W. et al., 2006, AJ, 132, 2701

Gunn J. E., Gott, III J. R., 1972, ApJ, 176, 1

Guo Q. et al., 2011, MNRAS, 413, 101

Guo Q. et al., 2010, MNRAS, 404, 1111

Gustafsson M., Fairbairn M., Sommer-Larsen J., 2006, Phys. Rev. D, 74, 123522

Hahn O. et al., 2007a, MNRAS, 381, 41

Hahn O. et al., 2007b, MNRAS, 375, 489

Hansen S. H., Moore B., 2006, New A., 11, 333

Hayashi E., Navarro J. F., 2006, MNRAS, 373, 1117

Hayashi E., Navarro J. F., Springel V., 2007, MNRAS, 377, 50

Hayashi E. et al., 2003, ApJ, 584, 541

Hayashi K., Chiba M., 2012, ApJ, 755, 145

Heiligman G., Schwarzschild M., 1979, ApJ, 233, 872

Helmi A., 2004, ApJ, 610, L97

Helmi A. et al., 2011, ApJ, 733, L7

Helmi A., White S. D., Springel V., 2002, Phys. Rev. D, 66, 063502

Helmi A., White S. D. M., Springel V., 2003, MNRAS, 339, 834

Hernquist L., 1990, ApJ, 356, 359

Hockney R. W., Eastwood J. W., 1988, Computer simulation using particles. Bristol: Hilger, 1988

Hoekstra H., Yee H. K. C., Gladders M. D., 2004, ApJ, 606, 67

Hopkins P. F., Bahcall N. A., Bode P., 2005, ApJ, 618, 1

Hubble E., 1929, Proceedings of the National Academy of Science, 15, 168

Ibata R. et al., 2001, ApJ, 551, 294

Ibata R. A. et al., 1997, AJ, 113, 634

Ivezić Ž. et al., 2000, AJ, 120, 963

Jardel J. R., Gebhardt K., 2012, ApJ, 746, 89

Jardel J. R. et al., 2011, ApJ, 739, 21

Jenkins A. et al., 2001, MNRAS, 321, 372

Jiang I.-G., Binney J., 2000, MNRAS, 314, 468

Jing Y. P., Suto Y., 2002, ApJ, 574, 538

Johnston K. V., Law D. R., Majewski S. R., 2005, ApJ, 619, 800

Johnston K. V., Spergel D. N., Haydn C., 2002, ApJ, 570, 656

Kalirai J. S. et al., 2010, ApJ, 711, 671

Kallivayalil N. et al., 2009, ApJ, 700, 924

Kamionkowski M., Koushiappas S. M., Kuhlen M., 2010, Phys. Rev. D, 81, 043532

Kang X. et al., 2007, MNRAS, 378, 1531

Karachentsev I. D. et al., 2004, AJ, 127, 2031

Kasun S. F., Evrard A. E., 2005, ApJ, 629, 781

Kauffmann G. et al., 1999, MNRAS, 303, 188

Kauffmann G., White S. D. M., 1993, MNRAS, 261, 921

Kauffmann G., White S. D. M., Guiderdoni B., 1993, MNRAS, 264, 201

Kazantzidis S., Abadi M. G., Navarro J. F., 2010, ApJ, 720, L62

Kazantzidis S. et al., 2004, ApJ, 611, L73

Kitzbichler M. G., Saurer W., 2003, ApJ, 590, L9

Kleyna J. T. et al., 2001, ApJ, 563, L115

Klypin A. et al., 1999a, ApJ, 516, 530

Klypin A. et al., 1999b, ApJ, 522, 82

Knebe A. et al., 2008a, MNRAS, 386, L52

Knebe A. et al., 2004, ApJ, 603, 7

Knebe A. et al., 2008b, MNRAS, 388, L34

Kochanek C. S., 1996, ApJ, 457, 228

Komatsu E. et al., 2011, ApJS, 192, 18

Koposov S. et al., 2008, ApJ, 686, 279

Koposov S. E. et al., 2012, ApJ, 750, 80

Koposov S. E., Rix H.-W., Hogg D. W., 2010, ApJ, 712, 260

Kravtsov A. V., Gnedin O. Y., Klypin A. A., 2004, ApJ, 609, 482

Kuhlen M., Diemand J., Madau P., 2007, ApJ, 671, 1135

Kuhlen M., Vogelsberger M., Angulo R., 2012, arXiv:1209.5745

Kunder A., Chaboyer B., 2009, AJ, 137, 4478

Lau E. T. et al., 2011, ApJ, 734, 93

Law D. R., Johnston K. V., Majewski S. R., 2005, ApJ, 619, 807

Law D. R., Majewski S. R., 2010, ApJ, 714, 229

Law D. R., Majewski S. R., Johnston K. V., 2009, ApJ, 703, L67

Lee J., Jing Y. P., Suto Y., 2005, ApJ, 632, 706

Lemson G., Kauffmann G., 1999, MNRAS, 302, 111

Li Y.-S., De Lucia G., Helmi A., 2010, MNRAS, 401, 2036

Li Y.-S., Helmi A., 2008, MNRAS, 385, 1365

Li Y.-S. et al., 2009, MNRAS, 397, L87

Li Y.-S., White S. D. M., 2008, MNRAS, 384, 1459

Libeskind N. I. et al., 2007, MNRAS, 374, 16

Libeskind N. I. et al., 2005, MNRAS, 363, 146

Libeskind N. I. et al., 2011, MNRAS, 411, 1525

Libeskind N. I. et al., 2010, MNRAS, 401, 1889

Liu L. et al., 2011, ApJ, 733, 62

Łokas E. L., 2002, MNRAS, 333, 697

Łokas E. L., 2009, MNRAS, 394, L102

Łokas E. L., Mamon G. A., Prada F., 2005, MNRAS, 363, 918

Long R. J., Mao S., 2010, MNRAS, 405, 301

Lovell M. R. et al., 2011a, MNRAS, 341

Lovell M. R. et al., 2011b, MNRAS, 413, 3013

Ludlow A. D. et al., 2010, MNRAS, 406, 137

Ludlow A. D. et al., 2011, MNRAS, 415, 3895

Macciò A. V. et al., 2007, MNRAS, 378, 55

Macciò A. V. et al., 2010, MNRAS, 402, 1995

Macciò A. V. et al., 2012, MNRAS, 424, 1105

Madau P., Diemand J., Kuhlen M., 2008, ApJ, 679, 1260

Magorrian J., Ballantyne D., 2001, MNRAS, 322, 702

Majewski S. R. et al., 2004, AJ, 128, 245

Majewski S. R. et al., 2003, ApJ, 599, 1082

Martínez-Delgado D. et al., 2010, AJ, 140, 962

Martínez-Delgado D. et al., 2004, ApJ, 601, 242

Mateo M. L., 1998, ARA&A, 36, 435

Merrifield M. R., Kent S. M., 1990, AJ, 99, 1548

Merritt D. et al., 2006, AJ, 132, 2685

Merritt D. et al., 2005, ApJ, 624, L85

Miyamoto M., Nagai R., 1975, PASJ, 27, 533

Mo H. J., Mao S., 2004, MNRAS, 353, 829

Moore B. et al., 1999, ApJ, 524, L19

Muñoz-Cuartas J. C. et al., 2011, MNRAS, 411, 584

Navarro J. F., Abadi M. G., Steinmetz M., 2004, ApJ, 613, L41

Navarro J. F., Eke V. R., Frenk C. S., 1996, MNRAS, 283, L72

Navarro J. F., Frenk C. S., White S. D. M., 1996, ApJ, 462, 563

Navarro J. F., Frenk C. S., White S. D. M., 1997, ApJ, 490, 493

Navarro J. F. et al., 2004, MNRAS, 349, 1039

Navarro J. F. et al., 2010, MNRAS, 402, 21

Neto A. F. et al., 2007, MNRAS, 381, 1450

Newman A. B. et al., 2012a, arXiv:1209.1392

Newman A. B. et al., 2012b, arXiv:1209.1391

Niederste-Ostholt M. et al., 2010, MNRAS, 405, 2023

Okamoto T., Frenk C. S., 2009, MNRAS, 399, L174

Olling R. P., 1996, AJ, 112, 481

Patiri S. G. et al., 2006, ApJ, 652, L75

Paz D. J. et al., 2011, MNRAS, 502

Pedrosa S., Tissera P. B., Scannapieco C., 2009, MNRAS, 395, L57

Peebles P. J. E., 1980, The large-scale structure of the universe. Princeton University Press

Pereira M. J., Bryan G. L., Gill S. P. D., 2008, ApJ, 672, 825

Perlmutter S. et al., 1999, ApJ, 517, 565

Piatek S., Pryor C., Olszewski E. W., 2008, AJ, 135, 1024

Pimbblet K. A., 2005, MNRAS, 358, 256

Pontzen A., Governato F., 2012, MNRAS, 421, 3464

Power C. et al., 2003, MNRAS, 338, 14

Prada F. et al., 2006, ApJ, 645, 1001

Press W. H., Schechter P., 1974, ApJ, 187, 425

Prior S. L., Da Costa G. S., Keller S. C., 2009, ApJ, 704, 1327

Quinn T., Binney J., 1992, MNRAS, 255, 729

Ragone-Figueroa C. et al., 2010, MNRAS, 407, 581

Read J. I., Gilmore G., 2005, MNRAS, 356, 107

Reed D. S., Koushiappas S. M., Gao L., 2011, MNRAS, 415, 3177

Richstone D. O., Tremaine S., 1986, AJ, 92, 72

Riess A. G. et al., 1998, AJ, 116, 1009

Rix H., 1996, in IAU Symposium, Vol. 169, Unsolved Problems of the Milky Way, L. Blitz & P. J. Teuben, ed., pp. 23–29

Roberts P. H., 1962, ApJ, 136, 1108

Robotham A., Phillipps S., De Propris R., 2008, ApJ, 672, 834

Rossi G., Sheth R. K., Tormen G., 2010, preprint (ArXiv:1010.2839)

Sackett P. D., 1999, in Astronomical Society of the Pacific Conference Series, Vol. 182, Galaxy Dynamics - A Rutgers Symposium, D. R. Merritt, M. Valluri, & J. A. Sellwood, ed., p. 393

Sakamoto T., Chiba M., Beers T. C., 2003, A&A, 397, 899

Sales L. V. et al., 2007, MNRAS, 382, 1901

Salvador-Solé E. et al., 2011, preprint (ArXiv:1104.3143)

Schaye J. et al., 2010, MNRAS, 402, 1536

Schneider M. D., Frenk C. S., Cole S., 2012, J. Cosmology Astropart. Phys., 5, 30

Sesar B., Juric M., Ivezic Z., 2011, in Bulletin of the American Astronomical Society, Vol. 43, American Astronomical Society Meeting Abstracts #217, p. 241.09

Sheth R. K., Tormen G., 1999, MNRAS, 308, 119

Shi W. B. et al., 2012, ApJ, 751, 130

Siebert A. et al., 2008, MNRAS, 391, 793

Smith M. C. et al., 2007, MNRAS, 379, 755

Smith R. W., 1982, The expanding universe: astronomy's "Great Debate" 1900 - 1931. Cambridge Univesity Press

Sofue Y., Rubin V., 2001, ARA&A, 39, 137

Somerville R. S., 2002, ApJ, 572, L23

Spergel D. N., Steinhardt P. J., 2000, Physical Review Letters, 84, 3760

Springel V. et al., 2008, MNRAS, 391, 1685

Springel V., White S. D. M., Hernquist L., 2004, in IAU Symposium, Vol. 220, Dark Matter in Galaxies, S. Ryder, D. Pisano, M. Walker, & K. Freeman, ed., p. 421

Springel V. et al., 2001, MNRAS, 328, 726

Stadel J. et al., 2009, MNRAS, 398, L21

Starkenburg E. et al., 2012, arXiv:1206.0020

Starkenburg E. et al., 2009, ApJ, 698, 567

Stoehr F. et al., 2003, MNRAS, 345, 1313

Stoehr F. et al., 2002, MNRAS, 335, L84

Stoica R. S. et al., 2005, A&A, 434, 423

Strigari L. E., 2012, arXiv:1211.7090

Strigari L. E. et al., 2008, Nature, 454, 1096

Strigari L. E., Frenk C. S., White S. D. M., 2010, MNRAS, 408, 2364

Strigari L. E., Kaplinghat M., Bullock J. S., 2007, Phys. Rev. D, 75, 061303

Stringer M., Cole S., Frenk C. S., 2010, MNRAS, 404, 1129

Swaters R. A., Sancisi R., van der Hulst J. M., 1997, ApJ, 491, 140

Taylor J. E., Navarro J. F., 2001, ApJ, 563, 483

Thomas P. A. et al., 1998, MNRAS, 296, 1061

Thoul A. A., Weinberg D. H., 1996, ApJ, 465, 608

Tissera P. B. et al., 2010, MNRAS, 406, 922

Tonini C., Lapi A., Salucci P., 2006, ApJ, 649, 591

Tormen G., 1997, MNRAS, 290, 411

Tormen G., Diaferio A., Syer D., 1998, MNRAS, 299, 728

Toth G., Ostriker J. P., 1992, ApJ, 389, 5

Valluri M. et al., 2010, MNRAS, 403, 525

van der Marel R. P. et al., 2002, AJ, 124, 2639

van Uitert E. et al., 2012, A&A, 545, A71

Varghese A., Ibata R., Lewis G. F., 2011, MNRAS, 417, 198

Vera-Ciro C. A. et al., 2012, arXiv:1202.6061

Vera-Ciro C. A. et al., 2011, MNRAS, 416, 1377

Viel M. et al., 2008, Physical Review Letters, 100, 041304

Vivas A. K., Zinn R., Gallart C., 2005, AJ, 129, 189

Vogelsberger M., White S. D. M., 2011, MNRAS, 413, 1419

Vogelsberger M. et al., 2008, MNRAS, 385, 236

Vogelsberger M. et al., 2009, MNRAS, 400, 2174

Vogelsberger M., Zavala J., Loeb A., 2012, MNRAS, 423, 3740

Walker M. G., 2012, arXiv:1205.0311

Walker M. G. et al., 2009, ApJ, 704, 1274

Walker M. G., Peñarrubia J., 2011, ApJ, 742, 20

Wang J. et al., 2012, MNRAS, 424, 2715

Wang J., White S. D. M., 2009, MNRAS, 396, 709

Wang Y.-G., Fan Z.-H., 2006, ApJ, 643, 630

Warnick K., Knebe A., Power C., 2008, MNRAS, 385, 1859

Warren M. S. et al., 1992, ApJ, 399, 405

Watkins L. L., Evans N. W., An J. H., 2010, MNRAS, 406, 264

White S. D. M., Davis M., Frenk C. S., 1984, MNRAS, 209, 27P

White S. D. M., Rees M. J., 1978, MNRAS, 183, 341

Wilcots E. M., Miller B. W., 1998, AJ, 116, 2363

Wilkinson M. I., Evans N. W., 1999, MNRAS, 310, 645

Wilkinson M. I. et al., 2002, MNRAS, 330, 778

Wojtak R. et al., 2005, MNRAS, 361, L1

Wolf J. et al., 2010, MNRAS, 406, 1220

Xue X. X. et al., 2008, ApJ, 684, 1143

Yang X. et al., 2006, MNRAS, 369, 1293

Yoon J. H., Johnston K. V., Hogg D. W., 2011, ApJ, 731, 58

Yoshida N. et al., 2000, ApJ, 544, L87

Zavala J., Springel V., Boylan-Kolchin M., 2010, MNRAS, 405, 593

Zhang Y. et al., 2009, ApJ, 706, 747

Zhao H., 1998, ApJ, 500, L149

Zolotov A. et al., 2012, arXiv:1207.0007

Zwicky F., 1937, ApJ, 86, 217

Summary

The journey that began by simply counting stars on the skies millennia ago has led to one of the most controversial open questions of contemporary science: "What is the Universe made of?". Finding a satisfactory answer has been particularly difficult, despite numerous and diverse attempts. Astrophysics has not been idle at all in this enterprise, since the last century was particularly fruitful in developing a physical picture of the formation and evolution of the universe as a whole and also of its individual components, such as planets, stars and galaxies.

By measuring the speeds of stars in distant galaxies, for instance, we have concluded that there is significantly more matter than what meets the eye. Stars move because of the total gravitational pull of the galaxy they live in. This pull depends on mass, and therefore if the masses of all stars are known to some extent (from their brightness for example), their velocities could tell us if our understanding of Newton's Laws is correct, a physical theory known since the XVII century. Large discrepancies were found when such measurements were made, which led to the conclusion that either these laws are fundamentally wrong, or that the galaxies have some hidden mass. In this Thesis we worked under the second hypothesis, and call the missing component *dark matter*, emphasizing the fact that it is matter that is not directly visible. The mismatch in the dynamics of stars in galaxies suggests that dark matter is the most dominant component of these systems, and that stars have only a negligible contribution to the overall mass budget. Models and observations suggest that the dark matter is distributed in a spheroid surrounding the visible galaxy, and we will refer to this as a *halo*.

Spectacular explosions of stars at the end of their lives in distant galaxies also have allowed us to draw another important conclusion about the composition of the universe. Besides dark matter, there is a force that makes galaxies move in an accelerated fashion away from each other. Because the nature of this force is unknown to mankind, with the exception perhaps of vacuum itself, a new component had to be added to the picture. This new component has been termed *dark energy* and has been estimated to account for approximately 3/4 of the matter/energy content of the Universe at the present day, with the remaining mostly 1/4 being dark matter.

Unfortunately, only educated guesses are available for the nature of either dark matter or dark energy. Several experiments are currently being carried out aiming to understand these and place them within a consistent physical model of the Universe. However this task has proven to be rather difficult, and the results so far are disappointingly inconclusive.

The ΛCDM model constitutes a particular, currently favored by observations, description of the Universe, which includes both dark components. In this model galaxies form and evolve through time by mergers of smaller systems. The gravitational pull generated by the dark matter halo of a massive galaxy attracts nearby objects making them collide and, with time, completely merge to produce a new more massive galaxy. Although this process is intuitively well understood, the equations to model it become effectively intractable once the number of objects involved in the process starts to grow. Thus the use to computational tools is not only required, but sometimes the only way to study the formation and evolution of galaxies.

In this Thesis we extensively use numerical experiments based on N bodies, where the dark matter component of galaxies is represented by point masses, and the equations predicting the positions and velocities are numerically solved with powerful computers. State of the art simulations of this kind include several billions of such bodies and are capable of model, with unprecedented detail, the formation and evolution of dark matter halos such as that surrounding the Milky Way, keeping track of all the process that led to their present day configuration.

Fig. 1 is a snapshot view of the present day distribution of dark matter around a simulated system that is expected to have the mass of the Milky Way. The smooth component, whose center defines the center of the picture, shows that the shape of the dark matter of the halo surrounding the Milky Way is expected to be far from spherical in the ΛCDM model. In fact, in Chapter 2 of this Thesis it is shown that it is better described by an ellipsoid whose axis ratios change as a function of distance from the center of the halo. In general at a distance comparable to that of the Sun to the Galactic center, the halo is described by a distribution of mass that partially resembles an american football, and which becomes progressively less axisymmetric as we move outwards. The shapes of the dark halos result as a response to the configuration of the surrounding nearest portions of the universe, and directly correlate with the way in which the mass assembly takes place. These conclusions however may be affected if other physical effects are taken into account. For instance, the interplay of visible and dark matter plays an important role in shaping the halo close to its center, generating figures that resemble closely a nut-less M&M$^{\text{TM}}$.

Perhaps the most striking impression after looking at Fig. 1 is the large amount of small structures embedding the halo. These are dark objects of their own (*subhalos*), currently merging with the main halo. In Chapter 3 we show

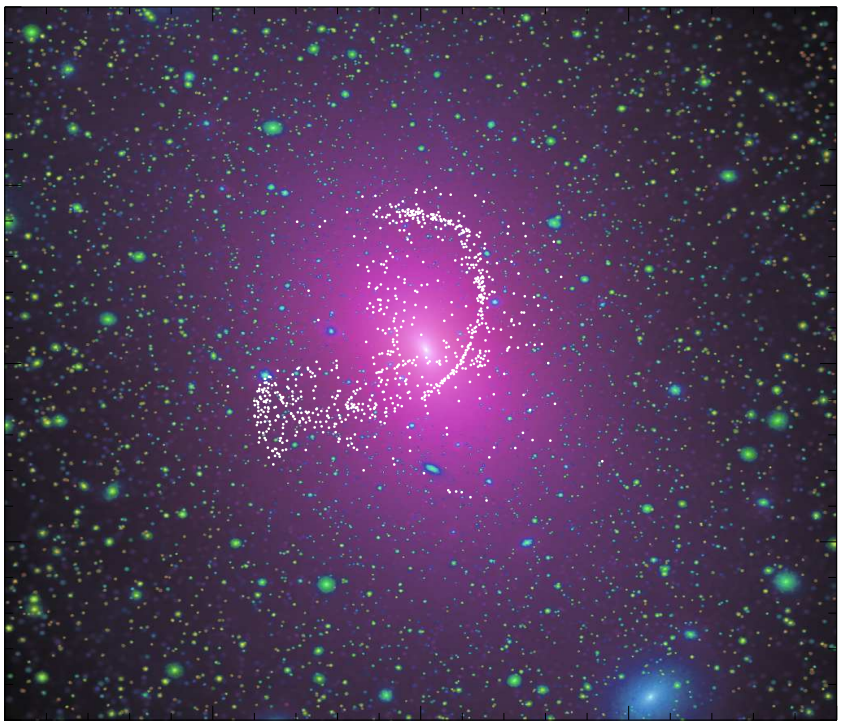

Figure 1: Present day snapshot view of a numerical simulation producing a system like the dark matter component of the Milky Way. The white dots represent a stellar stream, remnant of a merger event (Springel et al., 2008).

that subhalos are also elongated in nature, but with overall shapes that are rounder than their higher mass counterparts. The quest for understanding the properties of subhalos is highly motivated by the fact that they are predicted to host the satellite galaxies of the Milky Way, which are in turn, close enough to directly test the models of galaxy formation and evolution, as well as theories of gravity.

One of the first tests of this kind concerns the number of subhalos seen in simulations. Although the Milky Way itself is surrounded by a system of satellites, there are only a dozen of these known to-date. There is thus a flagrant discrepancy with the hundreds of thousands of small subhalos (which are satellites themselves) present in numerical experiments such as the one shown in Fig. 1. Although initially considered a problem, this fact has been used to complete our understanding of the way in which small galaxies form, providing insights into the role of different physical processes affecting the gas from which stars form. The number of big subhalos is also a tool used in Chapter 4 to refine our estimate of the total mass of the Milky Way, a number that, even today, is not known to better than a factor three, as different methods have yielded a variety of, sometimes, discrepant results.

Another tool highly used to measure the mass distribution of the Milky

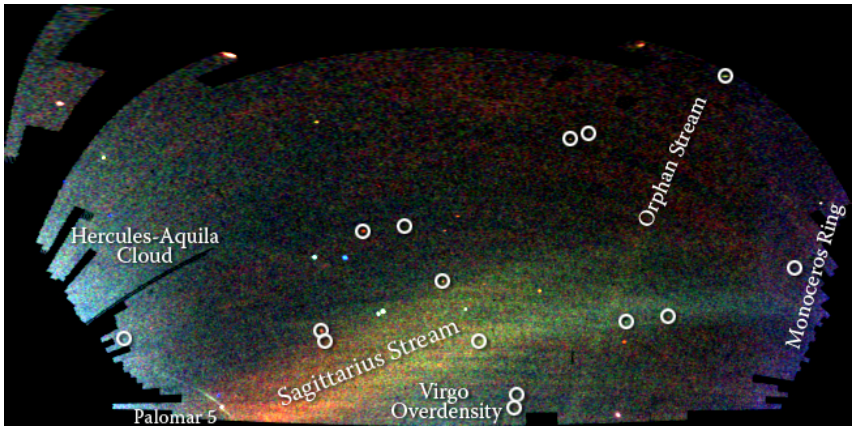

Figure 2: Observations of the Galactic halo, showing several stellar streams, such as the ones predicted from the numerical simulation shown in Fig. 1. The properties of the stars in the stream can be used to understand the mass distribution of the Mily Way (Belokurov et al., 2006).

Way is the dynamics of stellar streams. The white dots in Fig 1 represent a stellar tidal stream, remnant of a merger event. Since galaxy formation is a hierarchical phenomenon in the ΛCDM, these remnants are expected to be ubiquitous and also to be apparent in large numbers observations of our Galaxy. Such is indeed the case, as can be seen in Fig. 2. These stellar streams are coherent structures left-overs from accretion events and evolving under the influence of the gravitational pull generated by the Milky Way. Consequently, the dynamics of the individual stars can be used to constrain the mass distribution in the Galaxy.

Of particular interest is the stellar stream associated with the Sagittarius dwarf galaxy. Up to now, several models of the halo of the Milky Way have been used to explain the complex dynamics of this stream. However, the particular details of the most successful model are difficult to understand in the context of galaxy formation. In Chapter 5 of this Thesis we put forward a new model that successfully describes the stream, and that agrees with predictions of ΛCDM. For instance it includes the expected shape of the dark matter halo in the solar neighborhood keeping in mind the effects of a Galactic disk. Our model for the dynamics of the stream also incorporates the effect of the Large Magellanic Cloud (LMC), the most massive satellite of our Galaxy. We have found that the LMC affects the dynamics of the stream and has an impact on previous conclusions about the mass distribution inside the Milky Way.

There are many aspects of the ΛCDM model that have been only tangentially discussed, and that are by themselves interesting issues to address in the near future. Despite being limited in scope, it is my hope that the humble contribution shown in this Thesis has helped pave the road towards a better understanding of the formation and evolution of galaxies.

Samenvatting

De reis die begon door het simpelweg tellen van de sterren aan de hemel millennia geleden, heeft geleid tot een van de meest controversiële open vragen van de hedendaagse wetenschap: "Waar is het universum van gemaakt?". Het vinden van een bevredigend antwoord bleek bijzonder moeilijk, ondanks vele en uiteenlopende pogingen. De astrofysica heeft niet stilgestaan in deze onderneming, aangezien de laatste eeuw bijzonder vruchtbaar was in het ontwikkelen van een fysische omschrijving van de formatie en evolutie van het universum als geheel en alsmede de individuele componenten, zoals planeten, sterren en sterrenstelsels.

Het meten van snelheden van sterren in verre sterrenstelsels heeft bijvoorbeeld tot de conclusie geleid dat er aanzienlijk meer materie aanwezig is dan op het eerst gezicht te zien valt. Sterren bewegen door de totale gravitationele aantrekkingskracht van het sterrenstelsel waarin ze zich bevinden. Deze aantrekkingskracht hangt af van de massa, en als de massa van de sterren tot op zekere hoogte bekend is (bijvoorbeeld van hun helderheid), dan kunnen de snelheden ons vertellen of ons begrip van de wetten van Newton correct zijn, een natuurkundige theorie bekend sinds de XVII eeuw. Er werden grote verschillen waargenomen wanneer deze meting verricht werden, wat tot de conclusie leidde dat ofwel deze wetten fundamenteel fout waren, of dat sterrenstelsels verborgen massa bevatten. In dit proefschrift hebben we gewerkt onder de tweede hypothese, en duiden de missende massa aan met *donkere materie*, wat de nadruk legt op het niet zichtbaar zijn van deze vorm van materie. De discrepantie in the dynamica van sterren in sterrenstelsels suggereert dat donkere materie het dominante component is in deze systemen en dat de sterren een verwaarloosbare bijdrage hebben aan de totale massa van het systeem. Modellen en observaties suggereren dat donkere materie verdeeld is in een sferoïde die het zichtbare sterrenstelsel omringt.

Spectaculaire explosies van sterren aan het einde van hun leven in verre sterrenstelsels heeft ons ook toegestaan een belangrijke conclusie te trekken over de samenstelling van het universum. Naast donkere materie is er een kracht die sterrenstelsels in een versnelde manier van elkaar af doet bewegen. Omdat de aard van deze kracht onbekend is, met uitzondering misschien van het vacuüm zelf, moest er een nieuw onderdeel worden toegevoegd aan het

geheel. Dit onderdeel wordt aangeduid als *donkere energie* en verklaart naar schatting 3/4e van de materie/energie-inhoud van het heelal vandaag de dag, het overige 1/4e deel bestaat grotendeels uit donkere materie.

Helaas kunnen we alleen weloverwogen gissen naar de aard van donkere materie of donkere energie. Verschillende experimenten worden uitgevoerd om deze beter te begrijpen en te plaatsen in een samenhangend fysisch model voor het universum. Deze taak blijkt helaas erg lastig, en de resultaten tot nu toe zijn teleurstellend onbeslist.

Het ΛCDM model is een bepaald model, ondersteund door observaties, voor het universum, welke beide donkere componenten beschrijft. In dit model vormen en evolueren sterrenstelsels door de tijd middels het samensmelten van kleinere systemen. De aantrekkingskracht die door de donkere materie halo wordt opgewekt trekt nabije objecten aan, laat ze botsen en later volledig samensmelten om een nieuw massiever sterrenstelsel te vormen. Hoewel dit proces intuïtief goed is begrepen, worden we wiskundige vergelijkingen om dit te modelleren praktisch onoplosbaar zodra het aantal betrokken objecten stijgt. Zodoende is het gebruik van rekenmodellen niet alleen nodig, maar soms de enige manier om de formatie en evolutie van sterrenstelsels te bestuderen.

In dit proefschrift hebben we uitgebreid gebruik gemaakt van numerieke experimenten gebaseerd op N lichamen, waarbij het donkere materie component van sterrenstelsels wordt gerepresenteerd door puntmassa's, en de vergelijkingen welke de posities en snelheden voorspellen worden opgelost met krachtige computers. Het neusje van de zalm van dit soort simulaties bestaan uit miljarden van deze lichamen en zijn in staat, met ongekende details, de formatie en evolutie van donkere materie halos, zoals die van de Melkweg, te modelleren, hierbij worden de processen die leidde tot de huidige configuratie bijgehouden.

Figuur 1 is een momentopname van de huidige verdeling van donkere materie rondom een gesimuleerd systeem waarvan verwacht wordt dat het een massa heeft gelijk aan die van de Melkweg. Het diffuse component, waarvan het centrum het midden van het figuur definieert, laat zien dat de vorm van de donkere materie halo rondom de Melkweg verwacht wordt niet sferisch te zijn binnen het ΛCDM model. In feite, in hoofdstuk 2 van dit proefschrift wordt aangetoond dat het beter beschreven wordt door een ellipsoïde waarbij de asverhouding veranderd als functie van de afstand tot het centrum van de halo. In het algemeen wordt de vorm van de halo, op een afstand vergelijkbaar met de afstand van de zon tot het centrum van de Melkweg, beschreven door een verdeling die gedeeltelijk lijkt op een rugbybal, waarbij hij steeds minder assymmetrisch wordt bij grotere afstand tot het centrum. De vormen van donkere materie halos zijn het resultaat van een reactie op de configuratie van de dichtstbijzijnde delen van het universum en er is een direct verband met de manier waarop de samenstelling plaats vindt. Deze conclusies kunnen echter worden beinvloed wanneer andere fysische effecten in aanmerking worden genomen. Het samenspel tussen zichtbare en donkere materie bijvoorbeeld speelt

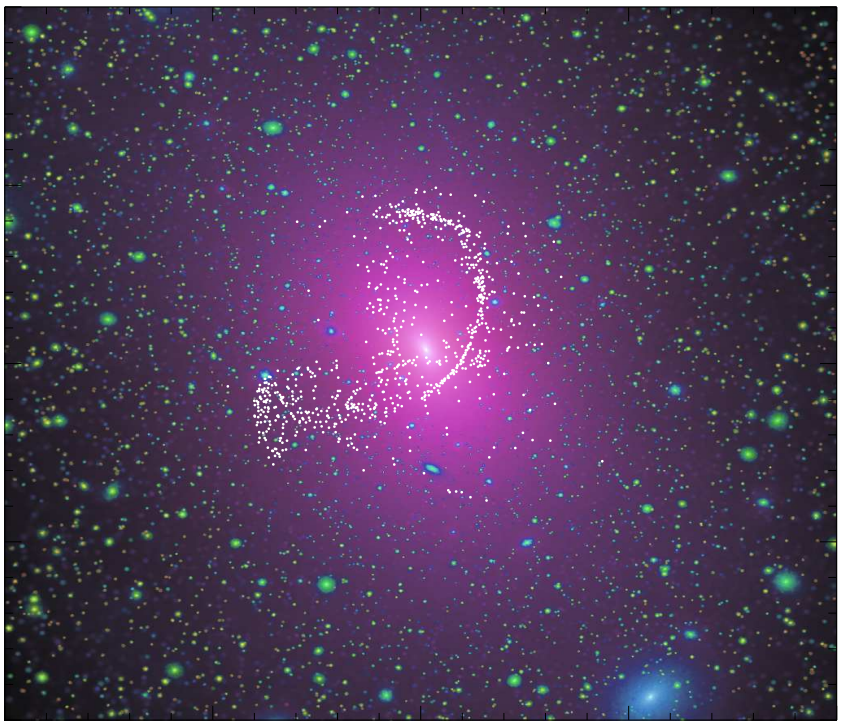

Figuur 1: Huidige momentopname van een numerieke simulatie welke een donkere materie component zoals de Melkweg produceert. De witte stippen zijn een stellaire stroom, een overblijfsel van een samensmelting (Springel et al., 2008).

een belangrijke rol in het vormen van de halo dichtbij zijn centrum, waarbij dit resulteert in een vorm die lijkt op een pindaloze M&M$^{\text{TM}}$.

Misschien wel de meest opvallende indruk na het zien van Figuur 1 is de grote hoeveelheid kleine structuren ingesloten in de halo. Dit zijn op zichzelf staande donkere objecten, bezig met het samensmelten met de hoofdhalo. In hoofdstuk 3 laten we zien dat subhalos ook langwerpig zijn, maar ronder dan hun zwaardere tegenhangers. De zoektocht naar het begrijpen van de eigenschappen van subhalos is gemotiveerd door het feit dat voorspeld wordt dat ze de gastheer zijn van satelliet sterrenstelsels van de Melkweg, die op hun beurt dichtbij genoeg zijn om direct modellen van formatie en evolutie van sterrenstelsels en theorieën van zwaartekracht te testen.

Een van de eerste proeven van dit soort betreft het aantal subhalos in simulaties. Hoewel de Melkweg zelf omringd is door satellieten, zijn er slechts een dozijn van bekend heden ten dage. Er is dus een tegenstrijdigheid met de honderd duizenden kleine subhalos aanwezig in numerieke experimenten zoals die getoond in Figuur 1. Hoewel in eerste instantie beschouwd als een probleem, is dit feit gebruikt om beter te begrijpen hoe kleine sterrenstelsels vormen en ons inzicht te geven in de rol van verschillende fysische processen

en hoe die het gas beïnvloeden waaruit de sterren ontstaan. Het aantal grote subhalos is ook een instrument dat wordt gebruikt in hoofdstuk 4 om onze schatting van de totale massa van de Melkweg te verfijnen, een getal dat, zelfs vandaag, niet beter bekend is dan binnen een factor van 3, aangezien verschillende methodes andere, soms afwijkende resultaten geven.

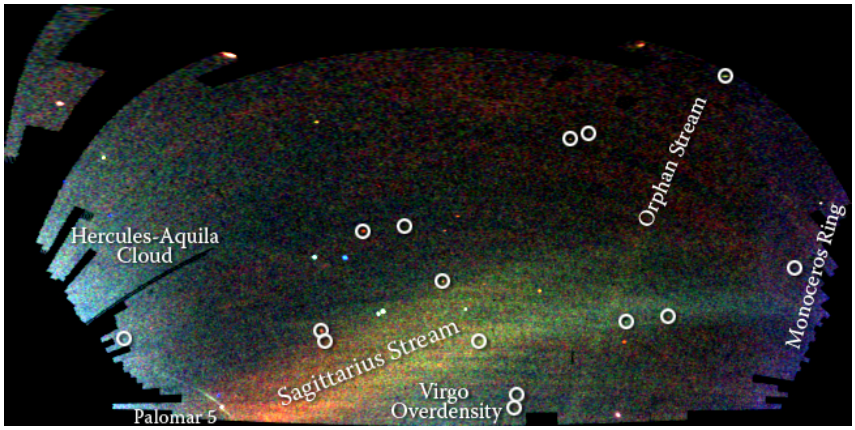

Figuur 2: Waarnemingen van de Galactische halo, met een aantal sterstromen zoals voorspeld uit de numerieke simulaties getoond in 1. De eigenschappen van de sterren in de stroom kunnen worden gebruikt om de massaverdeling van de Melkweg te begrijpen (Belokurov et al., 2006).

Een andere manier om de massadistributie in de Melkweg te bekijken is via sterrenstromen. De witte stipjes in Fig 1 stellen een dergelijke sterstroom voor, feitelijk gaat het om een restant van een dwergstelsel dat door de Melkweg is opgeslokt. Aangezien de vorming van sterrenstelsels een hiërarchisch proces is, verwachten we heel veel van zulke restanten, en dus ook in de waarnemingen van onze Melkweg. Dat blijkt inderdaad het geval te zijn, zoals te zien is in Fig. 2. Dergelijke sterstromen zijn coherente restanten van een botsing door een kleiner stelsel met de Melkweg en evolueren door diens zwaartekracht. Daardoor kan de dynamica van de individuele sterren in de stroom gebruikt worden om de massadistributie beter te meten in onze Melkweg.

De Sagittarius sterstroom trekt hierbij bijzonder de aandacht. Om de ingewikkelde dynamica te begrijpen zijn er diverse modellen gemaakt van de halo van onze Melkweg. Echter, de resultaten van het meest succesvolle model zijn lastig te begrijpen vanuit de context van de evolutie van sterrenstelsels. In hoofdstuk 5 van dit proefschrift stellen we een nieuw model voor dat de sterstroom met succes beschrijft en ook overeenstemt met voorspellingen van het ΛCDM-model. Zo houdt het bijvoorbeeld rekening met de verwachte vorm van de donkere materie halo in de buurt van onze zon, terwijl daarbij ook het effect van de schijf van de Melkweg niet wordt vergeten. Tevens neemt het model ook het effect mee van de Grote Magelhaense wolk (het grootste satellietstelsel van onze Melkweg). We hebben daarbij gevonden dat de Grote Magelhaense

wolk wel degelijk effect heeft op de dynamica van deze sterstroom. Daarbij moeten eerdere conclusies over de massadistributie in de Melkweg ook worden aangepast.

Er zijn veel aspecten van het ΛCDM-model die nu slechts zijdelings zijn besproken. Daarbij zijn ook veel interessante onderwerpen om in de toekomst nader te onderzoeken. Hoewel de reikwijdte van dit onderzoek beperkt is, hoop ik toch dat mijn bijdrage in dit proefschrift een steentje kan bijdragen aan het begrip van het ontstaan en de ontwikkeling van sterrenstelsels.

Resumen

La travesía que empezó miles de años atrás simplemente contando estrellas ha llevado a una de las preguntas más controversiales de la ciencia contemporánea: "¿De qué está hecho el Universo?". Encontrar una respuesta satisfactoria a esta pregunta ha sido particularmente difícil, a pesar de los muchos y diversos intentos hechos hasta el momento. En esta empresa la Astrofísica ha sido bastante fructífera, desarrollando un marco físico para la formación y evolución del universo como un todo, y de igual manera para sus componentes individuales, tales como planetas, estrellas y galaxias.

Midiendo las velocidades de estrellas en galaxias distantes, por ejemplo, hemos concluido satisfactoriamente que hay significativamente mucha más masa de la que se puede ver. Las estrellas se mueven como consecuencia de la atracción gravitacional generada por la galaxia en la que ellas viven. Esta atracción depende de la masa y, por lo tanto, si las masas de todas las estrellas se pueden estimar de alguna manera (por ejemplo a través de su brillo), sus velocidades pueden decirnos si nuestra interpretación de las Leyes de Newton es correcta, la cual es una teoría conocida desde el siglo XVII. Grandes discrepancias fueron encontradas cuando estas medidas se hicieron, lo que llevó a concluir que las leyes estan fundalmente equivocadas, ó que las galaxias tienen algín tipo de masa posiblemente escondida. En esta Tesis trabajamos bajo la segunda hipótesis y llamamos a la componente faltante *materia oscura*, enfatizando el hecho de que es materia que no es directamente detectable. El desacuerdo en la dinámica de las estrellas en galaxias sugiere que la materia oscura es la componente de masa más dominante en estos sistemas, y que las estrellas sólo hacen un contribución prácticamente despreciable a la cuenta total de la masa. Modelos y observaciones sugieren también que la materia oscura esté distribuida en forma casi esférica alrededor de la parte de la galaxia que es visible, en lo que llamaremos un *halo*.

Explosiones espectaculares de estrelllas al final de sus vidas en galaxias distantes también nos ha permitido llegar a otra importante conclusíon acerca de la composición del universo. Ademas de materia oscura, hay una fuerza que hace que las galaxias de alejen entre ellas en forma acelerada. Dado que la naturaleza de esta fuerza es desconocida para la humanidad, con la posible excepción del vacío en sí mismo, una nueva componente tuvo que ser agregada

al panorama. Esta nueva componente es llamada *energía oscura* y se estima que hoy forma 3/4 del contenido de materia/energía del Universo, mientras que el restante 1/4 es materia oscura.

Desafortunadamente, sólo hay disponibles estimaciones educadas de la naturaleza de la materia oscura o de la energía oscura. Muchos experimentos están siendo llevados a cabo actualmente tratando de entender estas componentes y ubicarlas dentro de un modelo fisico consistente para el Universo. Sin embargo esta parece ser una tarea insuperable y los resultados hasta ahora son decepcionantemente no concluyentes.

El modelo ΛCDM (por sus siglas en inglés) constituye una descripción particular del Universo, que es actualmente avalada por las observaciones. En este modelo las galaxias se forman y evolucionan gracias a la atracción gravitacional generada por una galaxia masiva sobre objetos cercanos haciéndolos colisionar y, con el tiempo, fusionar completamente para producir una nueva galaxia más pesada. A pesar de que este proceso es intuitivamente bien entendido, las ecuaciones que lo modelan se vuelven prácticamente intratables cuando el número de objetos involucrados empieza a crecer. Por lo tanto, el uso de herramientas computacionales no solamente es requerido, sino que es algunas veces la única forma de estudiar la formación y evolución de galaxias.

En esta Tesis usamos predominantemente experimentos numéricos basados en N cuerpos, donde la componente de materia oscura de las galaxias es representada por masas puntuales, y las ecuaciones que predicen las posiciones y velocidades son solucionadas numéricamente por computadores. Últimos avances en simulaciones de este tipo permiten incluir miles de millones de tales cuerpos y son capaces de modelar, con inaudito detalle, la formación y evolución de halos de materia oscura como los que rodean a la Vía Láctea, siguiendo todos los procesos que llevan a su configuración actual.

La Figura 1 es una muestra de la configuración actual de materia oscura alrededor de una sistema simulado del cual se espera que tenga la masa de la Via Láctea. La componente suave, cuyo centro define el centro de esta figura, muestra que la forma esperada según el modelo ΛCDM para el halo de materia oscura que envuelve la Vía Láctea no es esférico. De hecho, en el Capítulo 2 de esta Tesis es demostrado que un elipsoide cuyas razones de los ejes principales cambia como función de la distancia al centro del halo se aproxima mejor a esta forma. A una distancia comparable a la del Sol respecto al Centro Galáctico, el halo es descrito por una distribución de masa que parcialmente se parece a un balón de fútbol americano, y se vuelve progresivamente menos simétrico a medida que uno se aleja del centro. Las formas de los halos de materia oscura es una respuesta a la configuración de las regiones cercanas del universo que lo rodean y se correlacionan directamente con la forma en la cual el proceso de ensamblaje del halo toma lugar. Sin embargo, estas conclusiones pueden cambiar si otros efectos físicos se tienen en cuenta. Por ejemplo, la interacción de la materia visible con la materia oscura juega un papel importante en la de-

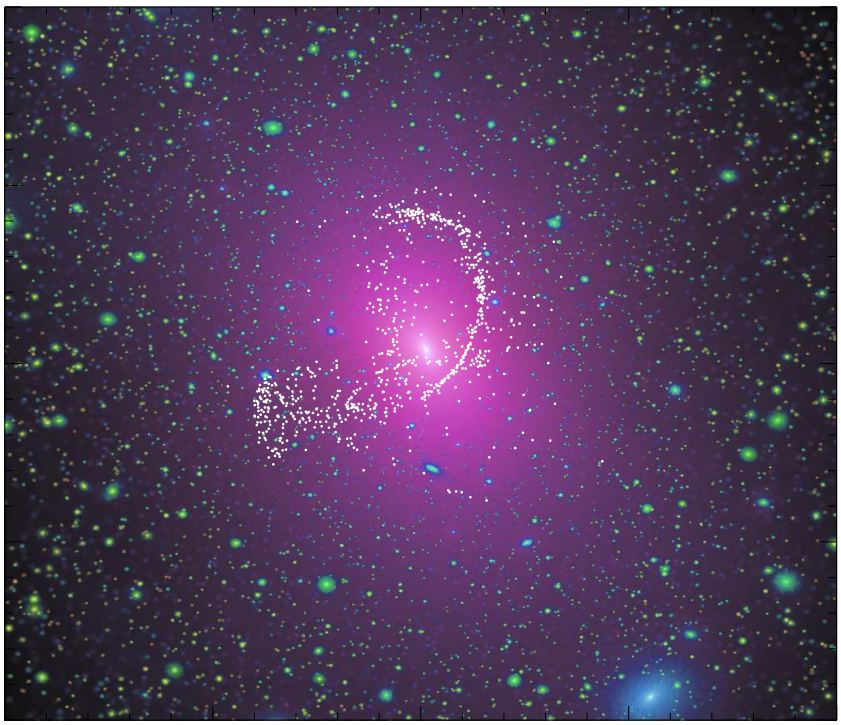

Figura 1: Configuración actual de una simulación que reproduce un sistema como la componente de materia oscura del Vía Láctea. Los puntos blancos representan una corriente estelar, la cual es el resultado de una fusión (Springel et al., 2008).

terminación de la forma del halo cerca de su centro, generando configuraciones que pueden ser descritas por la forma de un M&M$^{\text{TM}}$ sin maní.

Al mirar la Figura 1, la impresión mas fuerte es tal vez la enorme cantidad de pequeñas estructuras que habitan el halo. Éstos son también objetos compuestos de materia oscura (*subhalos*), que están actualmente fusionándose con el halo principal. En el Capítulo 3 mostramos que estos subhalos son también elongados, pero sus formas son en general más redondas que los halos más masivos. La misión de entender las propiedades de estos subhalos esta fundamentalmente motivada por el hecho de que estos alojan las galaxias satélites de la Vía Láctea, las cuales a su vez, están lo suficientemente cerca para evaluar directamente modelos de formación y evolución galáctica y teorías de gravitación.

Una de las primeras pruebas de este tipo se refiere al número de subhalos que se predicen en las simulaciones. A pesar de que la Vía Láctea está rodeada por un sistema de satélites, solo hay una docena de ellos conocidos actualmente. Hay entonces una evidente discrepancia con respecto a los cientos de miles de pequeños subhalos (que son también satélites) presentes en experimentos numéricos tales como el que se muestra en Figura 1. A pesar de que este

hecho fue inicialmente considerado un problema, más tarde fue usado para completar nuestro entendimiento de la forma en que las galaxias más pequeñas se forman, permitiendo comprender los efectos que algunos feńomenos físicos tienen sobre el gas del cual las estrellas se forman. El número de subhalos más grandes también fue usado como herramienta en el Capítulo 4 para refinar nuestro estimativo de la masa total de la Vía Láctea, el cual es un número que incluso hoy, no se conoce con exactitud dentro de un factor de tres, dado que los diferentes métodos usados para medirlo dan una variedad de resultados discrepantes.

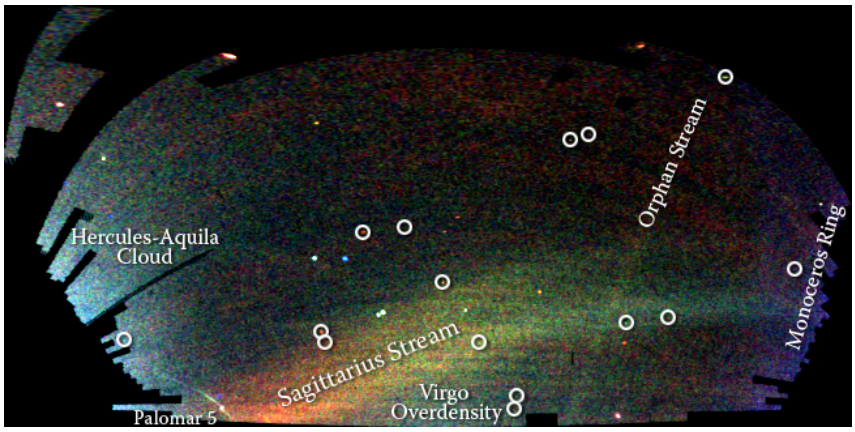

Figura 2: Observaciones del halo Galáctico, mostrando varias corrientes estelares, tales como las predichas por el experimento numérico mostrado en la Figura 1. Las propiedades de las estrellas en la corriente pueden ser usadas para entender la distribución de masa de la Vía Láctea (Belokurov et al., 2006).

Otra herramienta altamente utilizada para medir la distribución de masa es la Vía Láctea. Los puntos blancos en la Figura 1 representan una corriente estelar, la cual es el residuo de un evento de fusión. Dado que el proceso de formación galáctica es un fenómeno jerárquico en el modelo ΛCDM, se espera que estos residuos sean frecuentes y deban ser observados en grandes números en observaciones de nuestra Galaxia. Tal es el caso, como se puede ver en la Figura 2. Estas corrientes estelares son estructuras coherentes residuales de eventos de acreción y evolucionan bajo la influencia de la atracción gravitacional generada por la Vía Láctea. Consecuentemente, la dinámica de las estrellas individuales puede ser usada para restringir las posibles configuraciones de la distribución de masa en la Vía Láctea.

Particularmente interesante es la corriente estelar asociada a la galaxia enana de Sagitario. Hasta ahora, varios modelos para el halo de la Vía Láctea han sido utilizados para explicar la compleja dinámica de esta corriente. Sin embargo, los detalles de los modelos más exitosos son difíciles de explicar en el contexto de formación galáctica. En el Capítulo 5 de esta Tesis hemos propuesto un nuevo modelo que exitosamente describe la corriente y que concuerda

con las predicciones de ΛCDM. El modelo incluye, por ejemplo, la forma esperada del halo de materia oscura en la vecindad solar teniendo en cuenta los efectos del disco Galáctico. Nuestro modelo para la dinámica de la corriente estelar tambien incorpora el efecto de la Gran Nube Magallánica, la galaxia satélite mas masiva de nuestra Galaxia. Hemos encontrado que la Gran Nube Magallánica afecta la dinámica de la corriente estelar y tiene además un impacto apreciable sobre conclusiones previas acerca de la distribución de masa en la Vía Láctea.

Hay muchos aspectos del modelo ΛCDM que sólo han sido discutidos tangencialmente, y que son por sí mismos problemas interesantes para tratar en el futuro cercano. A pesar de ser limitada en su alcance, es mi esperanza que la humilde contribución mostrada en esta Tesis haya ayudado a pavimentar el camino hacia una mejor comprensión de los procesos de formación y evolución de galaxias.

Acknowledgements

This books embodies the most significant aspect of my life during the last four years. Looking at it, I cannot help but feel surprised by the many things that were accomplished in this period. It would indeed be untruthful to say that I did all of this by myself. The list of people that have helped me walk this road has been steadily increasing ever since I came here, almost four years ago. These concluding words are my humble attempt to express my heartfelt thanks to all of them.

None can be credited more for the culmination of this work than my promoter, Amina. Amina, it has been more than a privilege to work under your supervision. I will always feel indebted for your infinite patience and your enduring capacity to tolerate my innumerable mistakes! Among the many and invaluable things that you taught me, I will especially treasure your pragmatic counsel during the rough patches, more than one as they were.

I had the good fortune to work beside not just one boss, but two of them. Laura, in every aspect, I feel very fortunate for having shared this experience with you. Your constant guidance and unflappable character during these years have beyond doubt been instrumental in my thesis work. Our regular and long chats made the completion of all the projects we embarked on possible. And also provide irrefutable proof for that fact that depression can spread through Skype!

A significant part of the results shown in this book, and many others that I unfortunately could not finish on time, were completed with the priceless help of the members of the Virgo Consortium. I would like to express my gratitude to Volker, Carlos, Julio, and Simon for all the outstanding ideas and feedback.

Galactica is the group that I feel very lucky for being a part of. Yang-Shyang, Facundo, Laura, Else, Tjitske, Maarten, Hans, Teresa, Giacomo, Shoko, Hao, Pim, Kyle and Robyn, your input during our weekly meetings helped in shaping a great deal of my ideas. I would like to specially thank Maarten for all the interesting discussions we had. Besides being the other

member of the *Complainers Anonymous* (I guess it is not anonymous anymore) I had the privilege of sharing many enjoyable experiences with you during these four years. Thanks again to you, and to Hans, for helping me with the Dutch translation of my thesis summary despite the short notice.

To my office mates: Boris, Andre, Harish and Ajinkya, I should apologize for the many times I explicitly did not let you work when I was not in a productive mood, and could not bear to see you working! Thank you Harish for cheering me up during the "summer depression", also for your willingness to engage in the most pointless and vague conversations known to mankind. Thank you and Ivona for all the dinners at your place— being introduced to Bulgarian/Indian cuisine has been a most delightful experience.

I am divided between thanking and complaining about Koshy. On one hand you have been an immutable good friend, constantly cheering me up when bad moments kicked in. On the other hand, your unwelcome comments about the existence of dark matter kind of made me want to kick you out of my office! Andrea, thank you man for all the laughs. I truly enjoyed your visits to our office.

German, I will never find a way to repay you for all the things you have done for me in this time. You, Adriana, and Violeta have been the closest thing to a family that I had in Groningen. Thanks for everything!

To all the people in the Institute that unconditionally helped me, I would like to express my gratefulness. My special thanks to Jackie, Hennie, Christa, Lucia, Wim and Eite for all their support. My acknowledgment list is long and I probably will forget a few names, so instead I will extend my thanks to all of you. And if you just jumped to this last page in search of your name, please do not be disappointed!

I would also like to thank all my friends outside the institute for all the good moments. Isabel and Dorian, thanks for taking care of me during countless weekends that I spent at your home. To the members of the Walvisch, thanks for all the beers and jovial company. And to my friends back home, Luisa and Mauricio, thanks for always being there despite the distance.

Finally I reserved this space to thank my family. Ha sido un largo camino y una vez más me tengo que disculpar por mi obligada ausencia en estos últimos años. Pero a pesar de la insuperable distancia, siempre he sentido su calida e inmutable presencia en los muchos días de desasosiego. Este aparente final solo marca un nuevo comienzo, nuevamente lejos de ustedes; lo cual me entristece mas allá de palabras. Añoro cada segundo los dias pasados, pero encuentro consuelo en saber que el día vendrá en que nos encontraremos de

nuevo. Noelia, Mario, Maricela, Juliana, Gladys y Javier, quisiera dedicar con todo mi afecto este trabajo a todos ustedes. Gracias.

Thank you!